Implementation of Visible Wavelength Adaptive Optics at the William Herschel Telescope

DANIEL ALEJANDRO HOLCK-SANTIBANEZ

Implementation of Visible Wavelength Adaptive Optics at the William Herschel Telescope

Daniel Hölck

A thesis presented for the degree of

Doctor of Philosophy

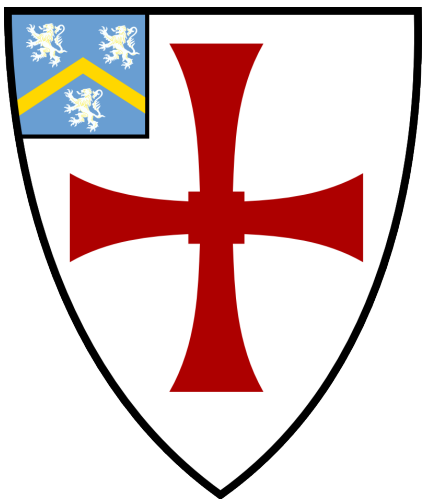

Centre for Advanced Instrumentation

The University of Durham

United Kingdom

August 2018

Implementation of Visible Wavelength Adaptive Optics at the William Herschel Telescope

Daniel Hölck

Abstract

This thesis investigates visible wavelength adaptive optics for astronomy. More specifically, it presents the development High Order Adaptive Optics (HOAO) system CANARY-HOsted UpGrade for HOAO (CHOUGH) for the William Herschel Telescope (WHT). The CHOUGH is a narrow field of view high-order single conjugate on-sky Adaptive optics (AO) demonstrator designed to be implemented at the WHT.

The main focus of this thesis is the development of a High-Order Wavefront Sensor (HOWFS) and an Atmospheric Dispersion Corrector (ADC). A HOWFS is a central piece of this experiment; it is a Shack-Hartmann with a sampling of 31×31 subapertures across the pupil. The detector is a Nüvü EMCCD camera, operating at > 500 Hz. The lenslet array, collimator and relay are commercial off-the-shelf.

When observing at a wide range of wavelengths the atmospheric chromatic dispersion can limit the spatial resolution (Wynne and Worswich, 1986), and this limit cannot be overcome by the AO system unless it is equipped with an ADC. Usually to avoid pupil actuator-lenslet array mismatch, the ADC is customarily placed very close to the pupil plane. This design aims to achieve a non-pupil conjugated ADC suitable to be located in any place inside the collimated beam path; this is due to the restrictions given by CHOUGH optical relay. The ADC also needs to satisfy the very small pupil shift requirement, for pupil stability.

As the results obtained in the laboratory confirmed, both of these subsystems have performed individually within their specifications which indicates that the proposed designs were successful.

Supervisors: Prof. Richard M. Myers and Dr. Nazim A. Bharmal

Acknowledgements

First and foremost, I would like to thank CONICYT (Comisión Nacional de Investigación Científica y Tecnológica/Chilean National Commission for Scientific and Technological Research) "Becas Chile" Doctoral Fellowship program for awarding me a research scholarship which made it possible for me to come to Durham. I am also very grateful to the Centre for Advanced Instrumentation (CfAI) that enabled me to travel to conferences and summer schools.

I offer my sincerest gratitude to my supervisors Richard Myers and Ali Bharmal for their support and guidance during my postgraduate studies at Durham University. Their continuous input and help has been fundamental for my thesis development and completion. I would also like to thank Tim Morris, James Osborn, Matt Townson, Ariadna Calcines, Tim Butterly, Alastair Basden, Marc Dubbeldam, Saavidra Perera and Amrit Lotay who have given me advice on numerous technical challenges that I faced in my PhD journey. Special thanks to Amrit and Saavi for being good friends as well.

I feel fortunate to have had an excellent university workspace and have shared it with valuable colleagues and friends. I am grateful to my officemates - Huizhe, David and Nico - for their help with Python and also for their friendship and daily support.

Above all I would like to thank my wife Hanna whose love and constant support was fundamental to get through this adventure. Thank you for being my proofreader and editor. But most of all, thank you for being my best friend and life companion.

Contents

Declaration

The work in this thesis is based on research carried out at the Centre for Advanced Instrumentation, Department of Physics, University of Durham, England. No part of this thesis has been submitted elsewhere for any other degree or qualification, and it is the sole work of the author unless referenced to the contrary in the text.

Some of the work presented in this thesis has been published in conference proceedings - the relevant publications are listed below.

Publications

- Hölck, D., Bharmal, N. A., Black, M., Henry, D. M., & Myers, R. M. CHOUGH: petite ADC for a high-order adaptive optics system. SPIE 9912, Advances in Optical and Mechanical Technologies for Telescopes and Instrumentation II, 99126Q, 2016.
- Hölck, D., Bharmal, N. A., Dubbeldam, C. M., & Myers, R. M. CHOUGH: spatially filtered Shack-Hartmann wave-front sensor for HOAO, Proceedings of the SPIE 9909, 990930, 2016.

List of Figures

List of Tables

Nomenclature

ADC Atmospheric Dispersion Corrector

AO Adaptive optics

CAWS Calibration and Alignment Wavefront Sensor

CCD Charge-Coupled Device

CfAI Centre for Advanced Instrumentation

CMD color magnitude diagram

CotS Commercial Off-The-Shelf

CHOUGH CANARY-HOsted UpGrade for HOAO

DARC Durham Adaptive Optics Real-time Controller

DASP Durham AO Simulation Platform

DM Deformable Mirror

E-ELT European Extremely Large Telescope

ELT Extremely large telescopes

EFL Effective Focal Length

EMCCD Electron-multiplying CCD

EO Edmund Optics

ESO European Southern Observatory

FWHM full width at half maximum

GHRIL Ground-based High Resolution Imaging Laboratory

GPI Gemini Planet Imager

GPIES Gemini Planet Imager Exoplanet Survey

GRACE GRound based Adaptive optics Controlled Environment

HOAO High Order Adaptive Optics

HODM High-Order Deformable Mirror

HOT High-order Test Bench

HOWFS High-Order Wavefront Sensor

ING Isaac Newton Group

IR Infrared

LODM Low-Order Deformable Mirror

LED light-emitting diode

LGS Laser Guide Star

LLA Lenslet Array

LTAO Laser Tomography Adaptive Optics

LUT Look-Up Table

MEMS-DM Micro Electro-Mechanical System Deformable Mirror

ML Microlens

MLA Microlens Array

MOAO Multiple-Object Adaptive Optics

NFSI Narrow-Field Science Imager

NGS Natural Guide Star

NIR Near-infrared

NCPA Non-common path aberrations

OAP Off-Axis Parabolic

ORM Observatorio Roque de los Muchachos

PALO Palomar Adaptive Optics

PSF Point Spread Function

PWM pulse-width modulation

QE Quantum Efficiency

RTC Real-time Control

RTCP Real-time control pipeline

SCAO Single Conjugated Adaptive Optics

SCExAO Subaru coronagraphic extreme AO

SCIDAR SCIntillation Detection And Ranging

SNR Signal-to-noise ratio

STYC Smart Tool in Yorick for CANARY

TCS Telescope Control System

TTM Tip-tilt Mirror

UKATC United Kingdom Astronomy Technology Centre

VLT Very Large Telescope

WDS Washington Double Star

WFS Wavefront Sensor

WHT William Herschel Telescope

Chapter 1

Introduction

Light coming from distant objects arrives as a flat wavefront at the Earth's atmosphere. When this wavefront travels through the different atmospheric layers it becomes distorted. As a consequence, instead of seeing a sharp round "Spot"(Airy disk) our detector sees a blurry image, thus restricting telescopes' capabilities to reach a diffraction limit Point Spread Function (PSF).

These aberrations in the wavefront are due to the variation in refractive index in the atmosphere. This variation is produced by small fluctuations in the air temperature as a result of changes in wind velocity, mixing atmospheric layers at different temperatures. These changes in the index of refraction vary in time and so do the aberrations in the wavefront.

Before the wavefront enters the atmosphere it is flat with the same phase along it. It forms a plane perpendicular to the propagation direction. After passing through the atmosphere the phase changes randomly for different points on the wavefront, distorting this plane. Figure 1.1 depicts the phase difference of two points on the wavefront after the effects of the atmosphere, where $l(\vec{r})$ is the optical path length and $\phi(\vec{r}) = \frac{2\pi}{\lambda} l(\vec{r})$ is the phase in the wavefront.

The strength of atmospheric turbulence that will affect the phase of the wavefront can be measured by using the *coherence length*, also known as *Fried parameter* or simply $r_\circ$. This parameter introduced by David Fried in the 1960's (Fried, 1966) is

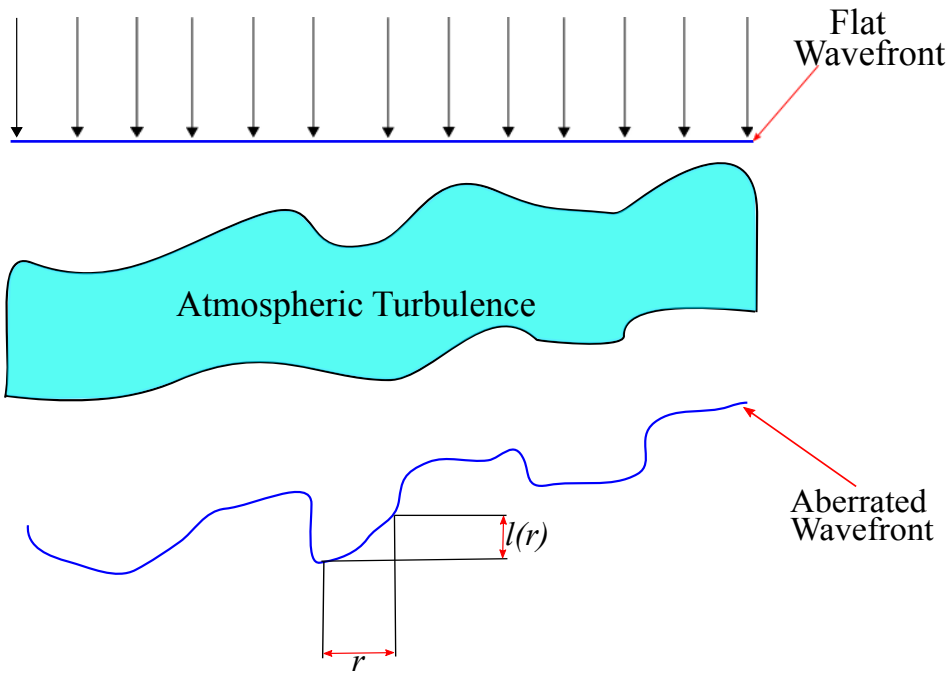

Figure 1.1: Phase difference of two points of an aberrated wavefront.

commonly used today to characterize seeing at a particular wavelength. The Fried parameter is usually expressed in centimetres. It defines a circular aperture size over which the mean-square wavefront error is $1\,\mathrm{rad}^2$. This can range from under 5 cm to over 20 cm. Average values are generally in the range of 7-12 cm (Hardy, 1998). Small values mean strong turbulence and bad seeing, whilst large values correspond to weak turbulence and good seeing.

In atmospheric science, turbulent random processes are described by the phase structure function. The Kolmogorov model of the turbulence distortions describes the specific form of the phase structure function, Equation 1.1. This is the average difference between two values of a random process. It is used to describe the spatial characteristics of the medium, in this case the atmosphere, and it is related to r_0

through Equation 1.2

$$D_\phi(\vec{r}) = \left\langle [\phi(\vec{x}+\vec{r}) - \phi(\vec{x})]^2 \right\rangle. \tag{1.1}$$

$$D_\phi(\vec{r}) = 6.88 \left(\frac{|\vec{r}|}{r_\circ}\right)^{5/3}. \tag{1.2}$$

Where

$$r_0 = \left[0.423k^2(\sec\theta_z)\int dh\ C_n(h)\right]^{-3/5}. \tag{1.3}$$

$C_n(h)$ is the refractive index structure parameter, it has altitude dependence, h, and represents the vertical distribution of the optical turbulence; θ_z is the zenith angle; and $\kappa = \frac{2\pi}{\lambda}$, the wavenumber. From equation 1.3 it can be inferred that r_0 is proportional to $\cos^{3/5}\theta_z$ as well as to $\lambda^{6/5}$.

In addition to the coherence length parameter, there is also a time parameter known as atmospheric coherence time, Greenwood or atmospheric time constant τ_0. It measures the time rate at which the wavefront phase structure changes which is defined in Equation 1.4.

$$\tau_0 = 0.314\frac{r_0}{V_0}. \tag{1.4}$$

where $\bar{V}$ is the wind velocity averaged over the altitude for each layer e defined by (Roddier et al., 1982).

$$\bar{V} = \left[\frac{\int_0^\infty C_n^2(h)V(h)^{\frac{5}{3}}dh}{\int_0^\infty C_n^2(h)dh}\right]^{\frac{3}{5}} \tag{1.5}$$

Another aspect to consider is the isoplanatic angle θ_0, which is the angle two stars can be separated, and still have their light pass through the same turbulent

region, defined as the angle at which the mean-square wavefront error, averaged over a large aperture, is $1\,rad^2$.

$$\theta_0 = 0.314\frac{r_0}{\bar{h}}. \tag{1.6}$$

where $\bar{h}$ is some characteristic average turbulence altitude. The averaging is done by weighting the $C_n^2(h)$ profile with $h^{5/3}$.

Astronomical AO is the technology used to correct in real time the aberrations caused by atmospheric turbulence, reducing in this way the wavefront distortions. The most conventional AO systems consist of three principle subsystems: a WFS, a DM, and a RTC system. Fig. 1.2 illustrates the concept.

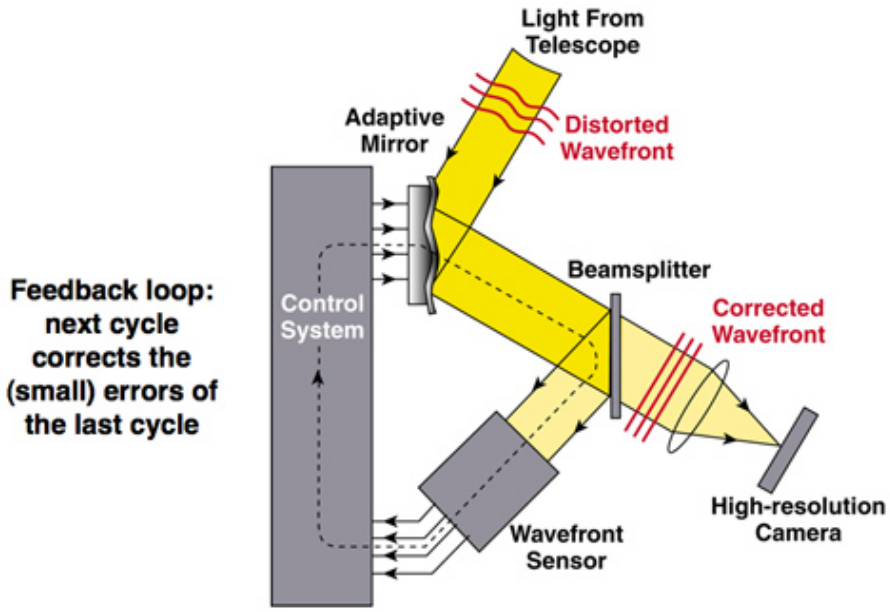

Figure 1.2: Illustration of the principles of AO technology.
(Image credits: Lawrence Livermore National Laboratory and NSF Center for Adaptive Optics).

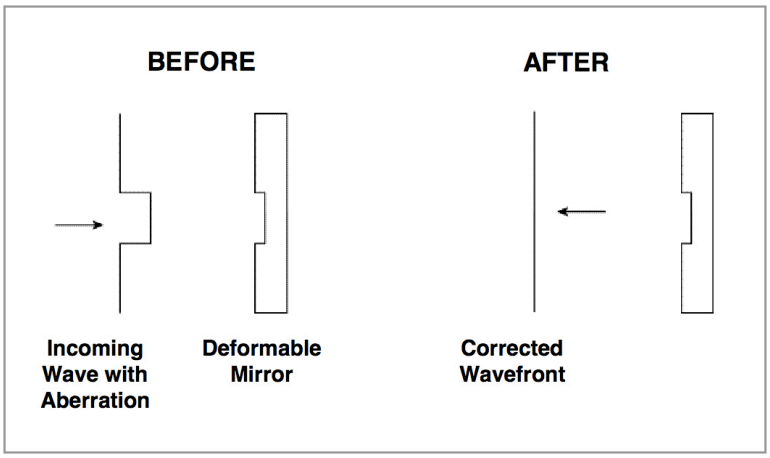

Figure 1.3: simplified form how a DM is able to correct a distorted wavefront. (Image credit: Lawrence Livermore National Laboratory and NSF Center for Adaptive Optics).

The main subsystems of an AO system are the following:

- The WFS is the instrument that measures the wavefront shape.
- The RTC reads the WFS measurements and gives the required commands to the DM to shape its surface into the needed form in order to compensate for the wavefront phase difference.
- The DM through a set of actuators shapes its surface in order to correct the wavefront distortion, as sketched in Figure 1.3

An AO system needs to convert the wavefront measurements into commands to the DM. An interaction matrix $\mathbf{P}$ is a matrix that measures the signal $\vec{s}$ of each actuator on the WFS,

$$\vec{s} = \mathbf{P}\vec{c}.$$

A control matrix is generated by creating a pseudo-inverse of a measured interaction matrix, this other matrix relates the measured wavefront to DM commands $\vec{c}$, that if applied to the DM will produce the shape necessary to correct the wavefront distortion.

$$\vec{c} = \mathbf{P}^{\dagger}\vec{s}.$$

Since AO for ground based telescopes started, at the end of the 1980's (Rousset, G. et al., 1990), night astronomical AO has been developed mostly for the near Infrared (IR) part of the electromagnetic spectrum, providing very good results in this range. Developing the technology for the near IR, and longer wavelengths was a natural path to follow, since r_0 varies proportionally to $\lambda^{6/5}$, thus the coherence length is longer, which makes correcting aberrated wavefronts more accessible given the available technology.

When r_0 is evaluated at a shorter wavelength, the wavefront needs to be finely sampled, so then subapertures become smaller. Consequently the resolution required to correct increases, and so does the actuator density required. Likewise τ_0 determines the correction speed, which increases when going to shorter wavelengths, the DM must respond faster with the decrease of the coherence time. Shorter wavelengths require wavefront correction on very short spatial and temporal scales. Smaller subapertures and quicker sampling mean less flux thus lower SNR. These are the challenges that emerge when developing AO for visible light. The technology used for AO has advanced: DMs have more actuators and finer strokes and can run faster as well. Similarly, the detectors technology is now equipped with higher resolution and speed.

HOAO corrections create a more compact and accurate PSF for high-angular resolution observations. With the capability to use fainter targets, HOAO allows high image resolution, so being able to reach high-order corrections in the visible gives access to new science targets on this side of the spectrum, or extremely high-order correction in the near-IR. For example, stellar population color magnitude diagram (CMD)s have better diagnostic power at optical wavelengths. This has led to the requirement of enhancing AO at shorter (0.7–0.8 μm) wavelengths as well as developing new techniques for estimating the ages of stellar populations. Direct imaging of exoplanets benefits from HOAO instrumentation, where contrast ratios of 10^5 within 0.1 arcsec are required. Exoplanets are a high priority science goal for the new Extremely large telescopes (ELT)s projects.

Currently there are a few projects working on higher order AO, these instruments have been designed with additional visible wavelength capabilities. The projects are reviewed below.

- **SAXO** (Petit et al., 2008) is a specific sub-system of SPHERE (Beuzit, 2008) at a 8.2 m telescope. SPHERE is a planet finder for the Very Large Telescope (VLT) dedicated to exoplanet imaging, detection, and characterization. It incorporates a very high-order AO System (SAXO) together with a coronographic device. SAXO is equipped with a CILAS DM with 41 x 41 actuators and a 40 x 40 subaperture visible spatially filtered Shack-Hartmann (VIS-WFS) based on a EMCCD camera. It is a 240 x 240 pixel (pixel size is 24 x 24 μm^2) Charge-Coupled Device (CCD) with a sampling frequency $\geqslant$ 1200 Hz. A SPHERE observation is the discovery of an edge-on disc reported in a paper entitled "A new disk discovered with VLT/SPHERE around the M star GSC 07396-00759" (Sissa et al., 2018).

- **GPIAO** (Poyneer et al., 2016) is an AO subsystem for Gemini Planet Imager (GPI) (Macintosh et al., 2007). Built for the Gemini South telescope in Chile, which has an 8-meter diameter primary mirror. The AO system utilizes a woofer/tweeter mirror pair, a 9 x 9 mirror from CILAS with a 5 mm actuator pitch and $\pm 3.4\,\mu$m stroke; and a 4096-actuator Boston Micromachines Micro Electro-Mechanical System Deformable Mirror (MEMS-DM), 5 nm actuator pitch and 1.07μm stroke. The WFS makes visible-light measurements, it is a Spatially-Filtered Shack-Hartmann WFS (Poyneer and Macintosh, 2004). The control loop can run at 1 kHz on bright stars and the 160 x 160 pixel CCD operates at 700-900 nm. The science instrument for GPI is a Near-infrared (NIR) integral field spectrograph (Larkin et al., 2014). GPI has been used for a variety of science missions, including the large scale Gemini Planet Imager Exoplanet Survey (GPIES) *.

*https://www.gemini.edu/sciops/instruments/gpi/gpies-campaign

- **Subaru coronagraphic extreme AO (SCExAO)** (Lozi et al., 2015) at 8.2 m Subaru telescope, is an AO instrument designed to be inserted between the Subaru curvature sensor adaptive optics system AO188 (Hayano et al., 2010) and the infrared HiCIAO (Hodapp et al., 2008) camera (Garrel et al., 2011). SCExAO was designed to operate between 0.6 to 2.4 μm. It has a 2000-actuator DM and a visible pyramid wavefront sensor operating at 3.5 kHz. The science instruments are two visible interferometric modules, VAMPIRES (Norris et al., 2015) and FIRST (Bordwell et al., 2015). Direct imaging Observation obtained from the Subaru SCExAO system with data recorded by the HiCIAO are reported in the paper "Subaru/SCExAO First-Light Direct Imaging of a Young Debris Disk around HD 36546" (Currie et al., 2017).

- **PALM-3000** (Burruss et al., 2014) is the second-generation astronomical adaptive optics facility for the 5.1 m Hale telescope at Palomar Observatory. It is an extension of the PALAO AO system (Dekany). It uses the 350-actuator DM of PALAO and adds a 3388-actuator DM alongside with a Shack-Hartmann wavefront sensor. The WFS has four modes of lenslet array with up to 64 x 64 sampling in the pupil plane. This system has been engineered specifically to optimize high-contrast study used in conjunction with specialized speckle-suppressing instrumentation (Dekany et al., 2013). Four back-end instruments are planned at first light: the PHARO near-infrared camera/spectrograph, the SWIFT visible light integral field spectrograph, Project 1640, a near-infrared coronagraphic integral field spectrograph, and 888Cam, a high-resolution visible light imager (Bouchez et al., 2008). The paper "First Exoplanet and Disk Results With the Palm-3000 Adaptive Optics System" (Burruss et al., 2013), presents initial high-contrast circumstellar disk results from the PHARO vector vortex coronagraph and exoplanet spectra from the P1640 integral field spectrograph.

- **MagAO** is the AO system for the 6.5 m Magellan Clay telescope located in Las Campanas Observatory in Chile. It has a 585-actuators adaptive secondary mirror and a 1000-Hz pyramid wavefront sensor. It was designed to work in the Mid-IR but also to work at visible wavelength using its VisAO camera to take advantage of intermittent periods of night when good-median seeing conditions are present (Kopon et al., 2009). Using MagAO's VisAO camera was detected the extrasolar giant planet (EGP) β Pic-toris b in Y -short (YS, 0.985 μm), at a separation of 0.470 $\pm$ 0.010" and a contrast of $(1.63\pm0.49)\times10^{-5}$ (Males et al., 2014).

This thesis aims to describe CHOUGH (Bharmal et al.), an instrument designed with the purpose to investigate AO in the visible region of the spectrum ($\geqslant$ 650 - 850 nm). It provides specific technologies for increasing the order of correction, enabling high Strehl ratio Natural Guide Star (NGS)-Single Conjugated Adaptive Optics (SCAO) using visible light. In order to investigate high-quality PSF correction, CHOUGH includes a MEMS-DM arranged with a Fried actuator mapping to a WFS, which is why CHOUGH incorporates a High-Order Shack-Hartmann WFS (Hölck et al., 2016) operating up to 1.2 kHz. CHOUGH intends to carry out visible HOAO experiments at the 4.2 m WHT, located in La Palma, Spain. Unlike the instruments mentioned above, CHOUGH was not designed for a specific sub-system, instead it is intended as a high-order AO technology & capabilities demonstrator, and then to deliver a flexible platform for on-sky AO research in the visible. Also CHOUGH has the potential to receive a visitor instrument.

CHOUGH was designed to have a "woofer-tweeter" configuration. A low-speed and high-stroke operation, and a high-resolution, high-speed and low-stroke operation, identified as “woofer” and “tweeter”, respectively.

CHOUGH operates using existing components and infrastructure of another AO project, CANARY (Myers et al., 2008). CANARY is an AO testbed located in one of the Nasmyth platforms of the WHT and provides CHOUGH with the optical

relay to bring the light collected by the telescope; it also contributes with its DM to work as a "woofer" mirror; supplies calibration sources; and a target acquisition system. The use of CANARY infrastructure permits adaptive optics at lower cost.

The thesis is structured as follows:

- **chapter 2** describes the concept of the design of CHOUGH, together with a brief description of its different subsystems such as the WFS, DMs, ADC, Optical Relay, RTC and NFSI, as well as the hosting facilities.

- **chapter 3** goes into detail of the HOWFS design, explains theoretical requirements, constraints, optical and mechanical design, laboratory experiments and results.

- **chapter 4** discusses the inconveniences induced by atmospheric dispersion, and the need to implement an ADC in the instrument. Theoretical requirements, simulations, as well as optical design of the CHOUGH ADC are explained in this chapter, as well as, laboratory testing and results. This chapter along with chapter 3 are central to this thesis as they present my main contribution to the CHOUGH project.

- **chapter 5** describes the possible engineering target selection proposed for the on-sky run during two nights on October 2016. In addition to the discussion of the number of photons required for the WFS.

- **chapter 6** presents a summary of this thesis, along with, conclusions and future plans for this project. It considers the results obtained in the laboratory.

Chapter 2

CHOUGH: CANARY-HOsted UpGrade for HOAO

CHOUGH (Bharmal et al., 2016) is an add-on instrument that works together with CANARY(Myers et al., 2008) assisting the WHT to achieve its diffraction limit at visible wavelengths. Specifically CHOUGH is a narrow-field of view High-Order SCAO instrument upgrade for the CANARY experiment. It aims to enable high-order AO capabilities on the 4 m telescope. Its principal purpose is to investigate AO in the visible region of the spectrum $\geqslant 600$ - 900 nm and study high-quality PSF correction which is why CHOUGH incorporates a High-Order Shack-Hartmann WFS operating at up to 1 kHz (see Chapter 3).

This chapter gives a description of CHOUGH as an understanding of its design is central to anticipate the requirements set for the subsystems described in chapters 3 and 4.

2.1 William Herschel Telescope

The CHOUGH AO experiment has been designed to run on the 4.2 m diameter WHT. The telescope, inaugurated in 1987, is located at the Observatorio del

Roque de los Muchachos on the island of La Palma in the Canary Islands, Spain. It was manufactured by Grubb Parsons Ltd. in Newcastle. It is a telescope with a paraboloidal primary mirror of diameter 4.2 m, made of Cervit, and a convex hyperboloidal secondary mirror, made of zerodur of 1.0 m diameter. The two mirrors of the WHT are aluminium coated, covering from the optical to the infrared range of the spectrum, Figure 2.1 shows a plot of Aluminium reflectance against wavelength compared to Silver and Gold.

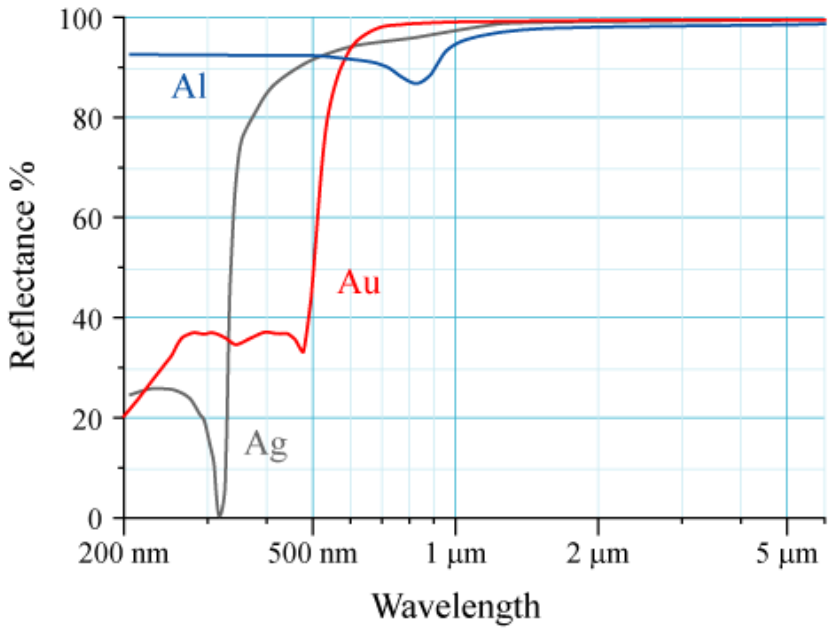

Figure 2.1: Aluminum, Silver, and Gold reflectance against wavelength. (Image credits: Bob Mellish).

The telescope has a Ritchey Chretien f/11 Cassegrain configuration. Additional to the primary and secondary mirrors, a flat fold mirror allows the use of two Nasmyth platforms, GRound based Adaptive optics Controlled Environment (GRACE) and Ground-based High Resolution Imaging Laboratory (GHRIL). The effective focal length of the telescope for the Cassegrain and Nasmyth foci is 46.2 m. The available unvignetted field diameter is 5 arcmin at the Nasmyth and folded Cassegrain foci.

Left hand side of Figure 2.2 shows a sketch of the WHT building. Right hand

side is the interior of the actual telescope building where the two Nasmyth platform can be seen at the sides of the primary mirror.

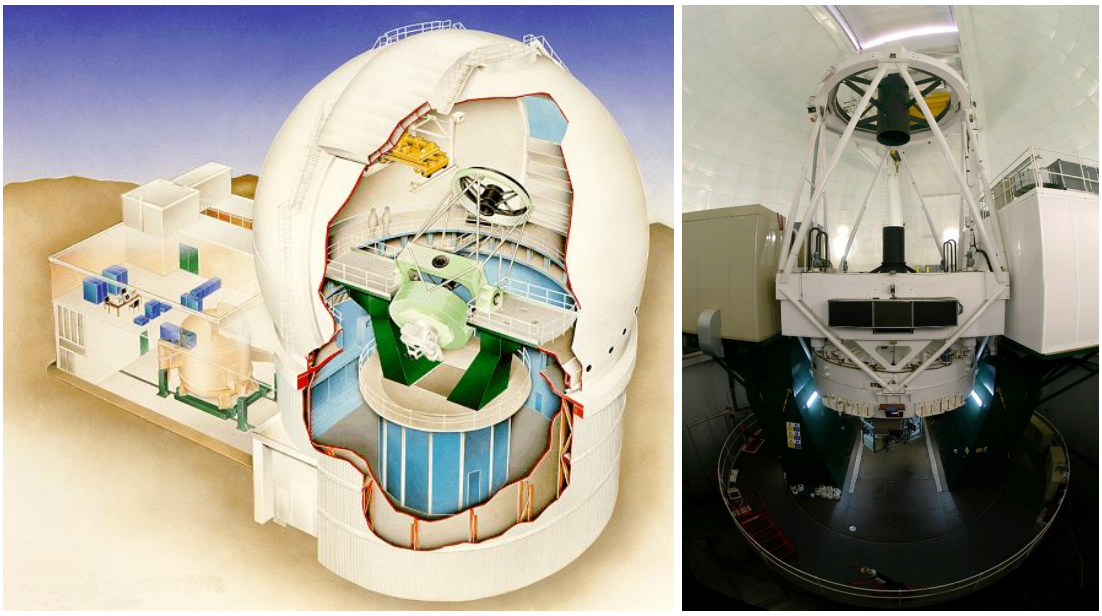

Figure 2.2: William HErschel TelescopeWHT. (Image credits: Isaac Newton GroupING).

2.2 La Palma Site Characteristics

The atmospheric optical turbulence at the astronomical site of Roque de los Muchachos Observatory at La Palma has a median seeing of 0.71" according to data obtained through SCIntillation Detection And Ranging (SCIDAR) observations from February 2004 to August 2009 (Garcia-Lorenzo and Fuensalida, 2011). A common description of the astronomical seeing conditions at an observatory is the full width at half maximum (FWHM) of the seeing disk. The FWHM of the long-exposure seeing-limited PSF in large telescopes is computed with the standard formula 2.1

$$\text{FWHM} = \frac{0.98\lambda}{r_0}. \tag{2.1}$$

Since the seeing is known, r_0 can be derived from the above equation. Bearing in mind that the standard wavelength λ for seeing measurements is 500 nm, and FWHM is used radians, the value of r_0 is 0.14 m.

The coherence length $r_\circ$ sets the number of degrees of freedom of an AO system, see Figure 2.3. The primary mirror is divided into subapertures of size r_0, where the number of subapertures will be approximately $\sim D/r_0$, where D is the telescope diameter. For a 4.2 m primary mirror and an r_0 of 0.14 m the number of subapertures is approximately $\sim$30.

The limited capability to fit a wave-front with a finite actuator spacing leads to the fitting error where the small details of wave-front remain uncompensated. For an inter-actuator spacing d_s, the fitting-error phase variance is

$$\sigma^2_{fit} = k_f(d_s/r_0)^{5/3}\text{rad}^2. \tag{2.2}$$

Equation 2.2 gives the fitting error, where k_f coefficient depends on the type of DM selected, d_s is the subaperutre on the DM, and r_0 is the scaled Fried parameter.

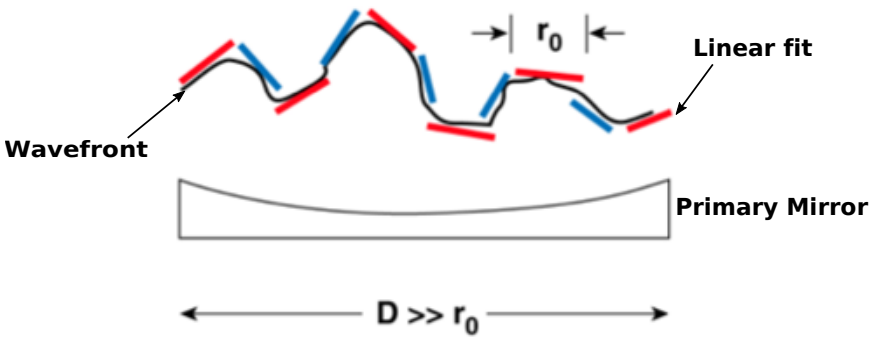

Figure 2.3: Wavefront linear fit. (Image Credits: Claire Max, Astro 289C, UCSC).

The k_f coefficient for CHOUGH's continuous face sheet DM is 0.28; and the (d_s/r_0) ratio for CHOUGH is 0.937. Inserted these numbers in Equation 2.2, the fitting σ^2_{fit} is $0.25\,\mathrm{rad}^2$.

The time delay between the measurement and correction of turbulence in AO system results in the temporal error. The mean coherence time τ_0 at the Observatorio Roque de los Muchachos (ORM) according to data acquired during the campaign site search of the E-ELT is 7.30 ms (Giordano et al., 2013). The temporal error is indicated by Equation 2.3

$$\sigma^2_{temp} = (\tau/\tau_0)^{5/3}\mathrm{rad}^2. \tag{2.3}$$

If the system is to run at 1 kHz, the temporal error σ^2_{temp} according to Equation 2.3 is $0.036\,\mathrm{rad}^2$.

Another source of error considered for AO systems, is the angular radius that characterizes the region of good correction, the isoplanatic angle θ_0, defined in Equation 1.6. Then the isoplanatic error is given by

$$\sigma^2_{iso} = (\theta/\theta_0)^{5/3}\mathrm{rad}^2. \tag{2.4}$$

Summing up the errors described previously, the total error budget for the system is

$$\sigma^2 = \sigma^2_{fit} + \sigma^2_{temp} + \sigma^2_{iso}. \tag{2.5}$$

A useful measure of the performance of an AO system is the Strehl ratio. This is defined to be the ratio of the central intensity of the image of a point source to that which would be produced by a perfect diffraction limited telescope having the same aperture and throughput. It follows that the maximum value that the Strehl ratio can take is 1.0.

The Strehl ratio is related to the wave-front errors via the Maréchal approximation

$$SR \sim e^{-\sigma^2}. \tag{2.6}$$

CHOUGH is primarily considered to be an on-axis experiment, therefore the isoplanatic angle error contribution can be 0. Then the Strehl ratio obtained with Equation 2.6 is approximately 0.73

CHOUGH simulations were done with Durham AO Simulation Platform (DASP) (Basden et al., 2010), to explore and justify the system's design specifications presented for the project's proposal. The Strehl ratio obtained with the simulations was 0.74. This agree with the theoretical error estimated in this section.

2.3 CANARY

CANARY (Myers et al., 2008), is a project led by the University of Durham and Paris Observatory. It is a wide-field of view open-loop AO demonstrator, located at one of the Nasmyths platforms in the 4.2 m WHT. CANARY emulates a single Multiple-Object Adaptive Optics (MOAO) channel of MOSAIC (Kelz et al., 2015), which is a proposed multi-object spectrograph instrument for the European Extremely Large Telescope (E-ELT). CANARY was developed in various phases (Gendron et al., 2016); starting with Phase-A, a NGS-only configuration with a single DM; and concluded with Phase-C2 which includes four Laser Guide Star (LGS) WFS tomography in a "woofer-tweeter" DM configuration. The latter phase is of interest for CHOUGH, since the instrument makes use of some these elements to operate on the telescope. Phase C2 (Figure 2.4) includes two DMs, an ADONIS 52-actuator DM and an ALPAO 241-actuator and a tip-tilt mirror; 4 LGS WFSs and 3 off-axis WFSs; as well as light sources for off-sky calibration.

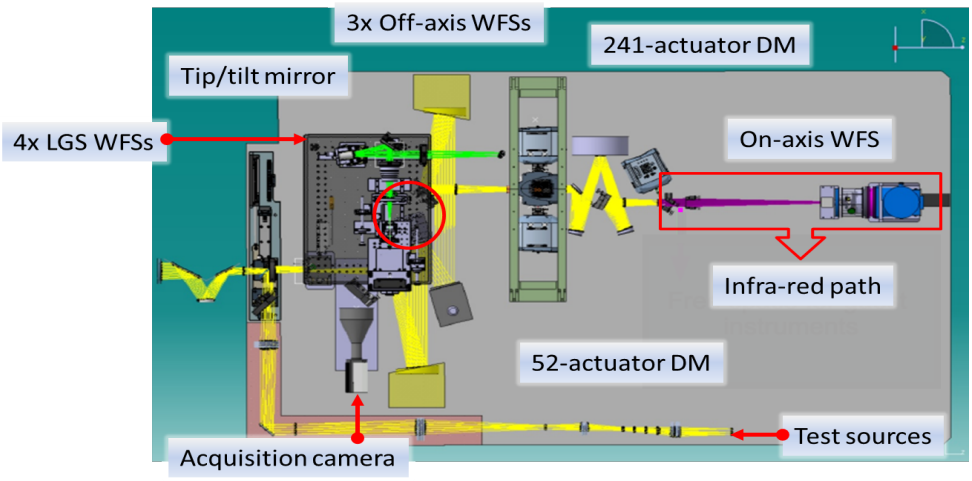

Figure 2.4: CANARY phase C2. (Image credits: Nazim Bharmal).

2.4 CHOUGH

CHOUGH was designed as an add-on instrument that goes on top of the CANARY experiment, this is the on-sky configuration, aside from this it also works as a standalone test bench to run experiments in the laboratory.

The combined CHOUGH–CANARY experiment can be described as a conventional SCAO system by design that uses a dual-DM, a "woofer–tweeter", together with a High-order Shack-Hartmann WFS operating at up to 1.2 kHz.

The flow chart in Figure 2.5 shows an overview of CHOUGH's subsystems. The thick-blue-arrows represent the light flow. Thin-black-arrows the flow of the control system.

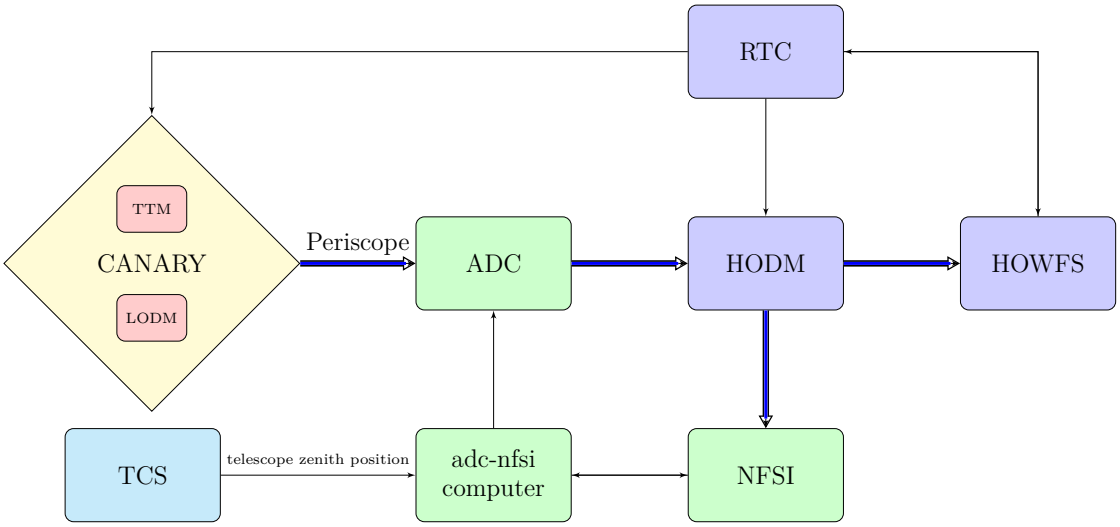

Figure 2.5: CHOUGH flow-chart. The thick-blue-arrows represent the light flow and the thin-black-arrows the flow of the control system.

From CANARY CHOUGH makes use of the 241-actuator DM, a tip-tilt mirror, alignment light sources and relay optics. Figure 2.6 shows a schematic of this configuration, where CHOUGH appears on the top right corner of CANARY. CHOUGH was built onto a breadboard placed 445 mm on top of the CANARY bench, and the light from CANARY is brought up to CHOUGH level through a periscope, as indicated on the diagram. Figure 2.7 shows a 3D-model of the two-level configuration, where the large bottom bench is CANARY and on top of it, at the front right is the CHOUGH bench. Figure 2.8 is picture of the actual CHOUGH-CANARY set up at the telescope. This was installed in GHRIL, one of the Nasmyth platform of the WHT.

CHOUGH also takes advantage of the CANARY RTC, DARC (Basden et al., 2010), reconfigured for CHOUGH's needs, likewise the RTC can be easily configured back for CANARY.

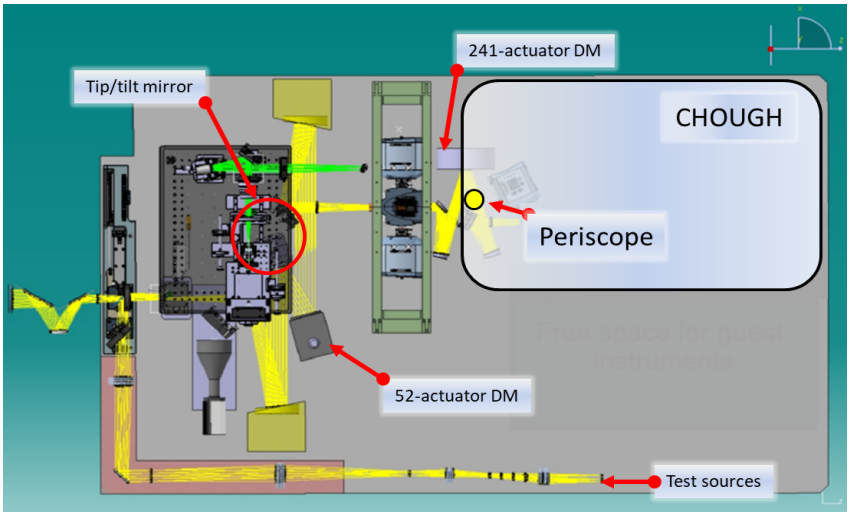

Figure 2.6: CANARY phase C2 CHOUGH configuration. (Image credits: Nazim Bharmal).

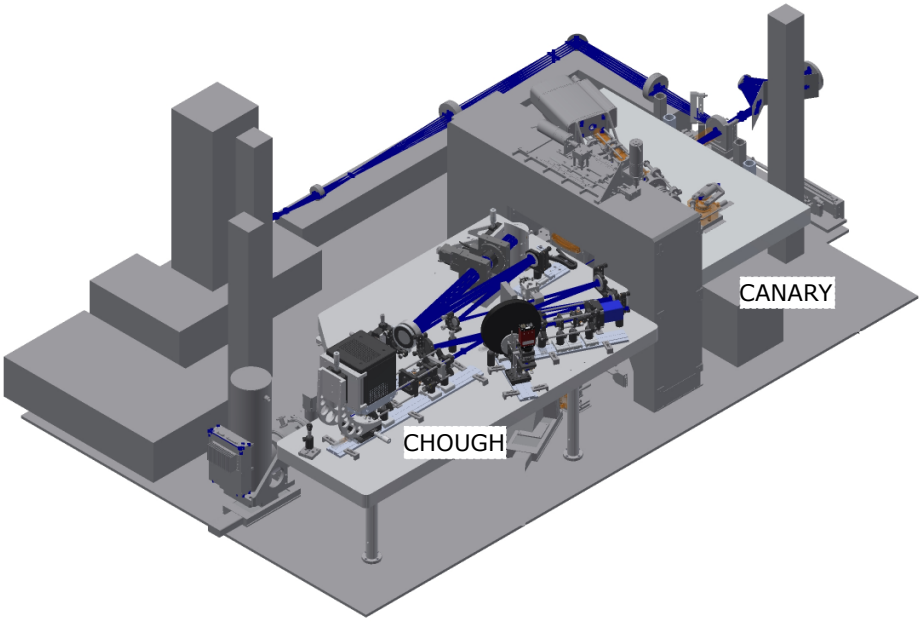

Figure 2.7: 3D mechanical model of the two-level CANARY-CHOUGH configuration.

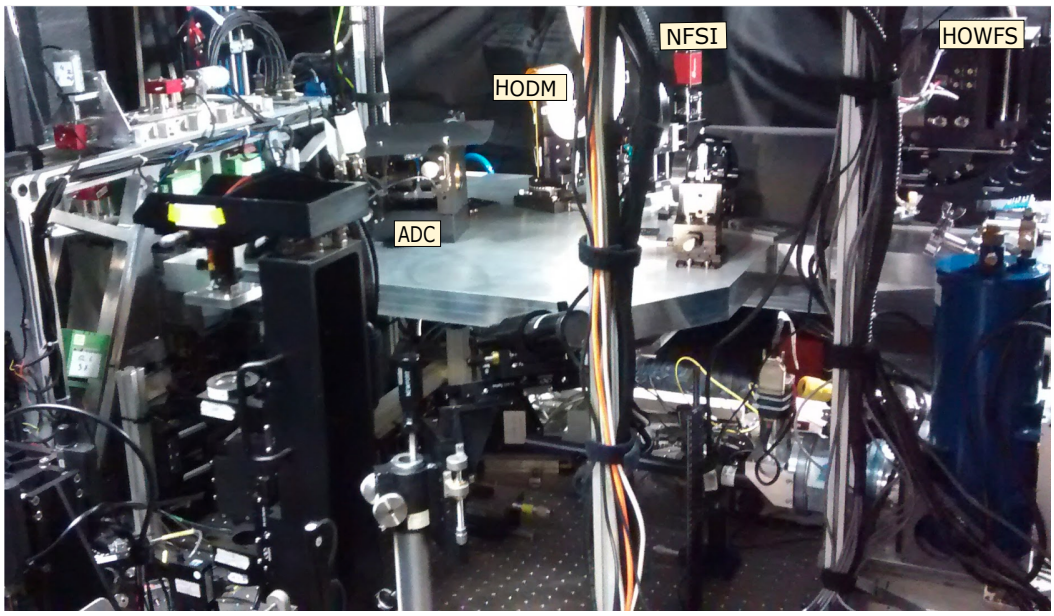

Figure 2.8: CHOUGH bench mounted on top of CANARY at the WHT. (Image credits: Nazim Bharmal).

Following the flow chart in Figure 2.5, the light collected by the telescope is redirected towards the Nasmyth platform into CANARY, where after reflecting onto the Tip-tilt Mirror (TTM) and LODM inside CANARY, the light is picked up by a periscope into CHOUGH. Figure 2.9 shows a 3D-model of the periscope. A collimated beam goes through the ADC and reflects onto various optics to then re-image the pupil onto the HODM and, finally, re-image the pupil at an output plane conjugated to the HOWFS and NFSI. The adc-nfsi computer retrieves the telescope positions from the Telescope Control System (TCS) and adjusts the ADC in order to compensate for the chromatic dispersion produced at the different zenith angles.

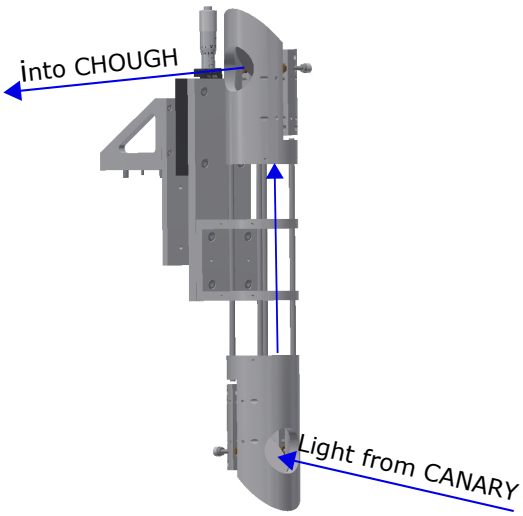

Figure 2.9: Periscope mechanical model.

Figure 2.10 shows a 3D-mechanical model of CHOUGH breadboard. The light track is represented in red lines starting at the periscope.

Figure 2.11 is a photograph of the CHOUGH breadboard in the laboratory. An Optical system, nicknamed "illuminator" was designed to emulate a narrow field image (<3" radius) from a 4 m telescope. This illumination system can connect to different diffraction-limited fibres, each one linked to a light sources. Currently only on-axis point sources are possible. In addition to the illumination system, a common-path interferometer to measure post-AO corrected light was implemented in the laboratory, it is named Calibration and Alignment Wavefront Sensor (CAWS)(Dubost et al., 2018) and it is not discussed in this thesis since its implementation did not form part of this thesis project.

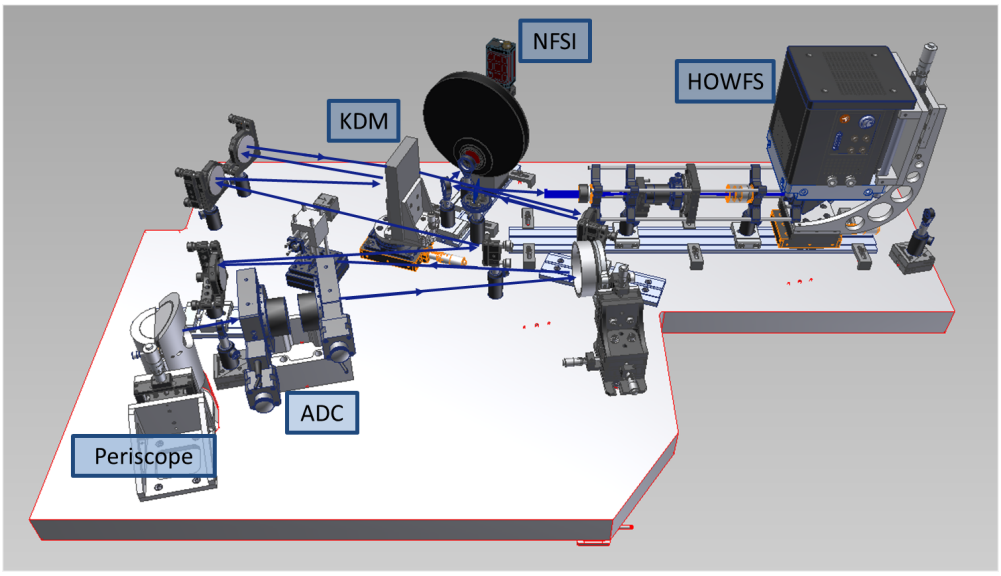

Figure 2.10: CHOUGH 3D-mechanical model.

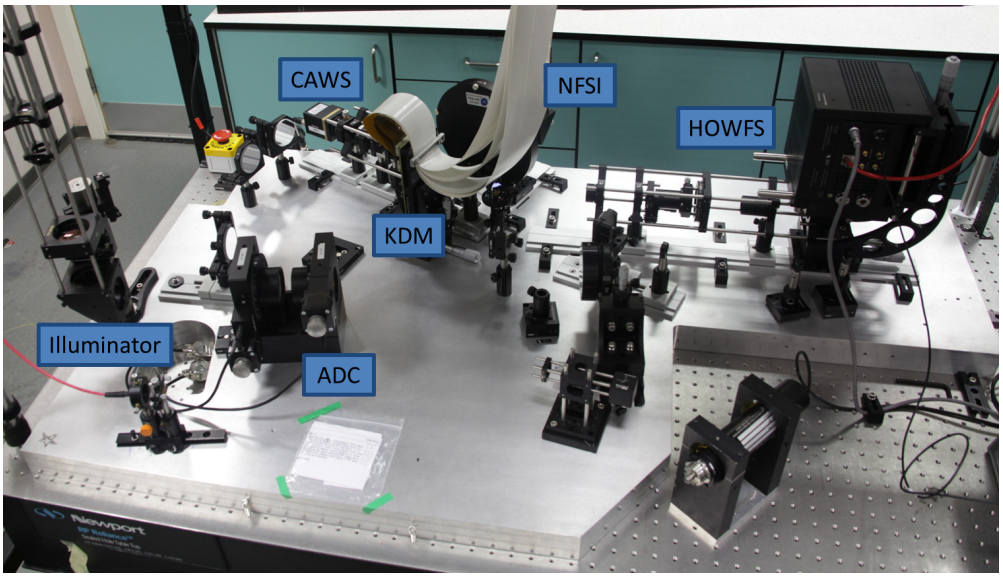

Figure 2.11: Picture of CHOUGH in the laboratory.

In summary, CHOUGH consists of the LODM in CANARY, the 1024-actuator MEMS-DM, the HOWFS, the NFSI, and the ADC.

2.4.1 Optical Relay

Due to the narrow field of view of CHOUGH (7") and the compact output pupil diameter (10.54 mm), CHOUGH has a large $F/\#$ of about 30. This attenuates the effects of spherical aberration, and allows the use of Commercial Off-The-Shelf (CotS) spherical mirrors in the optical relay reducing the need for customised optics.

The light coming from CANARY is brought into CHOUGH through a periscope (for the 3D-model see Figure 2.9 in Section 2.4), bringing the light from CANARY-bench level to CHOUGH-bench level, 445 mm above the CANARY bench. Figure 2.12 presents the Zemax layout of the CHOUGH optical relay, the white arrows represent the beam direction. The collimated beam goes through the ADC to reach an Off-Axis Parabolic (OAP), which is the only customised optics in the system besides the ADC. This OAP resizes the beam to a CHOUGH-sized beam with the right $F/\#$. The beam is folded by two flat mirrors and reaches the first spherical mirror, which collimates the beam and reimages the pupil on the HODM, subsequently there is a pair of spherical mirrors to reimage the pupil into the HOWFS and NFSI. A dichroic redirects the light with a wavelength below 645 nm into the HOWFS, and the rest(>654 nm) goes to the NFSI.
The OAP (Figure 2.13) manufactured by Aperture Optical Sciences, is made of fused silica with protected aluminium coating, and it has a segmented focal length of 1109.03 mm and clear aperture of 50 mm. The three spherical mirrors are CotS from Edmund Optics, they have a focal length of 304.8 mm (12") and diameter of 50.8 mm.100

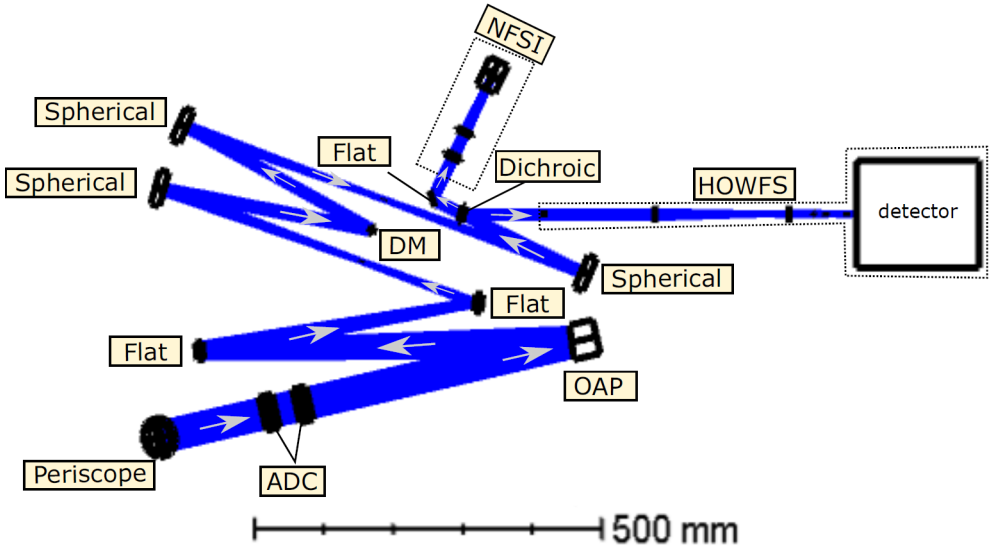

Figure 2.12: CHOUGH optical relay modelled in Zemax.

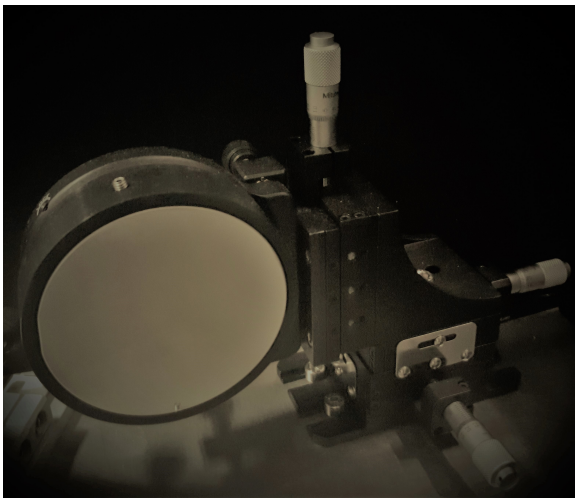

Figure 2.13: Off-Axis Parabola mounted on a 3-axis stage and tip-tilt adjustment.

2.4.2 LODM

The LODM, which is part of CANARY that was extensively tested at CfAI (Bitenc et al., 2014), is an ALPAO DM241 model, 241-actuator DM (Figure 2.14). It is a continuous surface DM motioned by magnetic actuators with large stroke, $\geq$ 25 μm, actuator pitch 2.5 mm, and pupil diameter of 37.5 mm. It has large strokes and high dynamic motion, and is able to correct large amplitude aberrations.

Besides the LODM, CHOUGH has a HODM with high spatial resolution strokes but it does not have high dynamic range, thus, it is not capable of correcting for the full physical range of wavefront aberrations expected to be encountered. CHOUGH works in a closed loop using the CANARY ALPAO DM as a "woofer" mirror(LODM) to corrects for the lower spatial-frequency aberrations.

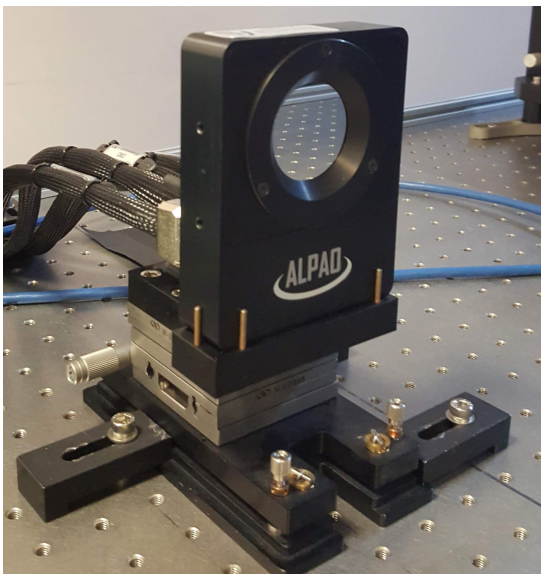

Figure 2.14: ALPAO 241-actuator DM.

2.4.3 HODM

The HODM, also known as Kilo-DM from Boston Micromachines Corporation (Figure 2.15), is a continuous surface MEMS-DM with a 32 x 32 square array of actuators, 1020 active plus the four corner actuators fixed. The mirror is aluminium coated. Its maximum stroke is 1.8 μm at 208 V; the actuator pitch is 340 μm and the active aperture size is 10.54 mm x 10.54 mm. This mirror suits the La Palma site characteristics, spatially and temporarily.

As mentioned previously, CHOUGH works in closed-loop using a "woofer-tweeter" configuration with the LODM correcting for the low-order aberrations and the

HODM correcting for the high-order aberrations. It is because of the limited stroke of this device that wavefront correction is obtained in conjunction with the LODM. The nominal frame rate this DM runs is as fast as the HOWFS, up to $\leqslant$1.2 kHz

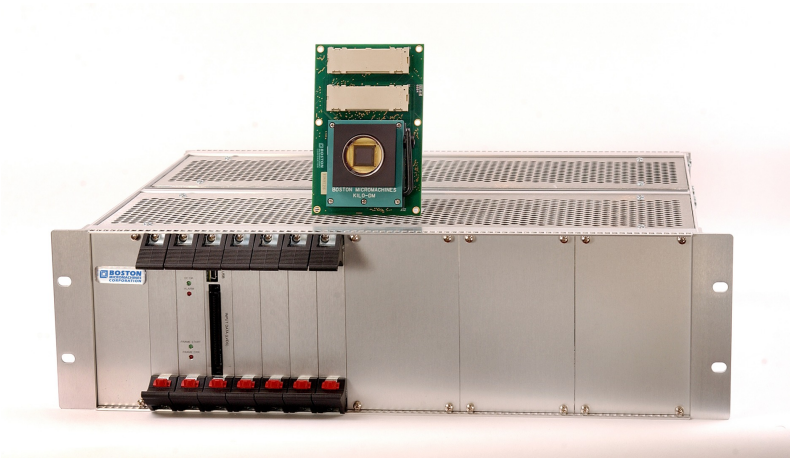

Figure 2.15: kilo-DM. (Image credits: Boston Micromachines Corporation).

2.4.4 HOWFS

The WFS is a central piece in the AO system. The HOWFS is a 31 x 31 Shack-Hartmann wavefront sensor that uses 93 x 93 detector pixels. Each sub-aperture is configured as a quadrant cell and a one-pixel guard-band (3 x 3 in total). The detector is an EMCCD camera, specifically a HNü 128 x 128 Nüvü Camera. Figure 2.16 shows a 3D mechanical model of this Shack-Hartmann WFS. Chapter 3 will present a detailed description of the HOWFS.

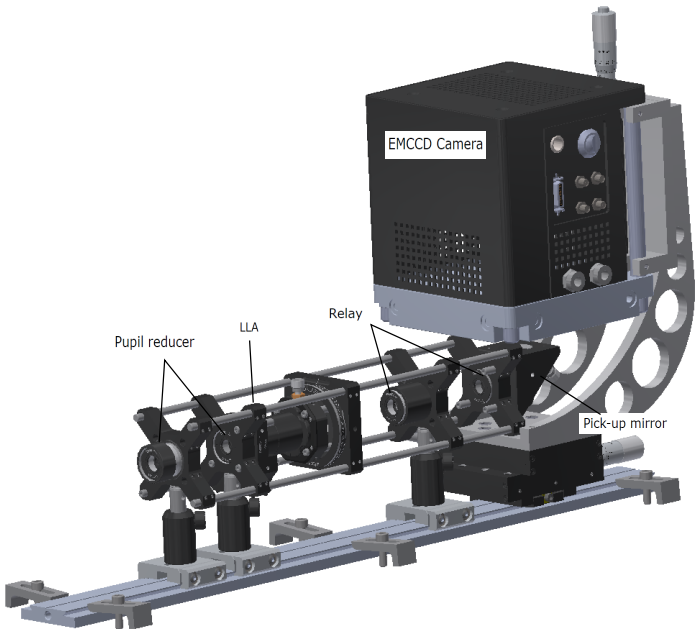

Figure 2.16: 3D mechanical model of the HOWFS.

2.4.5 ADC

The ADC corrects the chromatic dispersion produced by the atmosphere. The ADC design is made up of two plates of cemented double prisms facing each other, separated by 30 mm, as the Zemax model in Figure 2.17 shows. The two plates counter rotate correcting for the different Zenith angles up to 60°. The plates are mounted in rotating stages as shown in the 3D mechanical model in Figure 2.18. Chapter 4 will present a detailed description of the ADC.

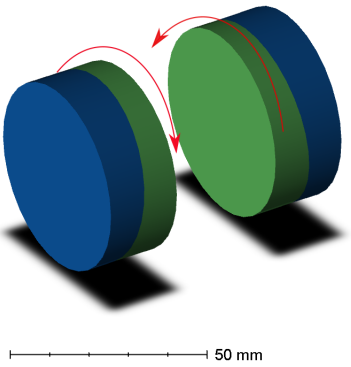

Figure 2.17: Zemax model of the Amici ADC.

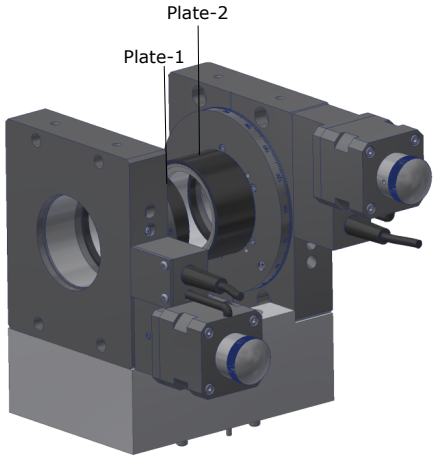

Figure 2.18: ADC Rotation stages 3D-model.

2.4.6 NFSI

The NFSI, produces an image of the field centred around the object used as the WFS reference. The camera is an imager operating in the R - through I - bands with a field of view of 7" and a filter wheel (Figure 2.19). It is an AVT Manta G-145B NIR optimized for the near-infrared and has GigE-Vision interface. The resolution of the camera is 1388(H) x 1038(V), pixel size 6.45 μm x 6.45 μm and frame rate 15.0 fps. The camera's good NIR sensitivity and low cost made it a good choice for the CHOUGH experiment.

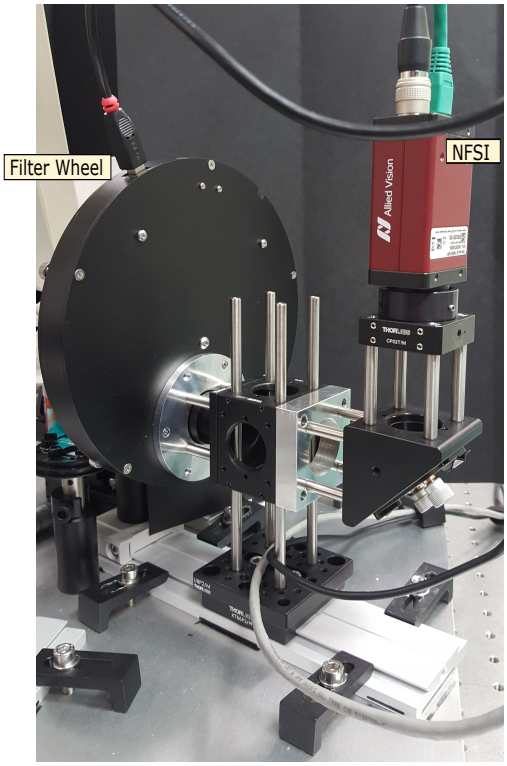

Figure 2.19: NFSI and filter wheel.

The filter wheel has a small variety of narrow- and wide-band filters, listed in Table 2.1. The filters are Edmund Optics (EO) CotS (see the second column in Table 2.1 for part number). They are located into slots on the filter wheel specified in the first column of Table 2.1. The filter wheel does not require a separate power supply when used with USB control. The high performance DC gearmotor runs entirely from the USB supply and consumes less than 100 mA. It is also capable of operating from a serial input, or from a switched hand controller, both of which power the wheel from a small dry battery.

Table 2.1: NFSI Filters.

Slot	EO Part number	Centre Wavelength	FWHM
1	87-757	697 nm	75 nm
2	87-758	732 nm	68 nm
3	84-107	832 nm	37 nm
4	86-358	655 nm	15 nm
5	88-012	700 nm	10 nm
6	65-178	780 nm	10 nm
7	Empty		

The narrow-band filters target spectral features from extended atmospheric or photospheric emission around stars (ionized Hydrogen and cool, extended atmosphere respectively), while the wide-band filters cover the sensitivity of the NFSI detector and are meant for AO research purposes.

2.4.7 The RTC

DARC (Basden et al., 2010) is the RTC system used to interpret the WFS signals and compute the commands that are to be sent to the DM . DARC has a modular design that allows one to customise easily, and can operate the CHOUGH system at $>$ 1kHz.

The DARC's key components are (Basden et al., 2010):

- The Real-time control pipeline (RTCP): It takes the WFS camera data and computes the control vectors to be sent to the DMs.
- Control inter face: It is responsible for allowing the user to update and control the RTCP.
- Diagnostic system: The diagnostic system is an optional component recommended for large systems and is responsible for taking output produced by the RTCP, logging it, and distributing it to clients as requested.

- Graphical and scripting interface: provide easy ways for a user to alter the state of the system via the control interface.

Figure 2.20 represents the CHOUGH-CANARY RTC

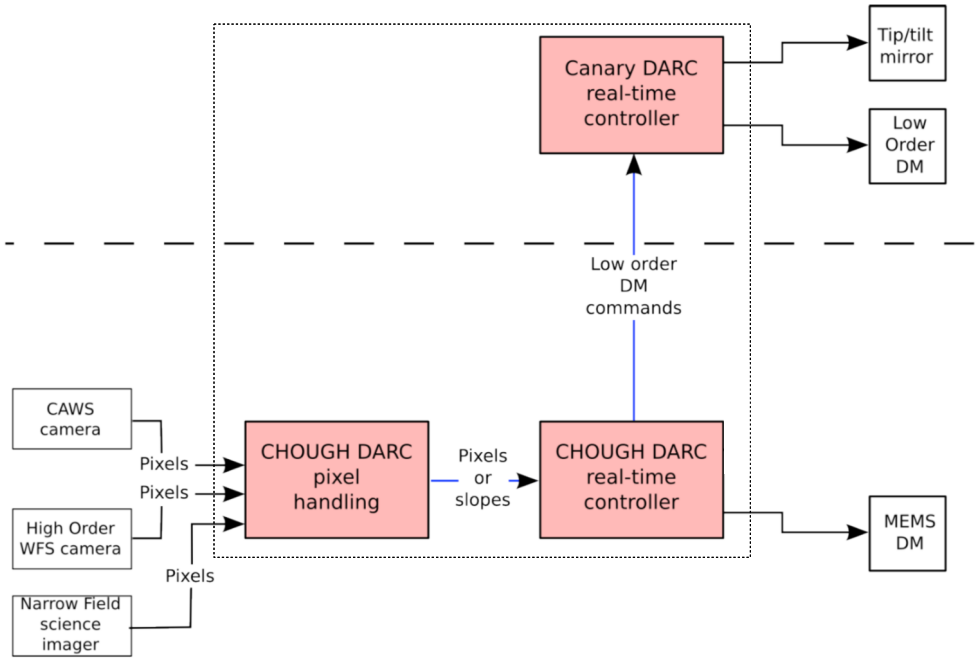

Figure 2.20: CHOUGH-CANARY RTC. (Image credits: Nigel Dipper).

The CAWS (Dubost et al., 2018), was not implemented by the time of the on-sky run because it was not ready.

2.5 Summary

In summary CHOUGH is a small add-on instrument that provides an experimental testbed that aims to achieve high-order SCAO capability in the visible ($>650\,\mathrm{nm}$) for the 4.2 m WHT telescope based in La Palma, Canary Islands. CHOUGH is mounted as an addition to the CANARY experiment.

It went on-sky two nights during October 2016 at the WHT. No prior laboratory testing could be carried out for CHOUGH, and it was assembled on the telescope for the first time. Where only a Strehl ratio of 0.1 at 832 nm with on-bench sources was the best PSF obtained. This was due to Non-common path aberrations (NCPA) compensation and not quite optimal DM control.

Sections 2.4.1 to 2.4.6 outlined the components of the instrument such as: optical relay, ADC, LODM, HODM, HOWFS, and NFSI.

Having described the structure of CHOUGH, the following two chapters proceed to in detail discuss the HOWFS and the ADC subsystems which are the main focus of this thesis.

Chapter 3

High-order Wavefront Sensor

The goal of the WFS is to provide a signal with measurements of the wavefront. The AO system must read the wavefront with enough spatial and temporal resolution in order to correct the aberrations. The WFS in AO is used in real-time operation, and requires to deal with the randomness of atmospheric turbulence; this requires a large number of degrees of freedom. Aiming to reach high order corrections, a High-Order Wave-Front Sensor (HOWFS) represents the central piece of any astronomical HOAO experiment.

The WFS sensor chosen for this project is a Shack-Hartmann WFS type coupled to a high-speed, high-sensitivity detector. The justification for this choice is the experience CfAI has with this type of WFS, since it is analogous to the one delivered by Durham University to the European Southern Observatory (ESO) High-order Test Bench (HOT) (Aller-Carpentier et al., 2008).

This chapter begins by outlining the principles of a Shack-Hartmann. Then, it proceeds to describe the design of the WFS for this project along with the undertaken steps. It concludes by presenting HOWFS laboratory experimental results.

3.1 Shack-Hartmann

This section presents the principle of how a Shack-Hartmann WFS works. A Shack-Hartmann WFS uses a Lenslet Array (LLA) to sample the input wavefront at discrete points across the pupil, and forms a grid of spots on the focal plane of the array (see Figure 3.1). The pupil is sampled by subapertures defined by the microlenses, and local wavefront slopes are measured. Each one of these slopes corresponds to the first derivative of the wavefront. Figure 3.2 represents a planar and a distorted wavefront incident on a single microlens, where δ_y is the total spot shift for an input angle α, described by Equation 3.1.

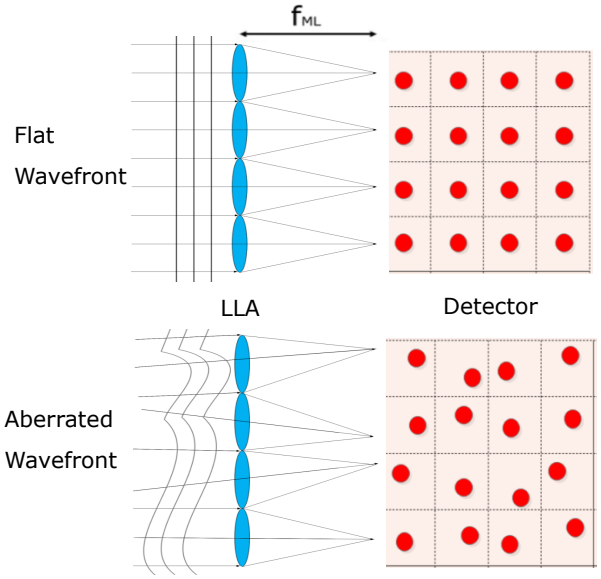

Figure 3.1: Wavefront sampled by LLA.

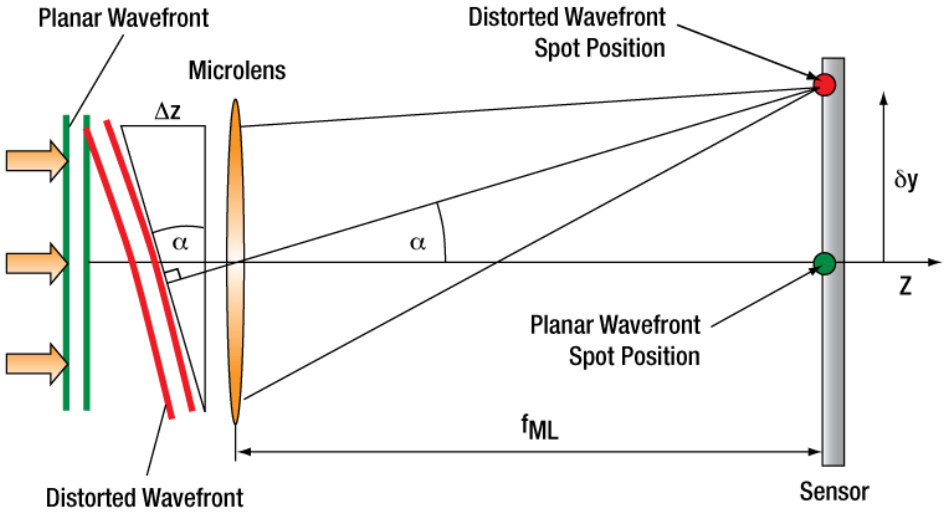

Figure 3.2: Planar and a distorted wavefront incident on a single microlens. (Image credits: Thorlabs Inc.).

$$\delta_y = \alpha f_{ML}. \tag{3.1}$$

3.2 Design

This section describes the steps undertaken to design the Shack-Hartmann WFS for this project, the detector's characteristics, LLA selection, constraints, and optical and mechanical design. The HOWFS was designed to work with wavelengths between 550 - 650 nm. It is worth mentioning that the original design included a variable spatial filter (Poyneer and Macintosh, 2004) to reduce aliasing for high-spatial frequencies. Which was not implemented due to time and budget constraints. Nevertheless, the optical design of the WFS presented here permits installation of such filter as a later upgrade.

3.2.1 Detector

The detector selected for the design is a HNü 128 Electron-multiplying CCD (EMCCD) camera, Figure 3.3. This is a low light detector from Nüvü, 24 μm pixel size, operating at < 1300 Hz.

Figure 3.3: HNü 128 camera. (Image credits: Nüvü Caméras Inc.).

Fried geometry (Figure 3.4) (Fried, 1977), is known to be optimal and with better SNR. Following this configuration where the DM actuators are registered to the corners of a square grid and considering the 32 x 32 actuator array of the Boston kilo-DM, the array of subapertures for the Shack-Hartmann is 31 x 31.

The detector is used in a quad-cell plus a guard-ring configuration to avoid overlapping and facilitate alignment. Figure 3.5 shows a sketch of the configuration. The quad-cell provides information about the position of an incident spot image by comparing the signal received from each of the four separate quadrants. The x and y position of the spot relative to the centre of the device can be determined by Equations 3.2, where A, B, C and D are the intensity measured on each of the four quadrants.

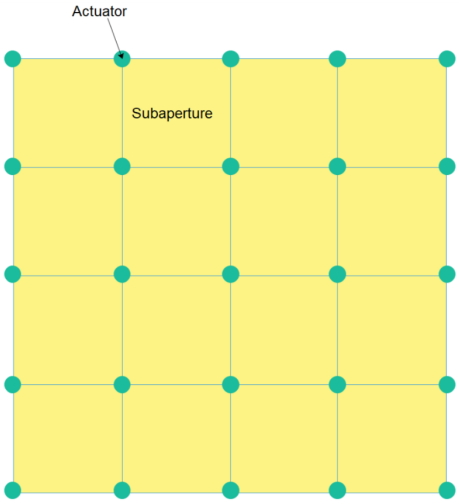

Figure 3.4: Schematic illustration of Fried geometry.

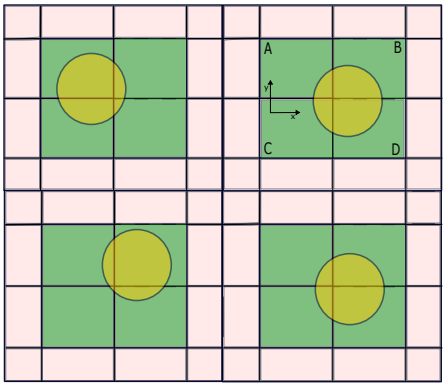

Figure 3.5: Schematic illustration of Shack-Hartmann WFS quad-cells.

$$x = \frac{(B+D)-(A+C)}{A+B+C+D}.$$
$$y = \frac{(A+B)-(C+D)}{A+B+C+D}. \tag{3.2}$$

3.2.2 Lenslet Array(LLA) selection

A LLA consists of a set of lenslets in the same plane. Each lenslet has the same focal length. Figure 3.6 shows an example of a LLA, where the pitch is the distance between the centre of one microlens to the adjacent one, this parameter together with the focal length were fundamental for the LLA selection. The pitch defines the size of the subaperture, and together with the focal length they determine the spot size, as it will be explained next.

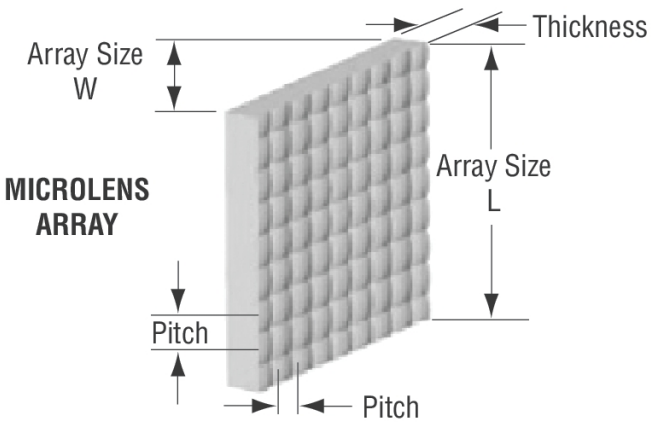

Figure 3.6: Lenslet array parameters. (Image credit: Newport Corporation).

For LLA selection it is crucial that the incident light spot must be smaller than the detector's total active area. Figure 3.7 shows that the spot's semi-angle α is given by the FWHM of a spot. Equation 3.3 gives the semi-angle value.

$$\alpha = 1.03\frac{\lambda}{d_s}. \tag{3.3}$$

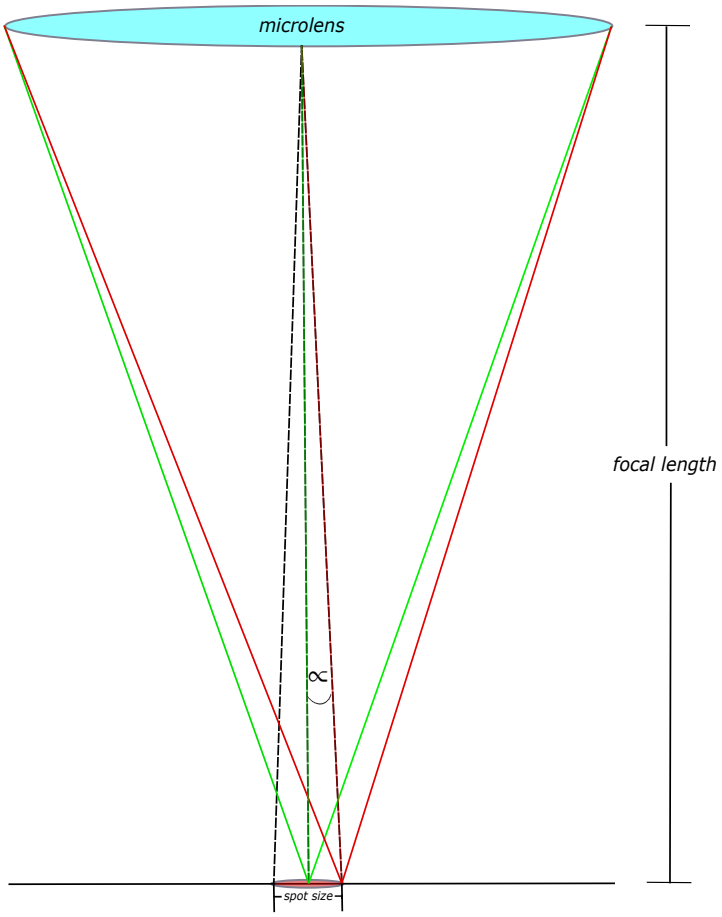

Figure 3.7: Schematic illustration of a single microlens.

where λ is the wavelength and d_s is the subaperture diameter. Using the same principle as in Equation 3.1, the spot radius is given by following equation

$$\frac{\text{Spot Size}}{2} = \alpha f_{ML}. \tag{3.4}$$

The Spot Size is obtained replacing α from Equation 3.3 into Equation 3.4.

$$\text{Spot Size} = \frac{2.06\lambda f_{ML}}{d}. \tag{3.5}$$

Since the spot has to be smaller than the subaperture $\frac{2.06\lambda f_{ML}}{d_s} < d_s$, from Equation 3.5 it is inferred that the maximum focal length allowed for the microlenses

will be

$$f_{ML} < \frac{d_s^2}{2.06\lambda}. \tag{3.6}$$

Applying Equations 3.5 and 3.6, the best suitable LLA available in the market that would fit CHOUGH's requirements is a LLA from SÜSS, 110 μm pitch and 5.786 mm focal length. The resulting theoretical spot size on the focal plane of this LLA, at a wavelength of 550 nm according to Equation 3.5 is 58.67 μm. The subaperture defined by the LLA is 110 μm and the subaperture at the detector defined by the quad-cell and the guard ring (3×3 pixels) is 72 μm. Since the subapertures defined by the microlenses are larger than the subapertures on the detector, it was necessary to design an optics relay, with a demagnification of 0.65 to match the LLA's subapertures to the detector. The 58.73 μm spot when demagnified has its diameter size reduced to 38.17 μm. When a gap between the microlenses is considered, which for this type of LLA can go up to p - 0.9ϕ (Nussbaum, 2000), where ϕ is the lens diameter and p the LLA pitch. The spot size can reach a diameter of 65.19 μm at the focal plane of the LLA and 42.37 μm at the camera's focal plane.

3.2.3 Optical & Mechanical Design

Once the LLA specifications and the detector pixel size to match the AO design were identified, it was possible to choose all the other optics components freely. These components are all CotS, from EO. Since the microlenses have larger diameter than the subapertures on the detector, and as it was mentioned before, it was necessary to design an optics relay to match the subapertures on the detector. Each microlens corresponds to a subaperture and each subaperture on the detector has 3 pixels (72 μm) across it. 31 subapertures give a total of 93 pixels across

the pupil and a total pupil diameter on the detector of 2.323 mm. In addition, the input beam coming from the HODM has a diameter of 10.54 mm. In order to match this pupil to the 3.4 mm pupil on the LLA some foreoptics had to be added to reduce the pupil diameter, Figure 3.8 shows the Zemax 3-D optical model. The design was restricted to fit in a space < 500 mm. The HOWFS optics consist of two parts: a pupil reducer before the LLA and a relay after LLA focal plane. The design allows a spatial filter to be placed in the focal plane inside the pupil reducer, as indicated in the figure below.

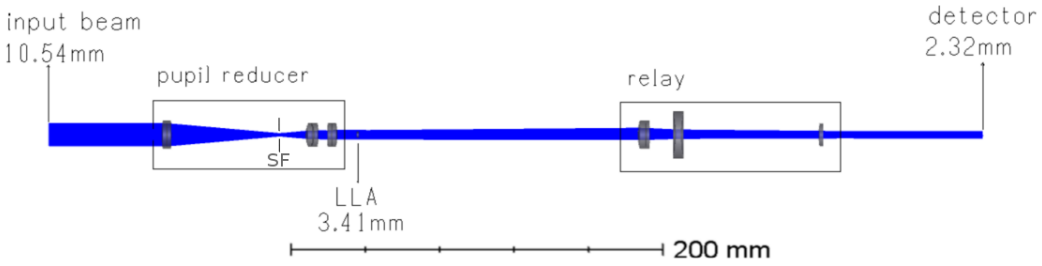

Figure 3.8: HOWFS optical design.

3.2.3.1 Pupil reducer

The Pupil reducer brings the pupil down from 10.54 mm (DM diameter) to 3.41 mm (31 LLA subapertures). It contains three lenses. The first Lens [f1=60 mm] brings the 10.54 mm pupil to focus, as it was taken into account to leave room for placing a spatial filter in the future. The other two lenses [f2=25 mm] [f3=50 mm] recollimate the beam to a 3.41 mm diameter pupil onto the Microlens Array (MLA). The reason to use two lenses after the focus is to have control of the focal length in case of manufacturing errors or any other source of error. Matching the pupil to the LLA correctly is very important; otherwise, phase information could be lost

due to incorrect sampling.

Table 3.1: HOWFS pupil reducer optics.

EO part number	**Effective Focal Length (EFL)**	**Diameter**
49954	60.0mm	15mm
65971	25.0mm	12.5mm
45125	50.0mm	12.0mm

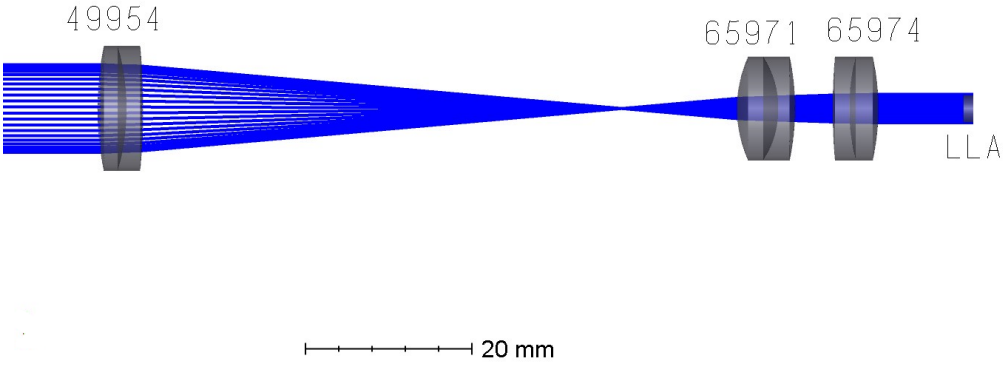

Figure 3.9: Pupil reducer.

3.2.3.2 Relay

The relay translates the spots from the MLA focal plane to the detector's focal plane. The main inconvenience when designing this section was the spherical aberration around the edge of the Shack-Hartmann spot grid on the camera. Spots

would not fall onto the centre of the quad-cell and also the telecentricity of the WFS would be affected.

The spherical aberration is produced when there is variation of focus position with the aperture. Rays that are very close to the optical axis will come to focus at the paraxial image position, as the ray height increases above the optical axis, the rays will focus closer to the lens. Spherical aberration is proportional to the cube of ray height incident onto the lens. A common way of reducing the spherical aberration is reducing the angle of incidence, thus increasing the focal length, and as consequence results in a smaller deviation between paraxial rays and real rays. The inconvenience of this is that the length of the WFS cannot be increased due to the lack of space in CHOUGH. Another way of dealing with spherical aberration is splitting the power in multiple lenses that have the total power of the original single lens. This is very effective because spherical aberration is highly dependent on the angle of incidence. The problem was solved using a combination of converging and diverging lenses. The relay to re-image the LLA focal plane is composed of three lenses [f=50 mm][f=-50 mm][f=72 mm], these lenses are listed in Table 3.2. Figure 3.10 shows the Zemax layout of the relay. This selection of lenses attenuated the spherical aberration, centred the spots and the system stayed telecentric.

Table 3.2: HOWFS relay optics.

EO part number	**EFL**	**Diameter**
45138	50.0 mm	15 mm
32996	-50.0 mm	25.0 mm
45125	72.0 mm	12.0 mm

Figure 3.11 shows the spot diagram generated with Zemax, after the light goes through the HOWFS optics as in Figure 3.8

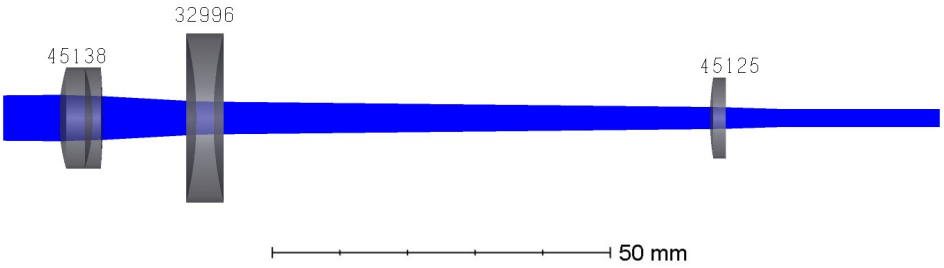

Figure 3.10: HOWFS relay.

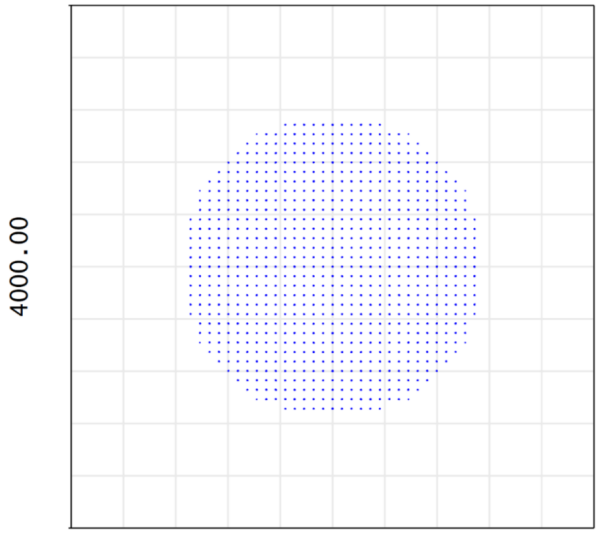

Surface 32: image

Full Field Spot Diagram

07/11/2018
Units are µm. Legend items refer to Wavelengths

RMS radius : 799.244
GEO radius : 1169.57
Box width : 4000 Reference : Chief Ray

Figure 3.11: Zemax HOWFS spot diagram.

3.2.3.3 Mechanical design

The mechanical design is rail mounted to aid shipping of CHOUGH. All the mechanical parts are CotS. The distance between the pair of lenses after focus are adjustable in order to have control over the collimation of the beam illuminating the array of microlenses. The LLA is in an x-y translation mount combined with a cage rotation mount, this allows to align the LLA axes to the HODM and adjust the LLA along the axes.

Due to the limited space in CHOUGH and the large size of the camera (Figure 3.3) a fold mirror is used to connect the relay to the camera, as shown in the 3D-model in Figure 3.12 and a picture of the WFS in the laboratory, Figure 3.13.

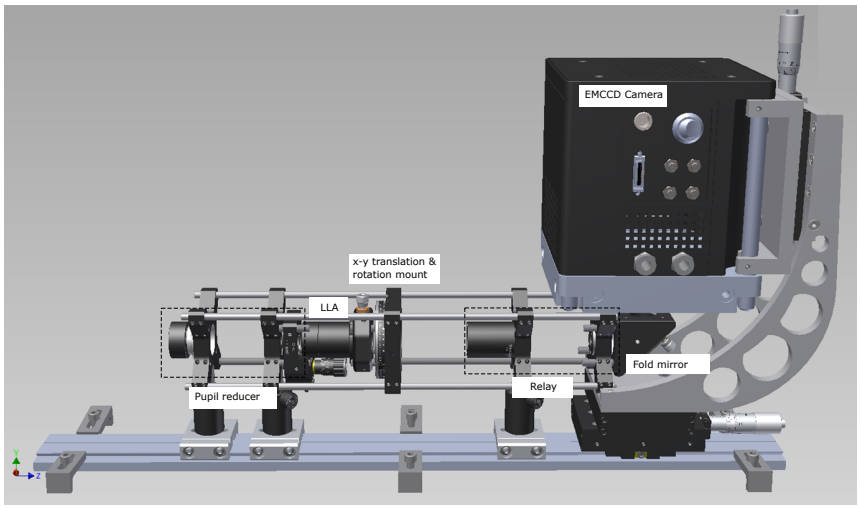

Figure 3.12: Mechanical model of the HOWFS.

The HOWFS camera is mounted on three translation stages allowing three degrees of freedom for the camera; x, y and z axes. Figure 3.14 shows the 3-D mechanical model (designed by Marc Dubbeldam) on which the Nüvü camera is mounted. The translation stages are from Thorlabs inc. One of them is a translation stage with standard micrometer, 1/4”-20 taps corresponding to the x-axis, and the others are two 25 mm translation stages with a standard micrometer and

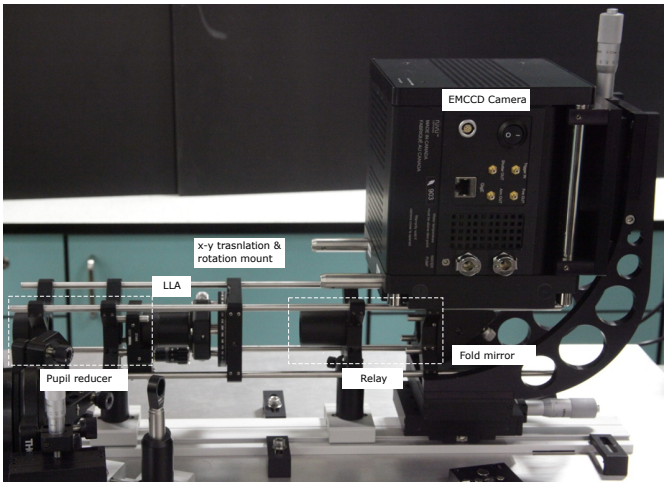

Figure 3.13: HOWFS in the laboratory.

M6 taps for the y and z axes. Figure 3.15 shows a picture with the two types of translation stage: the top stage is the PT1 model aligned to the x axis; the bottom stage is the PT1/M model for the corresponding y and z axes.

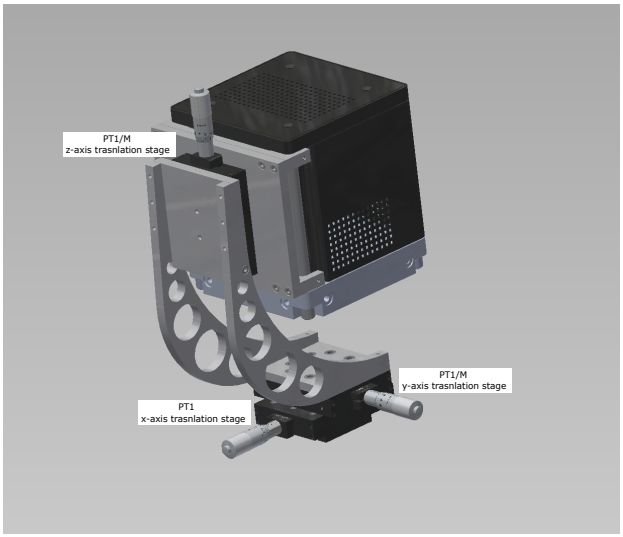

Figure 3.14: Camera mount 3D mechanical model.

Figure 3.15: Camera Translation Stages. Top: PT1 x-axis, Bottom: PT1M y-axis and z-axis. (Image credits: Thorlabs Inc.).

3.3 HOWFS plate scale

The plate scale connects the angular separation of an object on the sky, with the linear separation of its image at the focal plane on the detector. In the CHOUGH case, it relates the subtended angle θ_{wht} of an object on the sky observed with the WHT, and how many arcseconds per mm are on the WFS's detector. Figure 3.16 presents a schematic of the scaling described above.

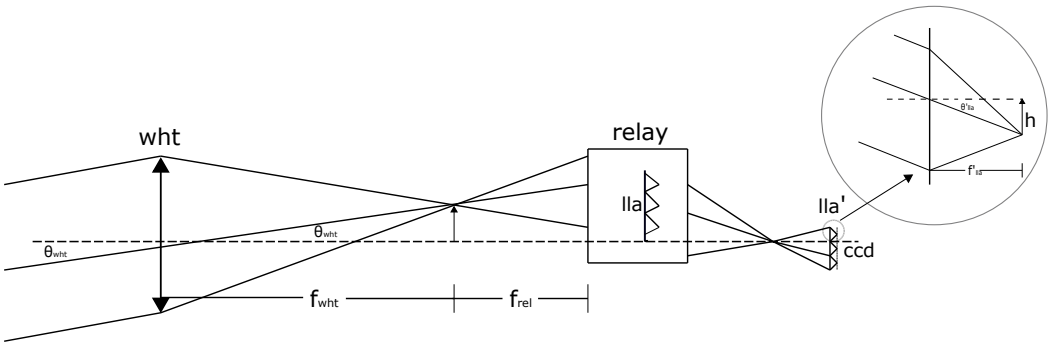

Figure 3.16: Schematic of HOWFS plate scale.

The demagnification of the LLA can be calculated from the ratio between ϕ, the diameter size of a single lenslet of the LLA and ϕ', the diameter of the 3 x 3 pixel subaperture on the detector.

$$m = \frac{\phi'}{\phi} = \frac{72}{110}.$$

then the scaled focal length of the LLA at the detector's focal plane is

$$f'_{lla} = f_{lla} \times m^2 = 5.78 \times \left(\frac{72}{110}\right)^2 = 2.48\,\text{mm}.$$

The $f/\#$ of the WHT is 11. This has to match the $f/\#$ of the relay optics up to the detector's plane in order to sample correctly the telescope's pupil. The pupil goes down from 4.2 m on the telescope to 2.232 mm on the detector. From this we can deduce the focal length of the relay optics, f_{rel}, up to the detector.

$$f/\# = 11 = \frac{f_{rel}}{2.232} \rightarrow f_{rel} = 24.55\,\text{mm}.$$

If a spot on the detector displaces a distance h from its nominal position, from Figure 3.16 it is possible to say the angle θ'_{lla} is

$$\theta'_{lla} = \frac{h}{f'_{lla}}.$$

and if it is scaled by the angular magnification m_a for the WHT one obtains the angle subtended by the object on sky.

$$\theta_{wht} = \theta'_{lla} \times m_a.$$

Given that the m_a for paraxial angles is the ratio of the focal lengths of the two systems; the telescope and the relay

$$\theta_{wht} = \frac{h}{f'_{lla}} \times \frac{f_{rel}}{f_{wht}}.$$

if the spot displaces 1 mm from the centre of the microlens, the angle on the sky

would be given by

$$\theta_{wht} = \frac{1}{2.48} \times \frac{24.55}{46200} = 0.00021\,\text{rad} = 43.32\text{”}$$

$$\boxed{Plate\,Scale_{wfs} = 43.32\left[\frac{\text{arcsec}}{\text{mm}}\right]}.$$

Given this plate scale, the range the HOWFS can measure per subaperture on the 48 μm quad-cell is an angle of ± 1.04 arcseconds.

Having discussed the theoretical foundations, the next sections presents experiments performed to confirm the HOWFS's design.

3.4 Spot Size Measurement

The Nüvü camera pixels are $24\,\text{x}\,24\,\mu$m and the theoretical size of the spot is 45.84 μm. That is less than 2 pixels of CHOUGH's WFS detector making it not possible to get a sensible measurement of the spot diameter. A camera with smaller pixels was used for the experiment instead, a $9.9\,\text{x}\,9.9\,\mu$m pixel size camera. Figure 3.17 shows the Shack-Hartmann spots focused on this camera, and a single spot from the same image. The x and y cross-section of the spot are shown in Figure 3.18. The FWHM was measured for 10 spots resulting in an approximate average of 43.2 μm. The FWHM was computed using the Python package optictools*.

$43.2 \pm 1.7\,\mu$m does not match the 58.73-65.19 μm theoretical value obtained in section 3.2.2. After alignment, the only parameter that could explain this discrepancy in spot size is a difference in the actual focal length of the LLA.

*$https://github.com/xmhk/optictools$

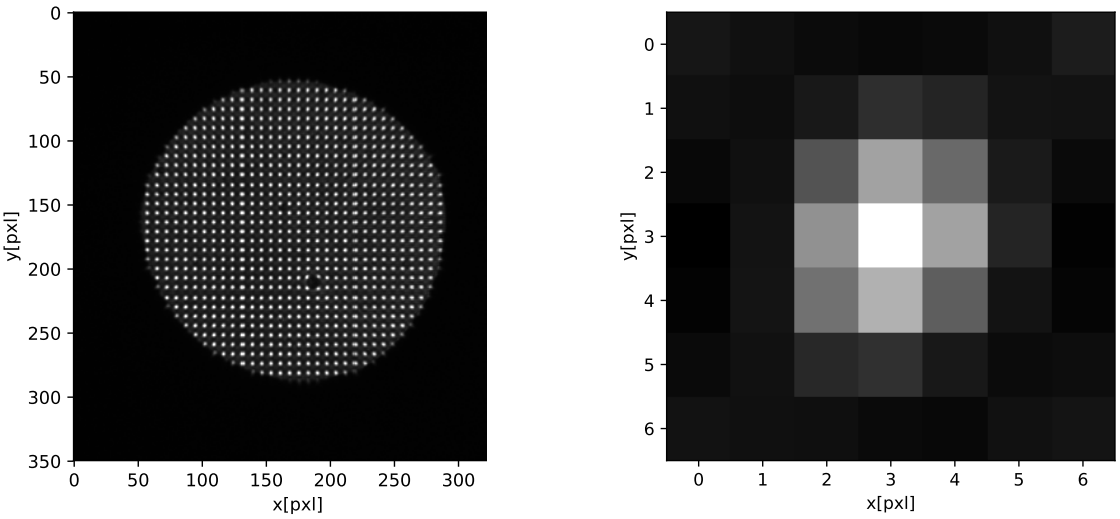

Figure 3.17: Shack-Hartmann spots.

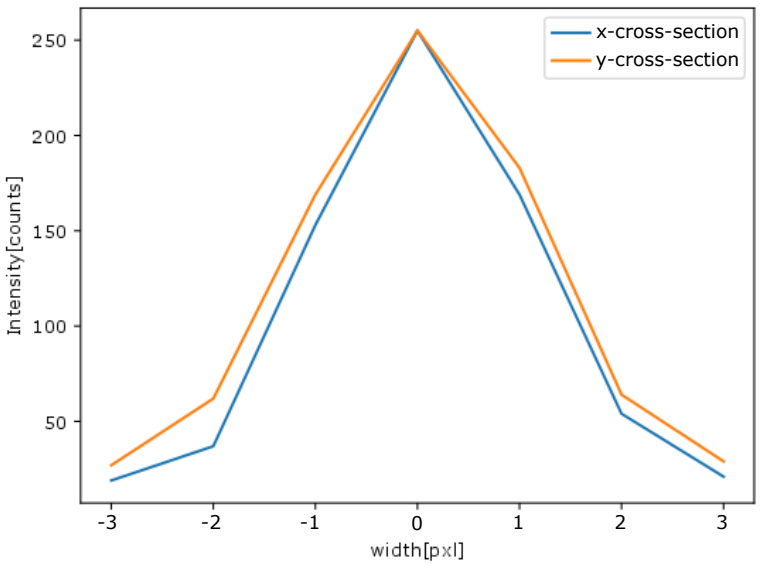

Figure 3.18: Shack-Hartmann spot cross-section.

From Equation 3.5 the focal length can be calculated given the spot diameter by

$$f = \frac{d_s \times SpotSize}{2.06\lambda}. \tag{3.7}$$

If the spot diameter obtained in the experiment, $43.2 \pm 1.7\,\mu$m, is replaced in Equation 3.7 together with the microlens diameter, and wavelength 589 nm, the focal length is obtained. There is a range of focal lengths, if the spot size error, and the minimum and maximum microlens diameter are taken into account. These are arranged in Table 3.3, where the maximum and minimum focal lengths are marked in yellow.

Table 3.3: LLA focal length measured in the laboratory applying Equation 3.7, considering the measurement error and microlens diameter interval. ϕ is the microlens diameter, and p is the pitch size of the LLA. $\lambda = 589$ nm.

Measured spot size (μm)	43.2 - 1.7		43.2 + 1.7	
Microlens diameter (μm)	$\phi = p$	$\phi = 0.9\,p$	$\phi = p$	$\phi = 0.9\,p$
Focal length (mm)	3.76	3.39	4.13	3.72

This result is a closer match to the focal length of another LLA in the SÜSS catalogue, it has the same characteristics as the LLA expected but different focal length. The two LLA are compared in Table 3.4. LLA Nr. 18-00013 is the LLA currently mounted in CHOUGH

Table 3.4: LLAs Comparison.

LLA Nr. 18-00013	**LLA Nr. 18-00014**
Fused Silica	Fused Silica
Circ. lenses	Circ. lenses
Quad. grid	Quad. grid
Pitch 110 μm	Pitch 110 μm
ROC 2.650 mm $\pm$5 %	ROC 1.561 mm $\pm$5 %
Focal length 5.780 mm	Focal length 3.408 nm
Size 10 x 10 $\pm$0.05 mm	Size 10 x 10 $\pm$0.05 mm
Thickness 1.2 mm	Thickness 1.2 mm

3.5 The Interaction Matrix

The interaction matrix relates the response of the WFS to the DM strokes, and as mentioned in Chapter 1, the interaction matrix **P** is used to produce a control matrix, which is generated by creating a pseudo-inverse of a measured interaction matrix, and this matrix gives the commands to the DM to correct for the aberrated wavefront.

The interaction matrix is built by poking one actuator at a time by one unit and measuring the resulting response $\vec{s}$, in an m vector that is read by the Shack-Hartmann, and repeat this measurement for each one of the n actuators. This can be illustrated using Equation 3.8 which represents the maths model for this AO interaction.

$$\vec{s} = \mathbf{P}\vec{c}. \tag{3.8}$$

where $\vec{s}$ is the local wavefront slopes produced by the deformable mirror as seen by the WFS; $\vec{c}$ is the n actuator commands, producing an n vector; and **P** is the m×n interaction matrix. Expanding Equation 3.8 into its bracket form

$$\begin{bmatrix} s_1 \\ \\ \vdots \\ \\ s_m \end{bmatrix} = \begin{bmatrix} p_{11} & \cdots & p_{1n} \\ & & \\ \vdots & & \vdots \\ & & \\ p_{m1} & \cdots & p_{mn} \end{bmatrix} \begin{bmatrix} c_1 \\ \vdots \\ \\ c_n \end{bmatrix}$$

and then applying the actuator command $c_1 = 1$, $c_2 = c_3 = \cdots c_n = 0$, and measuring the m local wavefront slopes s_1, s_2, $\cdots$, s_m produced by the DM deflecting the light.

$$\begin{bmatrix} s_1 \\ \\ \vdots \\ \\ s_m \end{bmatrix} = \begin{bmatrix} p_{11} & \cdots & p_{1n} \\ & & \\ \vdots & & \vdots \\ & & \\ p_{m1} & \cdots & p_{mn} \end{bmatrix} \begin{bmatrix} 1 \\ \vdots \\ 0 \end{bmatrix} = \begin{bmatrix} p_{11} \\ \vdots \\ p_{m1} \end{bmatrix}$$

then the command $c_1 = 0$, $c_2 = 1$ $c_3 = \cdots c_n = 0$, etc. in turn to $c_1 = c_2 = \cdots c_{n-1} = 0$, $c_n = 1$ to get

$$\begin{bmatrix} p_{12} \\ \vdots \\ p_{m2} \end{bmatrix}, \cdots, \begin{bmatrix} p_{1n} \\ \vdots \\ p_{mn} \end{bmatrix}$$

to fill in the interaction matrix $\mathbf{P}$. Figure 3.19 illustrates this process, the top figure represents a 4×4 subaperture configuration (yellow) with guard ring on a 5×5 actuator grid (green). The bottom figure is the interaction matrix plot produced by poking the DM actuators one at the time. The horizontal axis is the subaperture index, and vertical axis the actuator index. Coloured subapertures are influenced by the action of the actuators displacing the centroids; the red (+) colour represents the centroid moving on the positive axis direction and blue (-) on the negative axis direction. For example: The poking of actuator-1 is seen by

subaperture-1 only, actuator-2 is seen by subapertures 1 and 2, and son on. Figure 3.20 shows how a simulated 8×8 interaction matrix looks.

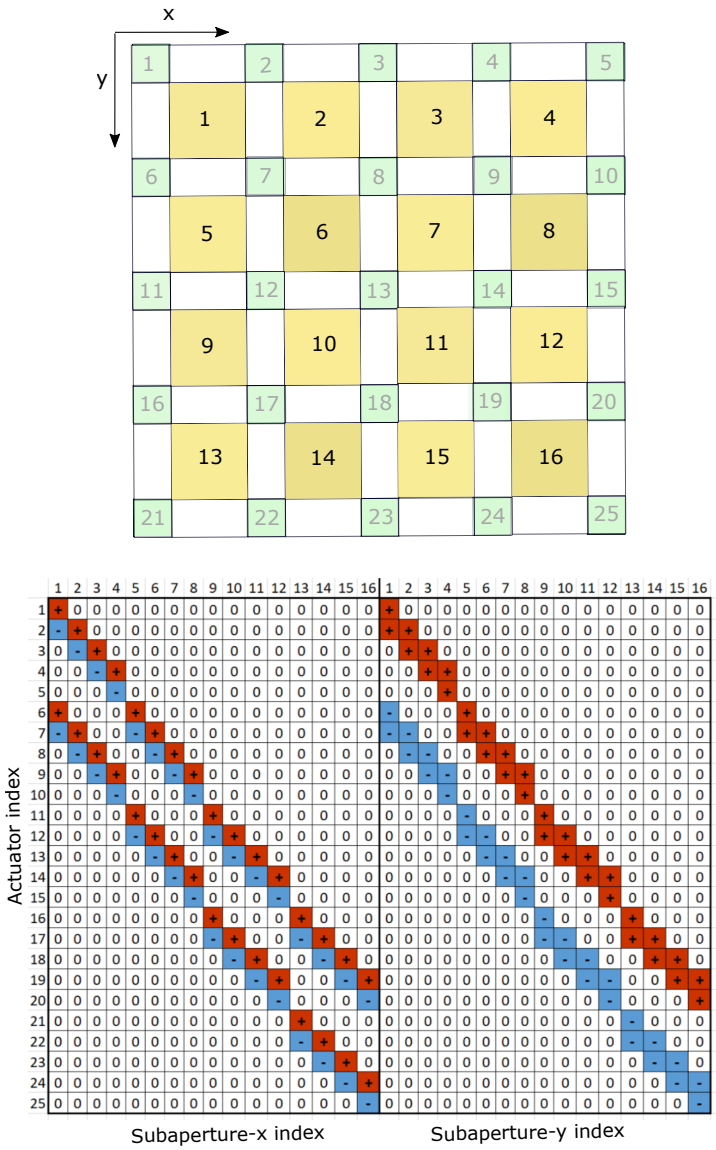

Figure 3.19: Top: 4×4 subaperture configuration (yellow) with guard ring on a 5×5 actuator grid (green). Bottom: interaction matrix plot produced by this configuration.

An interaction matrix was obtained in the laboratory using CHOUGH and the procedure described above. Figure 3.21 shows this matrix (top), where the x-axis is the slope index, with the first half being the slopes in the horizontal direction, and the second half being the slopes in the vertical direction, thus the x-axis is twice

the length of the number of subapertures; The y-axis is the actuator index. The interaction matrix shows that the HOWFS responds accordingly to the actuators strokes.

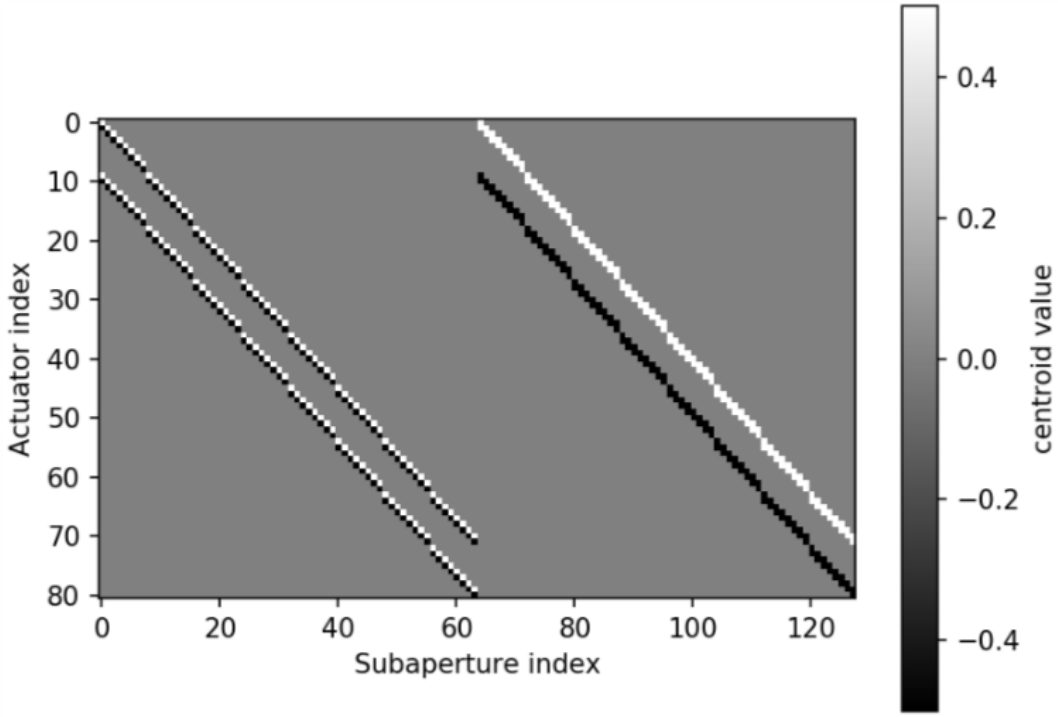

Figure 3.20: 8×8 Subaperture simulated interaction matrix.

The WFS was compared with a Python based model *. A model that provided the parameters generates an artificial interaction matrix. A modified version of this code was used to fit an artificial interaction matrix to the one obtained in the laboratory experiment. The bottom image in Figure 3.21 shows the fitted interaction matrix.

The normalized model-data residual variance is 12,25 %. The fitted interaction matrix shows a rotation of 0.21° with respect to the DM subapertures. This is consistent with a small mechanical rotation observed in the laboratory, later corrected roughly by the use of shims.

*$https://gitlab.cfai.dur.ac.uk/nab_durham/ABBOT$

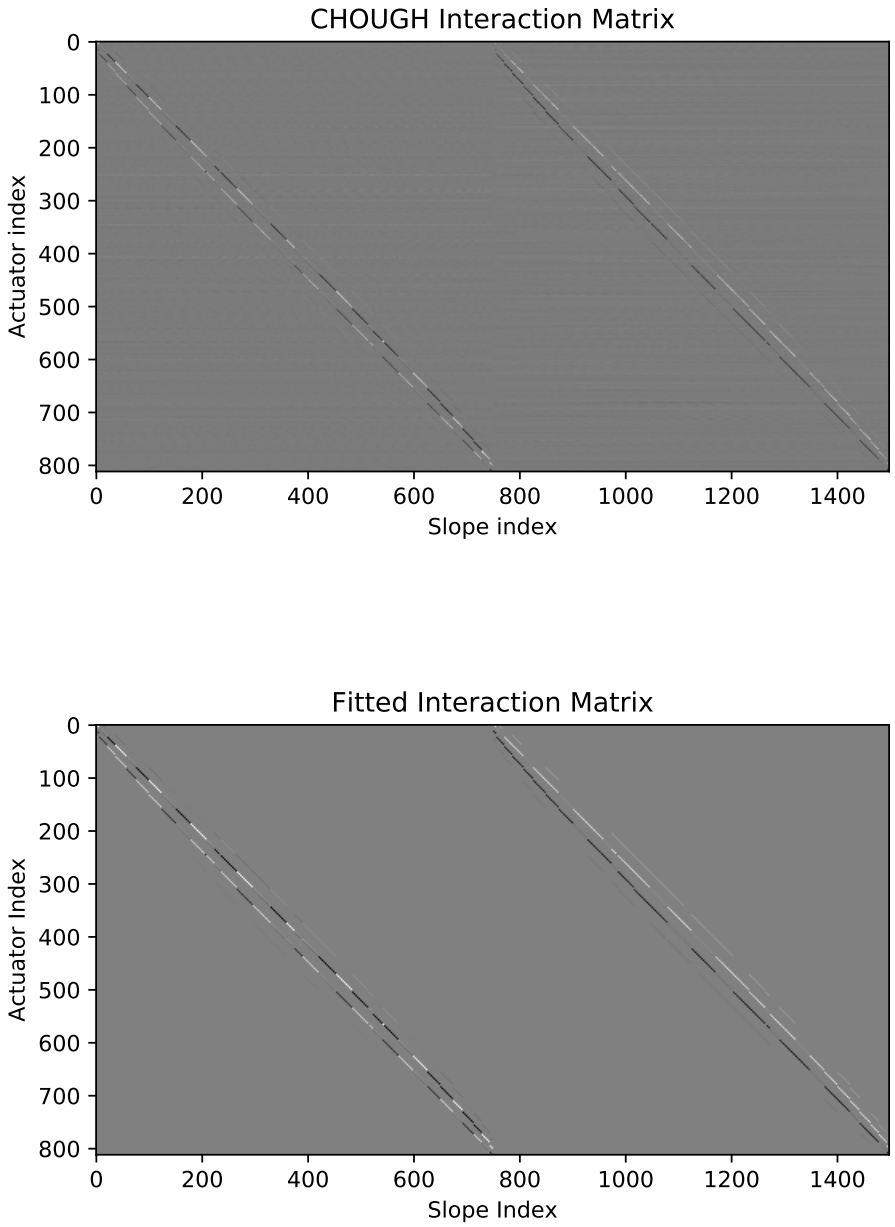

Figure 3.21: A measured (top) and modelled (bottom) interaction matrix between the HODM and the HOWFS.

3.6 Conclusions

The wavefront sensor is a central piece in the AO system. This is a WFS for HOAO using CotS components. The optical design was presented here, as well as an overview of the mechanical design and the Nüvü.

The parameters of the actual Shack-Hartmann tested in the laboratory match the design except for the focal length of the LLA. The microlenses have a different focal length to the one prescribed in the design. This focal length is shorter and makes the Shack-Hartmann spots smaller. A bigger spot size would have been easier to measure, and to align, however the smaller spots do not affect the correct operation of the WFS and CHOUGH. In the absence of sky background noise, and gaps between pixels, the operation of a quad-cell geometry Shack-Hartmann WFS is unaffected by the spot size, provided the spot is not so big as to reach the pixel boundary.

Laboratory verification of astronomical instruments is very important, it is when the instrument can be tested under a controlled environment and permits a better understanding of the instrument operation and performance. Additionally this allows a deterministic way to prove that the numerical model works.

The numerical model was confirmed in the laboratory, thus this demonstrates the HOWFS works according to the design.

Chapter 4

Atmospheric Dispersion Corrector

The refractive power of the atmosphere is dependent on the wavelength of light and zenith angle. Different wavelengths are refracted by different amounts, producing a prism-like effect (Figure 4.1). So the image affected by chromatic dispersion consists of a series of images, each of a different wavelength, slightly shifted relative to each other, and thus causing PSF elongation.

When observing at a wide range of wavelengths the atmospheric chromatic dispersion can limit the spatial resolution (Wynne and Worswich, 1986), and this limit cannot be overcome by the AO system unless it is equipped with an ADC. CHOUGH operates in the visible spectrum of light, over the spectral range of 510 nm to 880 nm. Since the chromatic dispersion effect increases as we approach the horizon, chromatic errors become more noticeable (Devaney et al., 2008). CHOUGH aims at Strehl ratios of 0.5 and to reach zenith distances up to 60°. Figure 4.2 presents a simulated PSF for different zenith angles, where it can be observed that at 15° from zenith the Strehl ratio is already below 0.5, thus it is very important to implement an ADC in the AO system.

This chapter begins by outlining how the conditions at the ORM were simulated. The chapter then turns to the design of the ADC. Finally the chapter describes the experiments run at the CfAI laboratories and results obtained.

4.1 Simulation of Site Atmospheric Chromatic Dispersion

It is necessary to implement an ADC in the AO system in order to compensate for the atmospheric chromatic dispersion, so that the spatial resolution limit achievable with CHOUGH can be increased.

The chromatic effects produced by the atmosphere in our particular case were analysed with the help of the software Zemax Optics Studio. The parameters utilised in the model match the site conditions at the ORM observatory: 2400 m elevation, 283 K, 780 mb pressure, 50 % relative humidity at 33° of latitude. Table 4.1 summarises the parameters used for this model.

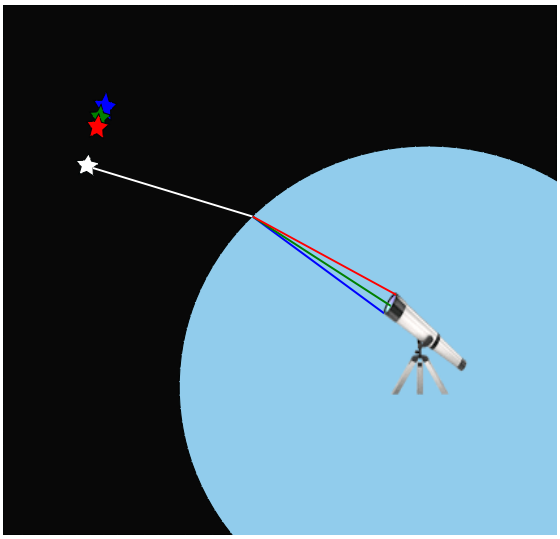

Figure 4.1: Atmospheric Chromatic Dispersion Illustration.

Figure 4.2 shows a simulated PSF for different zenith angles for a telescope of diameter 4.2 m and a focal length 46.2 m as it is the case of the WHT. The simulation shows that the PSF is severely degraded due to atmospheric chromatic effects as the zenith angles are increased.

Table 4.1: Parameters considered in the simulation.

Wavelength	510 - 880 nm
Max. zenith distance	60°
Altitude of the site	2400 m
Temperature	283 K
Pressure	780 mb
Humidity	50 %
Telescope coordinates	28° 45' 37.7"
Latitud	33.000°

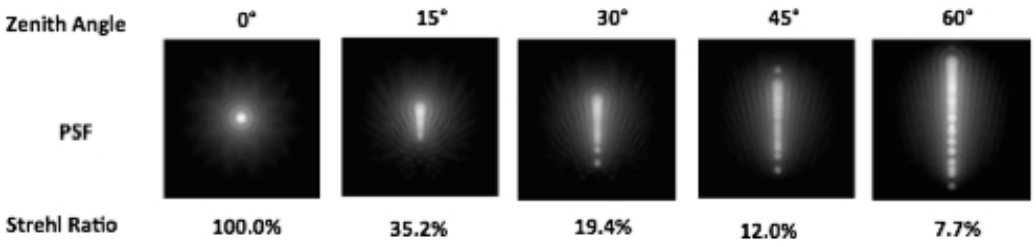

Figure 4.2: The effect of atmospheric dispersion upon the PSF at 510 - 880 nm. Note that the PSFs are log-scaled and wavelength range is discretised.

Considering the limited space to place an ADC inside CHOUGH, the Amici (Bahrami and Goncharov, 2011) counter-rotating-prisms ADC type was considered appropriate for the task. However, this type of ADC induces a shift in the pupil position when rotating. Usually to avoid pupil actuator-lenslet array mismatch, the ADC is customarily placed very close to the pupil plane, which is not possible in CHOUGH due to space restrictions, therefore, this ADC design requires one to produce minimal pupil shift ($< 0.3\,\%$) due to the strict requirement of HOWFS and DM pupil stability. Due to space requirements this design aims to achieve a non-pupil conjugated ADC suitable to be located in any place inside the collimated beam path.

4.2 The Design

As mentioned above, the ADC design is of the Amici variety. It is made up of two plates of cemented double prisms facing each other as shown in Figure 4.3. The ADC will show its maximum dispersion when the apex angles of the prisms are in the same directions and zero dispersion when opposite. The two plates counter-rotate through 90° correcting for different zenith angles, and producing different dispersion at different rotation angles; this dispersion is different in magnitude for each wavelength. So it is possible to say there is a dispersion ratio between wavelengths, and the scaling of these ratios is controlled by rotating the plates. This is the principle by which the ADC operates to correct the atmospheric chromatic dispersion for different zenith angles. Therefore, it will be necessary to build a Look-Up Table (LUT) considering the zenith angle and ADC rotation angles when on-sky.

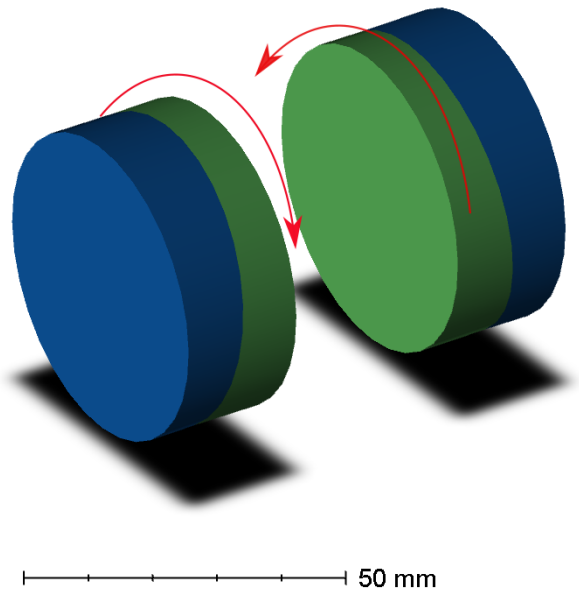

Figure 4.3: Zemax 3D-model of the Amici ADC. S-BAM4 (Blue), S-TIM3 (Green).

Each plate is made of two prisms, one of higher refraction index than the other and thus lower dispersion. The glass type chosen for the CHOUGH ADC prisms are S-BAM4 (higher dispersion) and S-TIM3 (lower dispersion) from the OHARA glass catalogue. Glass dispersion for both materials is plotted in Figure 4.4, showing S-BAM4 more dispersive than S-TIM3. The prisms are 50 mm in diameter,

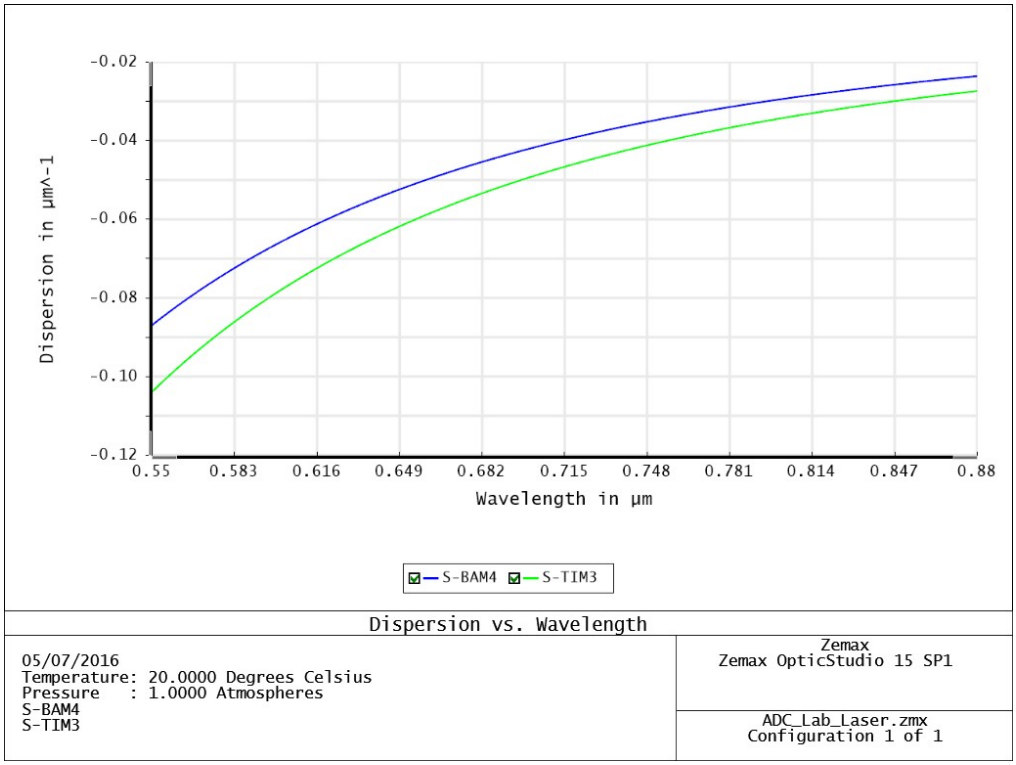

Figure 4.4: Prisms material Dispersion vs. Wavelength.

with a 46 mm clear central aperture and 10 mm central thickness. The diameter of the clear aperture was determined by the size of beam coming from CANARY, and the final diameter was set to fit the prisms inside standard CotS 50 mm lens tubes. The wedge angles for the prisms were optimised to satisfy the requirements of dispersion power and pupil stability, obtaining 5.608° and 5.416° as wedge angles. Since the wedges of the prisms are different, one of the external faces of the plate will not be perpendicular to the optical axis. The External faces of the plates, in blue (S-BAM4), in Figure 4.3 are at right angle with respect to the optical

axis, which is why the inner faces in green (S-TIM3) will have a slight inclination with respect to the plane perpendicular to the optical axis. The design was carried-out using Zemax Optics Studio. The parameters used in the design are summarised in Table 4.2. The model was optimised to obtain minimum dispersion between 550 nm and 880 nm at different zenith angles up to 60°. Figure 4.5 shows the simulated corrected PSFs when applying the ADC to the atmospheric dispersion conditions presented in Figure 4.2, the improvement of the PSF when the ADC is active is evident. Considering that CHOUGH aims to investigate PSF correction with Strehl ratios equal to or greater than 0.5 in the visible (R-band), the ADC design parameters are adequate to satisfy CHOUGH requirements.

Table 4.2: Prism specifications for one plate.

	Prism 1	**Prism 2**
Diameter	50.0 ± 0.1 mm (C/A 46 mm)	50.0 ± 0.1 mm (C/A 46 mm)
Material	S-BAM4	S-TIM3
Center Thickness	10.0 ± 0.1 mm	10.0 ± 0.1 mm
Wedge on one face(right)	5° 36' 30" ± 0° 1'	5° 32' 30" ± 0° 1'

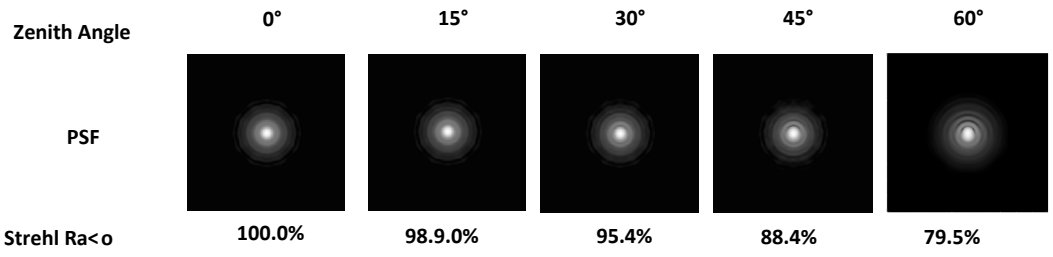

Figure 4.5: Simulation of corrected PSF applying the ADC.

The Prisms were manufactured by Gooch and Housego Optics through United Kingdom Astronomy Technology Centre (UKATC), to whom the design was handed over to handle the procurement of the prisms. Figure 4.6, 4.7, 4.8 show the mechanical drawings of the prisms made by UKATC.

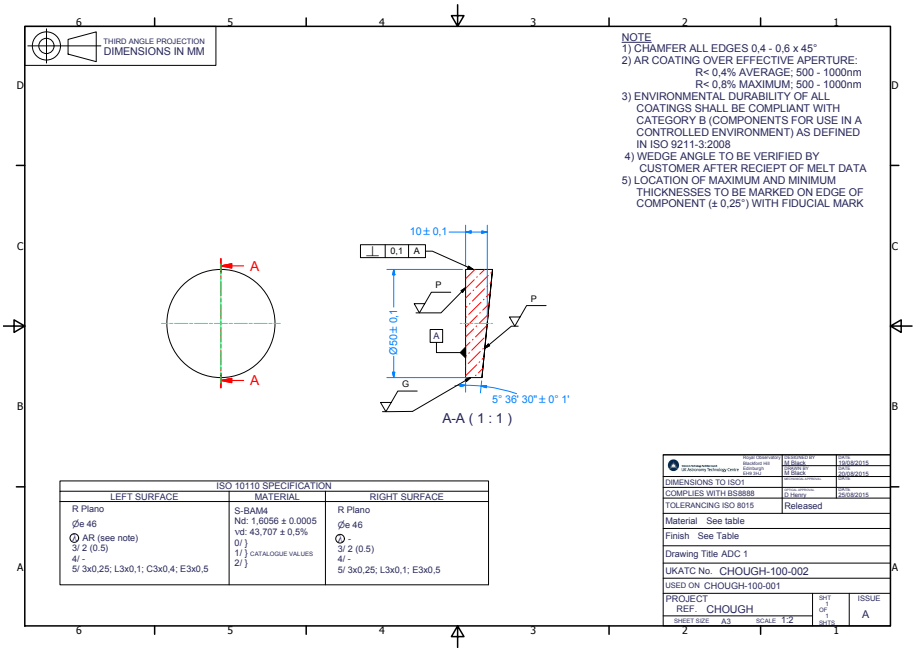

Figure 4.6: S-BAM4 prism. (Image credits: UKATC).

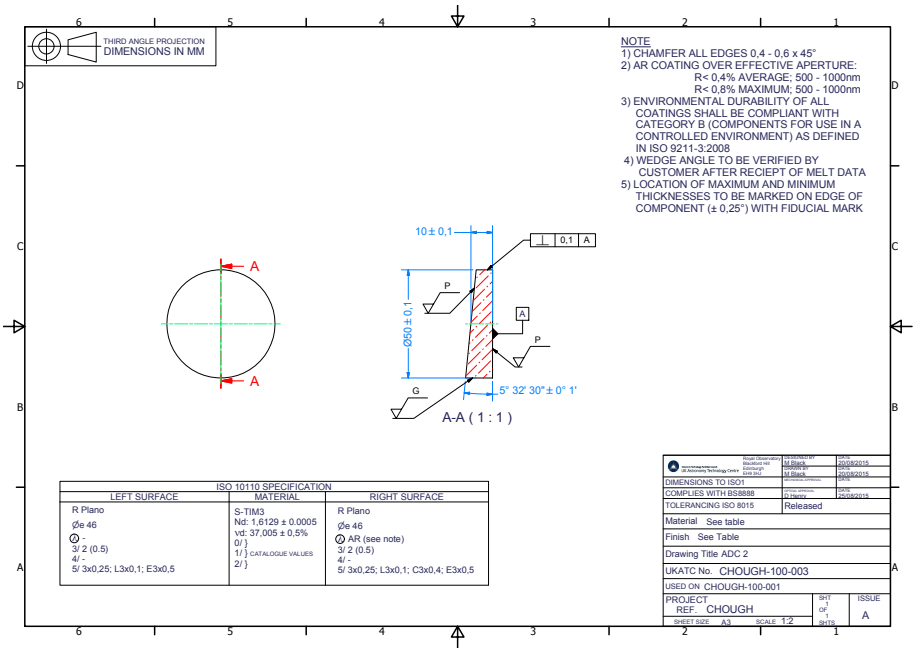

Figure 4.7: S-TIM3 prism. (Image credits: UKATC).

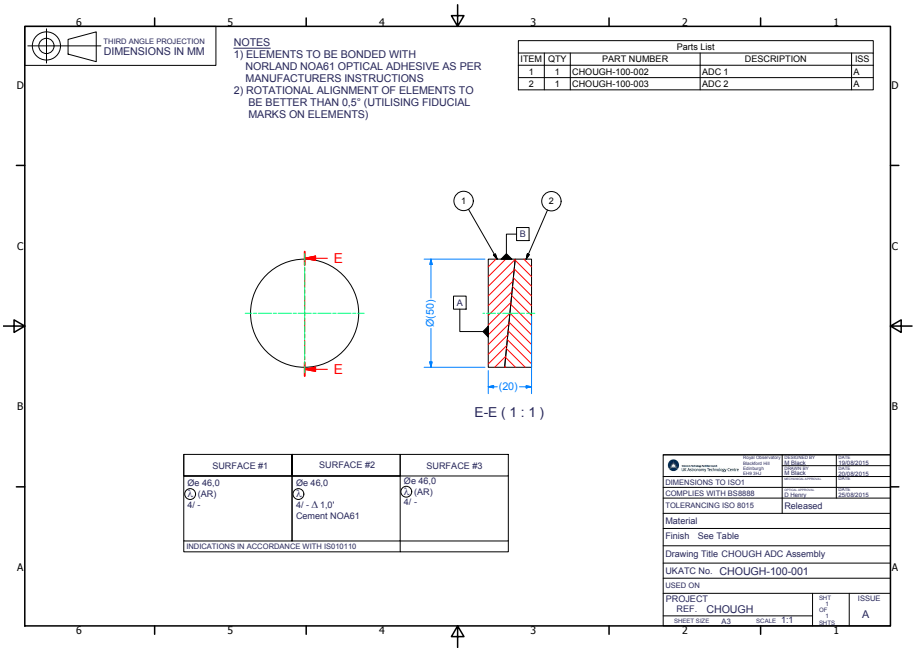

Figure 4.8: S-BAM4/S-TIM3 Assembly. (Image credits: UKATC).

Figure 4.9 shows pictures of the prisms in the laboratory. The prisms were mounted in 50 mm lens tubes as shown on the right-hand side picture in Figure 4.9.

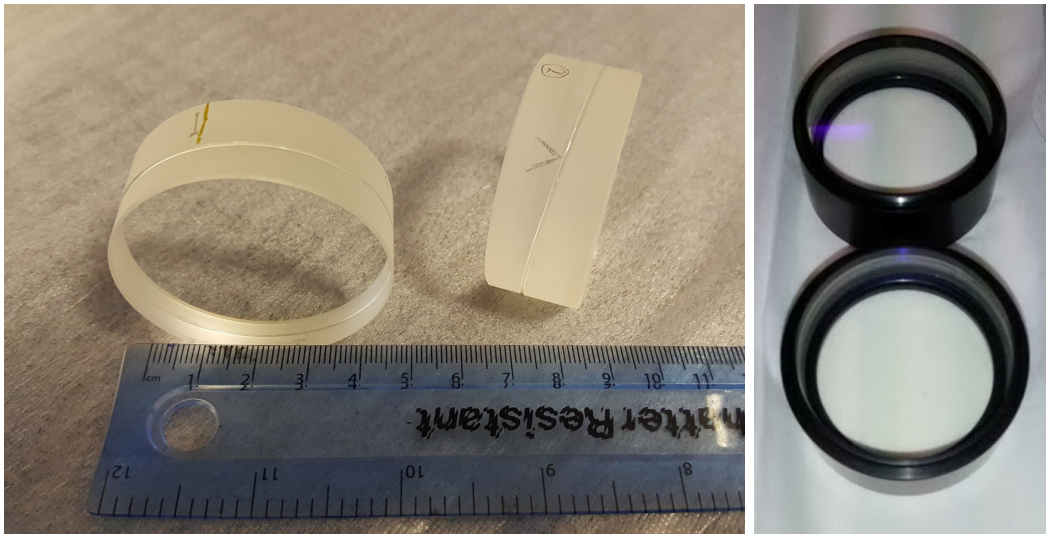

Figure 4.9: ADC Prisms in the laboratory.

4.3 Rotation Stages

The Rotation stages are CotS produced by Thorlabs, model NR360S rotation stages. They can provide arcsecond resolution when driven from a micro-stepping stepper motor controller. The aperture through the centre of the rotation stages features an SM2 thread on the rotating and the non-rotating parts, making the stage compatible with SM2 lens tubes used for holding the prisms (Figure 4.9). The motor controller board is a RUMBA working together with a stepper driver DRV8825.

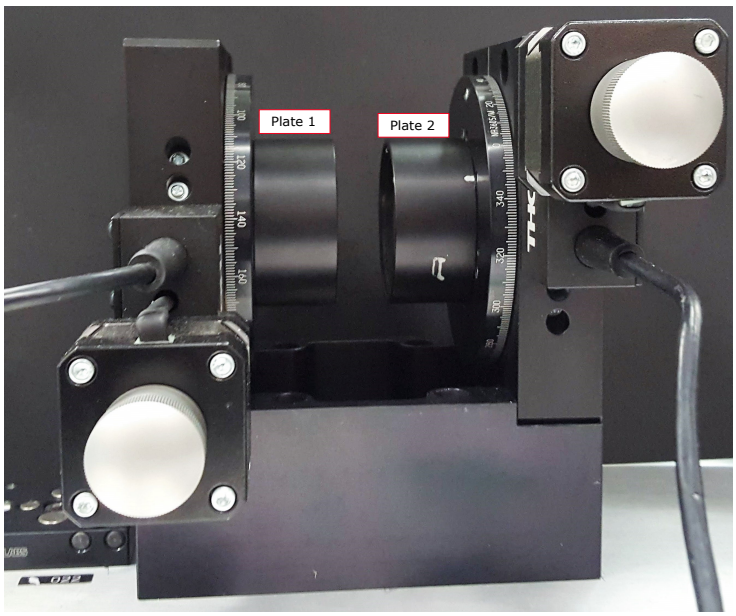

Figure 4.10: Rotator Stages.

4.4 ADC characterisation and dispersion experiments at CfAI laboratories

In this section, the experiments carried out on the ADC at CfAI laboratories are described. These experiments include; characterisation of the prisms and ADC dispersion power.

4.4.1 Light Source

The ADC is illuminated through a light source consisting of a set of different wavelength LEDs (605 nm, 630 nm, 660 nm, 680 nm, 710 nm), each one of them connected to an optical fibre shown in Figure 4.11. These fibres go into a bundle butt-coupled to a 0.5 NA multimode fibre (Figure 4.11) that subsequently goes into a collimating system.

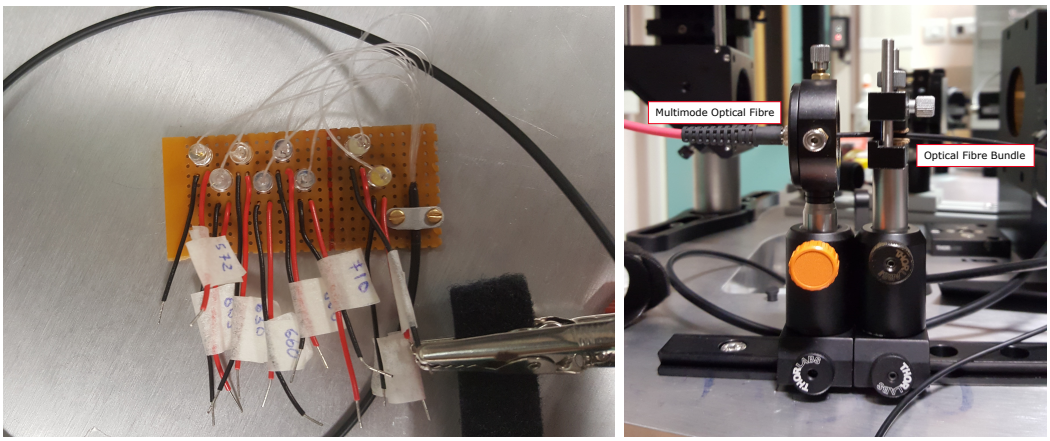

Figure 4.11: LEDs (left) and Butt-coupling of the fibres (right).

4.4.2 Identification of prisms' materials

The prisms received from the manufacturer did not have any reference for which side of the plate was S-TIM3 or S-BAM4. This was a problem since they look identical. To determine which one was which, each plate was placed into its holding cell and illuminated independently with a collimated beam. After going through the prisms the beam is focused by a convergent lens onto a camera as in the set-up presented in Figure 4.12.

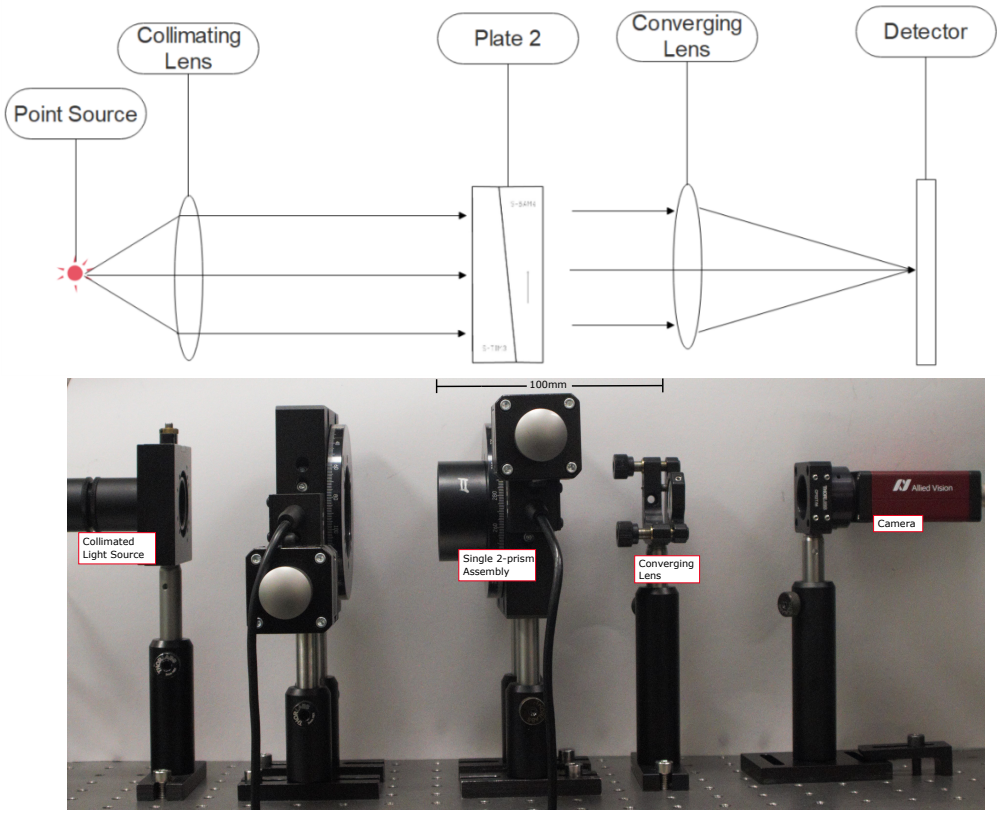

Figure 4.12: ADC experiment set-up.

The simulation shows that when the light goes through material S-TIM3 first and then S-BAM4 the effect of dispersion is higher than vice-versa. Therefore, for a monochromatic beam the orientation of the plate that produces a bigger displacement of the PSF position corresponds to the configuration S-TIM3/S-BAM4.

Figure 4.13 shows the PSF displacement vectors when testing the plate for the two different combinations. The blue vector with bigger magnitude corresponds to the S-TIM3/S-BAM4. Once the material of each side of the plates was identified the prisms were marked for reference.

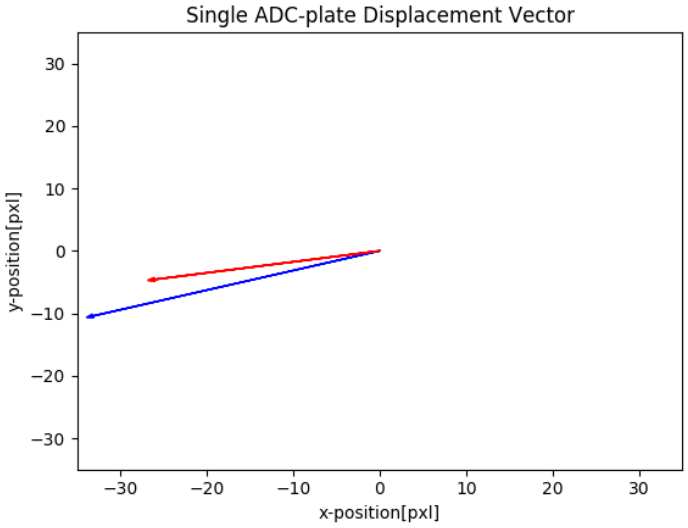

Figure 4.13: The blue arrow represents the dispersion due to the S-TIM3/S-BAM4 combination. The red arrow is the dispersion due to the S-BAM/S-TIM3 combination.

4.4.3 Finding the Zero: Fiducial marks, bases and apices of the prisms

The prisms received from the manufacturer came with fiducial marks indicating where the wedges are thickest and thinnest. The marks were made on the blanks when they were aligned on the polishing plate by polishing a small area on the fine ground perimeter. The fiducial marks were indistinct and difficult to identify. The plates had to be carefully put inside the holding cells keeping in mind the position of the fiducial marks which were to be covered by the lens tubes (Figure 4.10). It was important to align these fiducial marks to the the zero dispersion axis as shown in the Zemax model in Figure 4.14. It is from this zero dispersion axis that the

plates are counter-rotated increasing the dispersion power to compensate for the atmospheric dispersion. In theory, if the displacement of the PSF measured with respect to the centroid of the PSF when no prisms are present, measured with one plate and then the other independently at zero dispersion angle, the two resulting PSF displacement vectors should cancel each other out. Using the same set-up as in Figure 4.12 the plates were put one at a time in the second rotating stage and rotated until reaching the position where the PSF displacement vectors would have opposite directions as shown in Figure 4.15. This position is marked and these rotation angles are considered the zero (null) dispersion position.

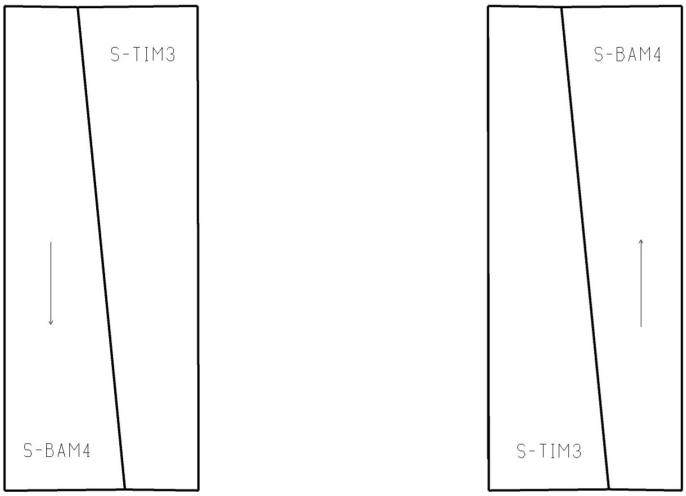

Figure 4.14: ADC Zero Dispersion Configuration. The arrows indicate the S-BAM4 base (S-TIM3 apex) direction.

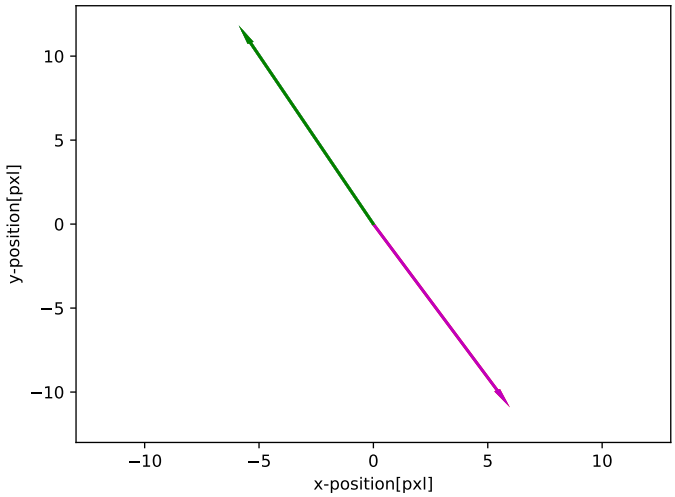

Figure 4.15: ADC Null Position Vectors.

4.4.4 Dispersion Experiments

To test the dispersion capabilities of the ADC, it was placed in front of the LED source and counter-rotated in steps of 30° (15° each plate in opposite directions), Figure 4.17. This is done for each of the LEDs. As a consequence of the ADC counter-rotation the PSF on the camera was expected to change its position at different rotation angles; and this change in position was expected to be different in magnitude for every wavelength too. Thus, there is a displacement ratio between different wavelength PSFs at different rotation angles, and the scaling of this ratio is controlled by rotating the plates. Figure 4.16 illustrates the method described above. Three wavelengths were used at two different rotation angles, 45° and 90°. The white disk represents the location of the zero dispersion when the ADC is at null dispersion, the coloured disks are the PSFs at 630 nm, 660 nm and 710 nm. The PSF displacement from the zero for each wavelength are measured, and then compared (ratio) for different rotation angles. This ratio should match the ratio obtained with Zemax.

The displacements obtained in the laboratory are measured calculating the im-

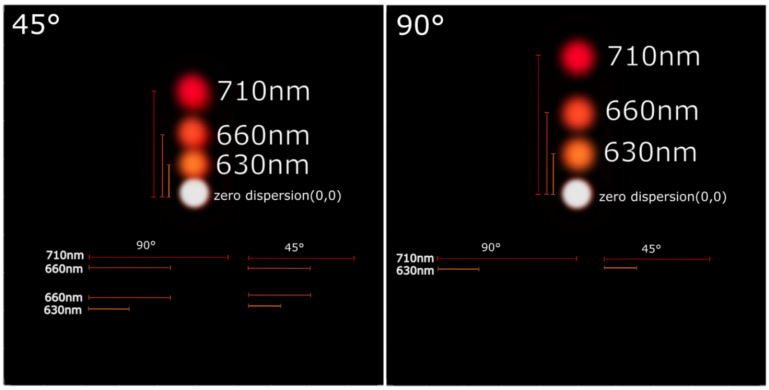

Figure 4.16: An illustration of the method employed to test the ADC dispersion.

age's centroid position with respect to the centroid position when the ADC is in its zero dispersion form. The centroiding error was under the minimum measurement unit, being < 1 pixel. Figure 4.17 shows the set-up for the experiment, where both plates are mounted on the rotating stages.

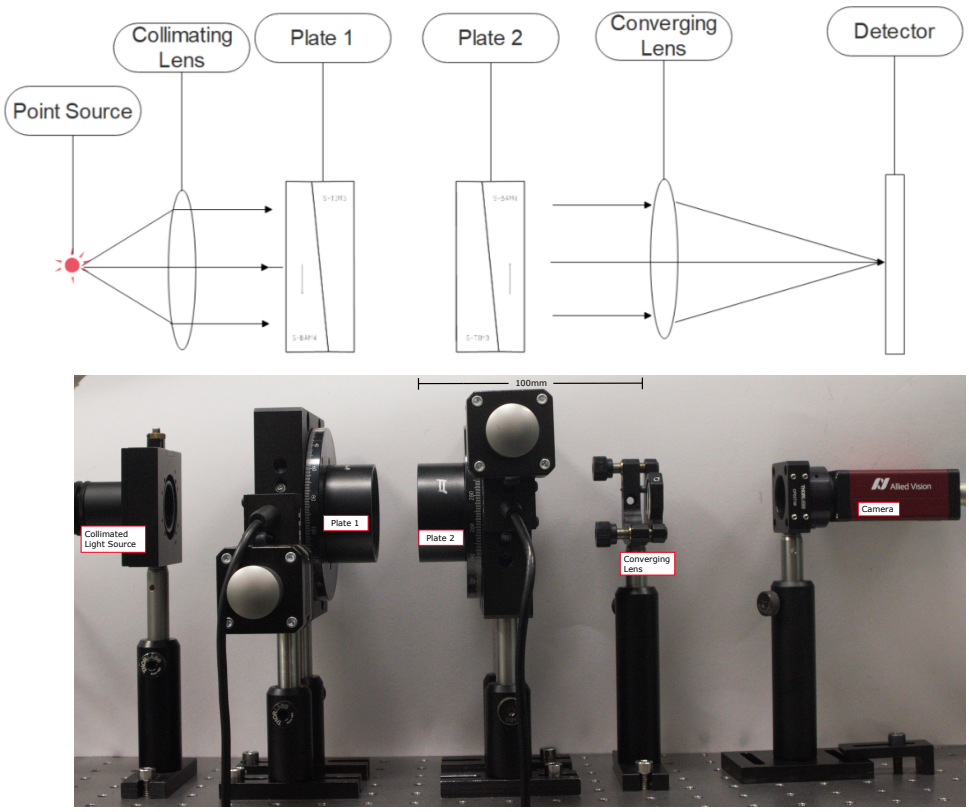

Figure 4.17: ADC Dispersion experiment set-up.

Tables 4.3, 4.4, 4.5, 4.6 show the displacement ratios by wavelength at different rotation angles. The green-white columns are the ratios between wavelengths at different ADC rotation angles in the laboratory and in simulation. The right column next is the comparison (ratio) between the laboratory results and the simulated data.

Table 4.3: 710 nm dispersion ratios. Laboratory/Zemax ratio average = 0.987, Standard Deviation = 0.018.

710 nm : 680 nm		**Lab/Zemax ratio**	**710 nm : 660 nm**		**lab/Zemax ratio**
15° Laboratory	1.036	**1.002**	15° Laboratory	1.057	**0.997**
15° Zemax	1.033		15° Zemax	1.060	
30° Laboratory	1.029	**0.995**	30° laboratory	1.056	**0.996**
30° Zemax	1.033		30° Zemax	1.060	
45° Laboratory	1.027	**0.994**	45° Laboratory	1.061	**1.001**
45° Zemax	1.033		45° Zemax	1.060	
60° Laboratory	1.027	**0.994**	60° Laboratory	1.062	**1.002**
60° Zemax	1.033		60° Zemax	1.060	
75° Laboratory	1.031	**0.998**	75° Laboratory	1.069	**1.008**
75°° Zemax	1.033		75° Zemax	1.060	
90° Laboratory	1.036	**1.002**	90° Laboratory	1.072	**1.012**
90° Zemax	1.033		90° Zemax	1.060	
710 nm : 630 nm		**Lab/Zemax ratio**	**710 nm : 605 nm**		**Lab/Zemax ratio**
15° Laboratory	1.077	**0.972**	15° Laboratory	1.105	**0.952**
15° Zemax	1.109		15° Zemax	1.160	
30° Laboratory	1.077	**0.972**	30° Laboratory	1.101	**0.949**
30°° Zemax	1.109		30° Zemax	1.160	
45° Laboratory	1.083	**0.977**	45 Laboratory	1.111	**0.958**
45° Zemax	1.109		45 Zemax	1.160	
60° Laboratory	1.090	**0.983**	60° Laboratory	1.122	**0.967**
60°° Zemax	1.109		60° Zemax	1.160	
75° Laboratory	1.095	**0.988**	75° Laboratory	1.137	**0.980**
75° Zemax	1.109		75° Zemax	1.160	
90° Laboratory	1.107	**0.999**	90° Laboratory	1.144	**0.986**
90° Zemax	1.109		90° Zemax	1.160	

Table 4.4: 680 nm dispersion ratios. Laboratory/Zemax average = 0.993, Standard Deviation = 0.020.

680 nm : 660 nm		**Lab/Zemax ratio**	**680 nm : 630 nm**		**Lab/Zemax ratio**
15° Laboratory	1.020	**0.995**	15° Laboratory	1.040	**0.970**
15° Zemax	1.026		15° Zemax	1.073	
30° Laboratory	1.027	**1.001**	30° Laboratory	1.047	**0.976**
30° Zemax	1.026		30° Zemax	1.073	
45 Laboratory	1.034	**1.008**	45° Laboratory	1.055	**0.983**
45 Zemax	1.026		45° Zemax	1.073	
60° Laboratory	1.035	**1.009**	60° Laboratory	1.062	**0.989**
60° Zemax	1.026		60° Zemax	1.073	
75 Laboratory	1.036	**1.010**	75° Laboratory	1.062	**0.990**
75 Zemax	1.026		75° Zemax	1.073	
90° Laboratory	1.035	**1.009**	90° Laboratory	1.069	**0.997**
90° Zemax	1.026		90° Zemax	1.073	

680 nm : 605 nm		**Lab/Zemax ratio**
15° Laboratory	1.067	**0.950**
15° Zemax	1.123	
30° Laboratory	1.070	**0.953**
30° Zemax	1.123	
45° Laboratory	1.082	**0.964**
45° Zemax	1.123	
60° Laboratory	1.093	**0.973**
60° Zemax	1.123	
75° Laboratory	1.102	**0.982**
75° Zemax	1.123	
90° Laboratory	1.105	**0.984**
90° Zemax	1.123	

Table 4.5: 660 nm dispersion ratios. Laboratory/Zemax average = 0.971, Standard Deviation = 0.011.

660 nm : 630 nm		**Lab/Zemax ratio**	**660 nm : 605 nm**		**Lab/Zemax ratio**
15° Laboratory	1.019	**0.975**	15° Laboratory	1.045	**0.955**
15° Zemax	1.046		15° Zemax	1.095	
30° Laboratory	1.020	**0.976**	30°Laboratory	1.042	**0.952**
30° Zemax	1.046		30° Zemax	1.095	
45° Laboratory	1.020	**0.975**	45° Laboratory	1.047	**0.956**
45° Zemax	1.046		45° Zemax	1.095	
60° Laboratory	1.026	**0.981**	60° Laboratory	1.056	**0.965**
60° Zemax	1.046		60° Zemax	1.095	
75° Laboratory	1.025	**0.980**	75° Laboratory	1.064	**0.972**
75° Zemax	1.046		75° Zemax	1.095	
90° Laboratory	1.033	**0.987**	90° Laboratory	1.067	**0.975**
90° Zemax	1.046		90° Zemax	1.095	

Table 4.6: 630 nm dispersion ratios. Laboratory/Zemax average = 0.983, Standard Deviation = 0.006.

630 nm : 605 nm		**Lab/Zemax ratio**
15° Laboratory	1.025	**0.980**
15° Zemax	1.047	
30° Laboratory	1.022	**0.976**
30° Zemax	1.047	
45 Laboratory	1.026	**0.980**
45 Zemax	1.047	
60° Laboratory	1.030	**0.984**
60° Zemax	1.047	
75 Laboratory	1.038	**0.992**
75 Zemax	1.047	
90° Laboratory	1.033	**0.987**
90° Zemax	1.047	

The average and standard deviation of the laboratory/simulation ratio are noted above each table. The results are shown to be precise, and to confirm that the discrepancy between the expected dispersion simulated with Zemax and the actual dispersion obtained in the laboratory will not affect the performance of the ADC, the dispersion in the laboratory was introduced in the Zemax model changing the rotation angles in order to get the same dispersion numbers obtained in the laboratory. For this purpose, the 710 nm and 605 nm PSF relative displacement with respect to the null position of the ADC used to produce the ratios are utilised, the longest and shortest wavelengths in the laboratory experiment, thus the highest dispersion difference. The result obtained in Zemax applying these numbers to the atmospheric dispersion at 60° of zenith angle are presented in Figure 4.18. The image on the left shows the PSF of the original simulation, the image on the right shows the PSF with the prisms rotated 8.4° from the maximum dispersion rotation angle, equivalent to what was obtained in the laboratory. The reduction in the Strehl ratio is 4.4 % for the worst case, wavelength range from 510 nm to 880 nm, at 60° of zenith angle.

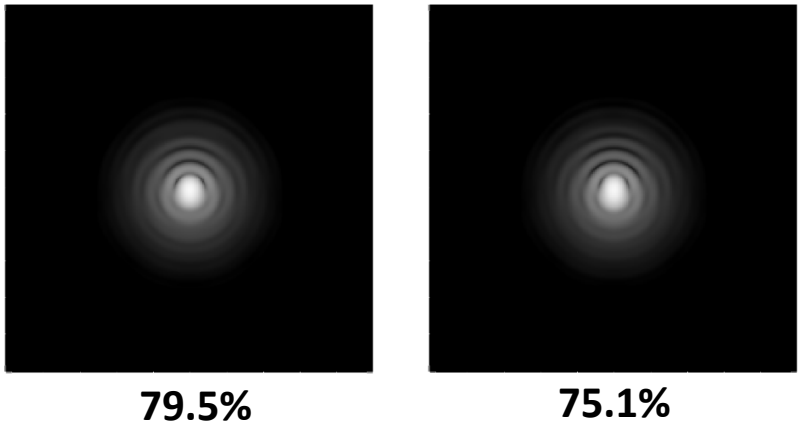

Figure 4.18: Left: original Zemax, right: prisms rotated 8.4° from the maximum dispersion.

4.5 Pupil Shift Experiment

The ADC design requires the pupil shift to be kept to a minimum in order to avoid actuator-subaperture mismatch, as explained in Section 4.1. The pupil shift should be restricted to $< 0.3\,\%$, which is equivalent to $6.696\,\mu$m. To verify the ADC works under the pupil shift requirements specified in the design, in the laboratory, the ADC was rotated as it would do on-sky and one measured the pupil centroids in order to obtain its displacement from when the ADC is at null-dispersion.

The centroid of the pupil was measured so it was important to have a good illumination along it, in order to, calculate the centroids correctly. The experiment is run within CHOUGH, hence the light goes all the way up to the HOWFS camera where the pupil was imaged. To obtain a more defined pupil shape the MLA was removed from the Shack-Hartmann, and the light source changed for a white LED connected to the multimode fibre illuminating CHOUGH. This white source illuminates the pupil more uniformly than the LED set used for prior tests, it has better coupling and it does not need to go through the fibre bundle.

The box enclosing the white LED is shown on the right-hand side of Figure 4.19, and the tip of the 0.5 NA multimode fibre used to illuminate experiment on the

left. The LED is used with a pulse-width modulation (PWM) controller. Single-band bandpass filters available in the laboratory at the time of the experiment were used; 469 nm, 530 nm and 640 nm. An image of the pupil at the HOWFS camera is shown Figure 4.20.

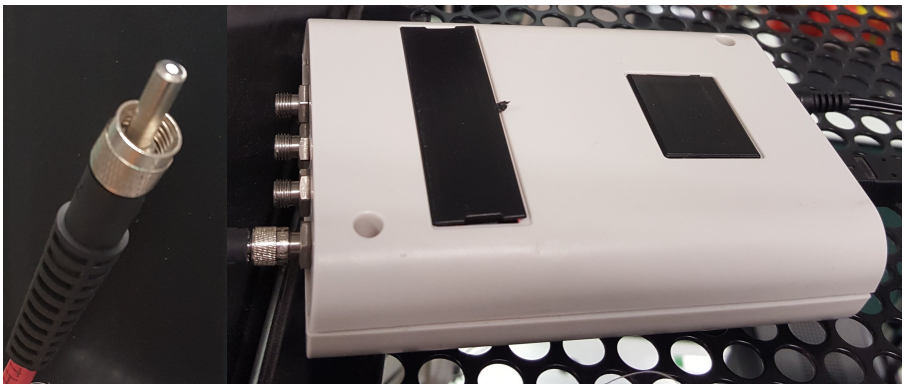

Figure 4.19: Left-hand side: tip of the 0.5 NA multimode optical fibre. Right-hand side: box enclosing the white LED.

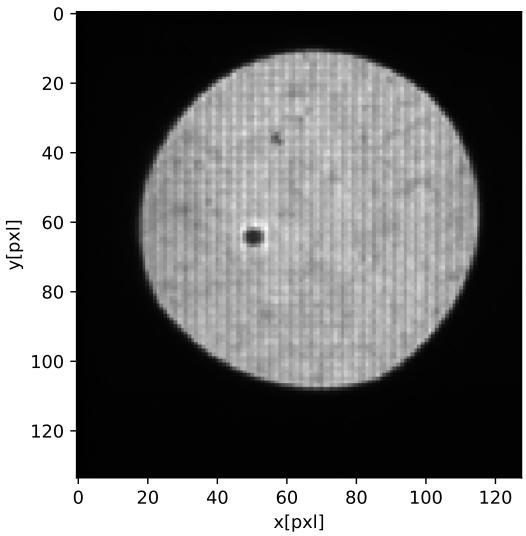

Figure 4.20: Pupil image at HOWFS camera.

4.5.1 Camera Translation test

The goal of this section is to verify that the centroid displacement measurements on the Shack-Hartmann camera are accurate, in order to measure the pupil shift produced by the ADC. The DM was conjugated to the HOWFS camera in order to image the pupil. The Nüvü is mounted on x and y translation stages as described in Section 3.2.3.3 (Figure 3.14 and 3.15). Utilizing the micrometers of these stages, the camera was translated by certain amounts, and images of the pupil were recorded. The centroid for these 2D-array pupils were measured as "centre of mass" determined from image moments. It is expected the centroid of the images move on the same axis as the translation stage, and in the same amount indicated by the micrometers. The centroid was measured over ten images at each position of the translation stage, the random error being negligible ($\ll 1\,\mu$m). The standard deviation of the difference between the centroid shifts and the stage micrometres are in the second and third columns of Tables 4.7 and 4.8. The square root of the sum of squares of these values are in Table 4.9. These errors are considered in the next two experiments.

Table 4.7: x-axis error due to the difference between the centroid shift and the stage micrometre measurements.

Filter [nm]	**x [μm]**	**y [μm]**
469	1.30	1.06
530	0.48	0.29
640	1.17	1.78

Table 4.8: y-axis error due to the difference between the centroid shift and the stage micrometre measurements.

Filter [nm]	**x [μm]**	**y [μm]**
469	0.11	0.73
530	0.16	0.86
640	0.47	2.96

Table 4.9: Total x- and y-error. The square root of the sum of squares of error in Tables 4.7 ans 4.8.

Filter [nm]	**x [μm]**	**y [μm]**
469	1.30	1.29
530	0.51	0.91
640	1.26	3.45

4.5.2 Pupil Shift Experiment & Results

The ADC is set to its null-dispersion configuration as shown in the layout in Figure 4.14. An image is taken and its centroid is calculated and saved, acting as a reference point. Thenceforth the ADC is rotated in steps of 15° up to 90° each plate which is its maximum dispersion form. Figure 4.21 presents the results in the three wavelengths implemented for this experiment. The x-axis is the rotation angle at which each plate of the ADC is when counter-rotated, the y-axis is the pupil shift in microns for each of the ADC rotations. The black dashed line at the top part of the graph determines the maximum acceptable pupil shift according the design requirements. Therefore, from the plots it is possible to confirm the ADC pupil shift is inside the acceptable length of displacement.

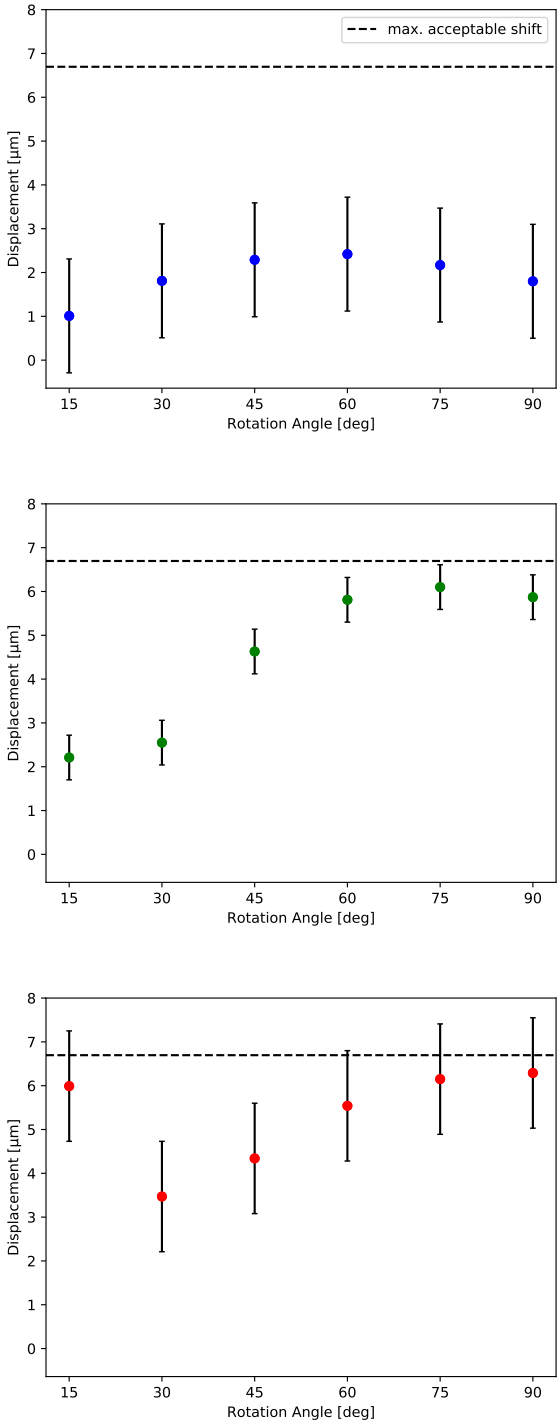

Figure 4.21: Pupil shift test results at three different wavelength (469 nm, 530 nm and 640 nm). Shifts measured at six rotation angles (15°, 30°, 45°, 60°, 75°, and 90°). The dashed black line represents the maximum acceptable pupil shift.

4.6 Plate Wedge Angle Test

Using the set-up described in the previous section it is possible to verify if the wedge angles of the ADC prisms satisfy the prescribed model. The method consists in using one plate of the ADC at a time, the plate is rotated in 30-degree steps from 0° to 330°. The centroid of the pupil should trace a circle as the plate rotates, and the radius of the circle should match the one generated with the Zemax model within tolerance range.

Red markers in Figure 4.22 show the individual plates' centroid positions at different rotation angles. A circle fitting these points is drawn as a continuous black line. The dashed cyan line is the circle traced by the plates in the Zemax simulation using the ideal wedge angle of the plates. The dash magenta is the circle traced by the Zemax simulation for when the wedge angle is modified by 1' which is the tolerance specified for manufacturing.

The centroids in Figure 4.22 do not delineate a "perfect" circle as expected. There is nothing that leads one to think it is due to something in the optics of the experiment, or a misalignment in the system, thus it was thought it could be caused by the centroiding. Then in an attempt to improve the centroiding and the shape of circle traced by the image on the camera produced by the ADC plates, different thresholds in image and Fourier space were applied as well as a correlation method for centroiding, additionally a mask on the pupil was implemented. Nevertheless the accuracy on the shape of the circles traced did not improve.

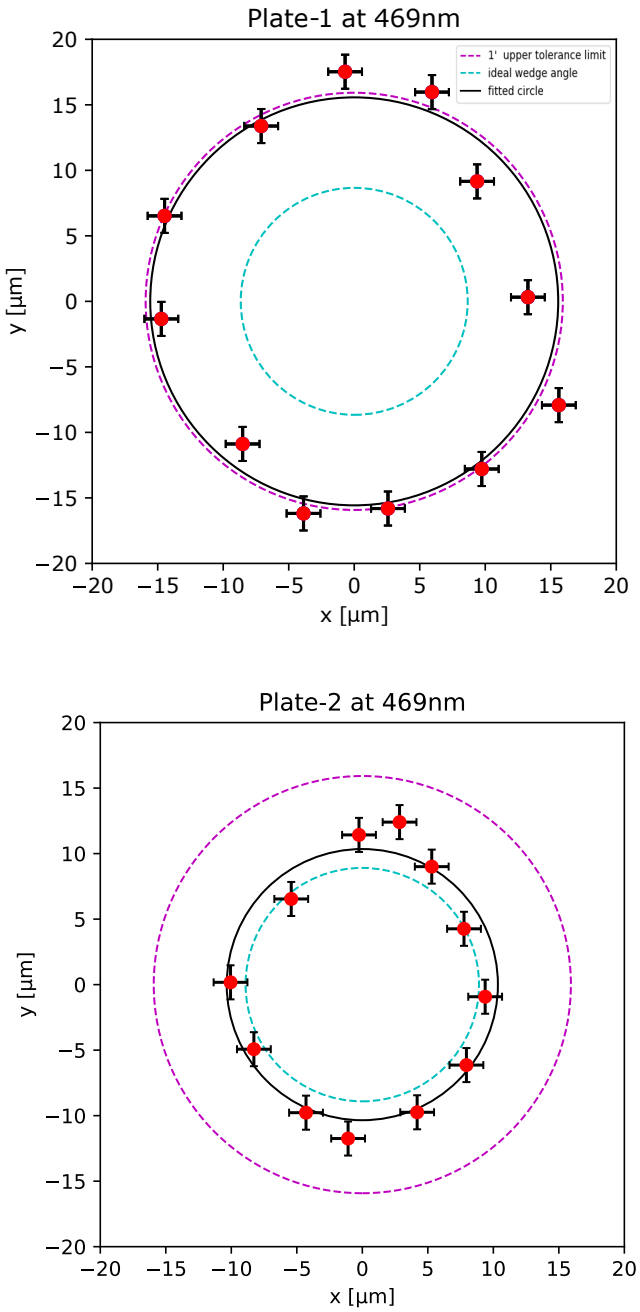

Figure 4.22: Measured circular motion of the pupil due to rotation of individual ADC plates. Red markers are the centroid position of the pupil. The black solid line is a circle fitted to the centroids. The dashed cyan line is the circle traced by the plates in the Zemax simulation using the ideal wedge angle of the plates. The dash magenta is the circle traced by the Zemax simulation for when the wedge angle is modified by 1' which is the tolerance specified for manufacturing.

The Nüvü camera could not be removed from the WFS for characterization so unable to flat-field, in order to remove possible artifacts from the image, sensitivity variances between pixels in the detector, or illumination variations within the optical system. This could be a potential explanation for the "not-perfect" circle results. However, considering the fitted circle to the data and according to what is presented in Figure 4.22, the wedge angles of the prisms are inside the tolerance range recommended.

4.7 Conclusions

The design of the ADC was described in this chapter as well as the motivation to implement it in CHOUGH. This AO system works in a wide rage of the visible spectrum where the effects of atmospheric dispersion are very noticeable, which makes essential the implementation of an ADC in the AO system when on-sky.

The simulated results as well as laboratory tests were presented here. The Zemax simulation and dispersion measured in the laboratory indicate that in the most challenging scenario, when the telescope points at at 60° of zenith angle, and a wavelength range between 510 nm and 880 nm, there would be a reduction in the expected Sthrel ratio. This would be a 4 % for maximum chromatic dispersion that could be encounter on-sky. At zenith angles $< 60°$ when this difference is $< 4\,\%$, it can be compensated rotating the ADC a few extra degrees to give the bit of extra dispersion power needed. The degradation of the PSF compared to the design is small not affecting considerably the image quality (Figure 4.18).

The pupil shift (section 4.5.2) is kept under 6.696 μm, specified in CHOUGH design as the maximum acceptable pupil displacement on the HOWFS.

In conclusion, the results presented in this chapter show that the manufactured ADC has the capability to correct for the chromatic atmospheric dispersion that could be found on-sky, as well as, meeting the required pupil stability on the HOWFS and HODM.

Chapter 5

SNR, Target selection, On-sky and Laboratory implementation

To assess the on-sky performance of an AO system and to test the capabilities of the instrument, it is important to find suitable astronomical targets. When choosing astronomical targets it is important to consider the number of photons reaching the WFS; they need to be sufficient so that the system keeps stable. This brings up a question: what is the limiting target brightness CHOUGH could see? In order to answer this question, it is necessary to know the transmittance of the AO system, the number of photons collected per subaperture, and the SNR.

The engineering target selection described in this chapter were proposed for the two nights on-sky run during October 2016 at the WHT in La Palma, Canary Islands, Spain. Sections 5.4.1 and 5.5 describe the on-sky run and current laboratory experiments.

5.1 CHOUGH Transmittance

The fraction of incident light that is transmitted throughout the system WHT-CANARY-CHOUGH can be determined by the number of reflective and refractive surfaces the light interacts with in the system, this together with the Quantum

Efficiency (QE) of the camera gives the approximate total transmittance of light through the system WHT-CANARY-CHOUGH. The reflectivity and transmission of the surfaces involved in the optical path are listed in Table 5.1. For more details on CHOUGH optical components see appendix 7.2

Table 5.1: Throughput.

WHT	**R/T**
3 Al mirrors	0.75
1 Derotator(1 window+3 Al mirrors)	0.87
1 Field lens	0.90
Throughput	**0.60**

CANARY	**R/T**
6 Ag mirrors	0.94
1 Al mirror	0.92
Dichroic	0.90
LODM	0.99
Throughput	**0.77**

CHOUGH	**R/T**
5 Ag mirrors	0.95
3 Al mirrors	0.77
2 ADC plates	0.98
kilo-DM	0.86
Dichroic	0.98
HOWFS	0.77
Fold mirror	0.99
HNü 128 protective Window	0.94
Throughput	**0.43**

The transmittance T is expressed by Equation 5.1, where T_n is the transmittance of the components in the optical path, and QE is the quantum efficiency. QE for the Nüvü camera in EMCCD mode is equivalent to 0.45 for SNR calculations.

$$T = \prod_{1}^{n} T_n \times QE. \tag{5.1}$$

Using the numbers in Table 5.1 and Equation 5.1 the transmittance for the combined system WHT-CANRY-CHOUGH is

$$T = 0.60 \times 0.77 \times 0.43 \times 0.45 = 0.09.$$

The amount of the light transmitted through the WHT-CANARY-CHOUGH system is 9 %. This result was calculated assuming that most optics have brand new coatings. However, many of the components might have degraded over time and the transmittance will be below this estimate.

5.2 Photons per subaperture

The WHT primary mirror is sampled by 31×31 subapertures, Figure 5.1. The diameter D of the primary mirror is 4.2 m.

Consequently one side of a subaperure is the fraction of the mirror diameter over the number of subapertures along it, n_{sub},

$$A_{sub} = \frac{D}{n_{sub}} = \frac{4.2\,m}{31},$$

therefore the area of one subaperture, A_{sub}, at the primary mirror of the telescope is

$$A_{sub} = 1.35\,m \times 1.35\,m = 0.018\,m^2.$$

From the magnitude of a star it is possible to obtain the flux, F. So then the number of photons per subaperture per frame is given by

$$n_p = F\left[\frac{photons}{m^2 \times s}\right] \times A_{sub}\left[m^2\right] \times T \times \frac{1}{\nu}\left[s\right]. \tag{5.2}$$

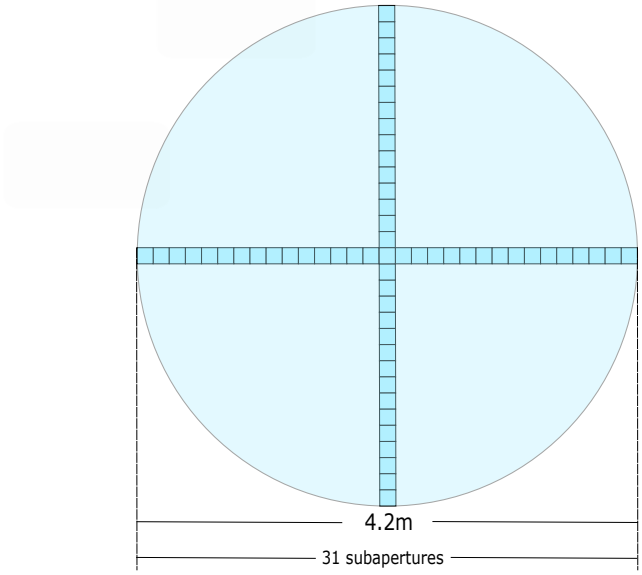

Figure 5.1: WHT primary mirror sampling (along x and y axes).

where F is the photon flux from the object, A_{sub} is the area of one subaperture, T the transmittance of the system, and ν the frame frequency.

5.3 SNR

SNR describes the quality of a measurement. In CCD imaging, SNR compares the level of a desired signal to the level of background noise. Specifically, it is the ratio of the measured signal to the overall measured noise (frame-to-frame).

The EMCCD SNR is affected the same way halving the QE would, so the SNR can be treated as a common CCD and taking this into consideration. For a conventional CCD camera used for wavefront slope measurements, the SNR is (Robert K. Tyson, 2004)

$$\mathrm{SNR} = \frac{n_p}{\left(n_p + N_D\left[n_B^2 + \left(\frac{e_n}{G}\right)\right]\right)^{1/2}}.$$

where n_p is equal to the number of detected photons per subaperture; N_D is the number of pixels in a quad-cell subaperture; n_B is the background noise, which is very low, $\ll 0$; G equals the gain ($G = 1$); e_n is the read-noise in electrons per pixel < 0.1. Given that $n_p \gg N_D\left[n_B^2 + \left(\frac{e_n}{G}\right)\right]$ the SNR equation simplifies as

$$\mathrm{SNR} = \frac{n_p}{\sqrt{n_p}}.$$

Table 5.2 presents the SNR for different star magnitudes, the number of photons calculated using Equation 5.2, and the flux obtained from the star magnitude using a magnitude-to-flux converter code.

Table 5.2: m: Star Magnitude, Spectral Bands, ν: Frame Rate, Number of Photons (per subaperture), and SNR.

m	bands	ν [Hz]	Photons	SNR
5	V - R	1000	260.46	16.14
6	V - R	1000	103.69	10.18
7	V - R	1000	41.28	6.43
8	V - R	1000	16.43	4.05
9	V - R	1000	6.54	2.56
10	V - R	1000	2.60	1.61
11	V - R	1000	1.02	1.04

The transmittance used in the SNR calculations is considering brand new optical coating estimates, which suggests the SNR calculations listed above can be lower due to optics degraded over time. Thus, to successfully find useful test targets it is preferable to choose targets brighter than magnitude 8.

5.4 Target Selection

An interesting target to observe and test CHOUGH's AO capabilities would be double stars. In observational astronomy, a double star is a pair of stars that appear close to each other in the sky as seen from Earth when viewed through an optical telescope, if not viewed with adequate resolving power they look as one. The components of a double star are generally denoted by the letters A (for the brighter, primary, star) and B (for the fainter, secondary, star). In order to find a suitable double star for this propose the Washington Double Star (WDS) catalogue was used (WDS).

Given that the WHT theoretical resolution for a wavelength $\lambda = 700\,\mathrm{nm}$ and a primary mirror diameter $\mathrm{D} = 4.2\,\mathrm{m}$ is

$$1.22 \times \frac{\lambda}{D} = 1.22 \times \frac{700 \times 10^{-9}}{4.2} = 2.02 \times 10^{-7} rad.$$

$$= 0.0417".$$

A suitable target to test CHOUGH would be a double star with a separation $< 2.96"$, which is the isoplanatic angle at ORM (Garcia-Lorenzo and Fuensalida, 2011), the angle the two stars can be separated, and still have their light pass through the same turbulent region; and a separation greater than the theoretical diffraction limit of the telescope, 0.0417".

The targets were selected according to the following criteria: a) CHOUGH has the theoretical resolving power to resolve the target, b) the targets are bright enough to supply the WFS with sufficient photons, and c) the targets are visible at the time of the on-sky run. Table 5.3 presents a set of possible double stars targets to test CHOUGH.

Table 5.3: Targets. Presented in order are the WDS J2000 coordinates, the discovery and component designation, the first and last measured epoch, the number of means, the first and last measured position angle (theta) in degrees, the first and last measured separation (rho) in arcseconds, the magnitudes of the primary and secondary, the spectral type of one or both components (if known), proper motion in RA and Dec (primary and secondary in milliarcseconds/yr), the Durchmusterung (DM) number, and a notes column.

WDS	Discovr Comp	EPOCH		#	THETA		RHO		Magnitudes		Spectral	Prop Mot		2nd PM		DM	Desig	Note	Precise
Identifier		Frst	Lst		First	Last	First	Last	Pri	Sec	Type	RA”	DEC”	RA”	DEC”				Coordinate
00022+2705BU	733AB	1878	2014	188	274	339	0.7	0.4	5.83	8.9	G5Vb+K5V	+830	-989			+26	4734	NO	000210.18+270455.6
00046+4206CHR	122Aa,Ab	1986	1996	13	95	60	0.1	0.1	6.0	.	B9III	-009	-009			+41	4933	NO	000436.60+420533.2
00171+3841CHR	123	1986	1996	6	142	135	0.1	0.1	4.61	.	A2V	-048	-013			+37	34	NO	001705.54+384054.0
00209+1059BU	1093	1889	2012	106	54	117	0.4	0.8	6.73	8.55	A0V	-040	-029	-040	-029	+10	32	NO	002054.59+105836.8
00243+5201HU	506	1902	2007	40	217	94	0.2	0.1	5.95	6.84	B5IV	+017	-003			+51	62	NO	002415.64+520111.7
00257+0741OCC	228	1953	1953	0	-1	-1	0.1	0.1	8.0	8.0	K3III	+039	-045			+06	43		002541.89+074128.4
00282+4424LSC	7	2014	2014	2	239	237	0.1	0.1	5.3	7.7		+085	-015						002813.65+442340.0

5.4.1 On-sky implementation

The CHOUGH project was funded with two nights on-sky, 14–15 of October 2016. As described above, this is made possible via mating the bench to CANARY. This proved relatively straightforward and it is possible to enable the CANARY IR-camera by simply withdrawing the periscope as otherwise it is untouched by CHOUGH from a hardware perspective. From a software perspective, there is no (significant) reconfiguration required. A software operation issue is that to operate the CANARY bench facilities (principally calibration and the acquisition camera) the standard software is the Smart Tool in Yorick for CANARY (STYC) interface of CANARY. Due to lack of time to replicate the functionality of STYC, the concept of the Ledger was developed for CHOUGH. The Ledger contains a description of all bench changes under software control together with a time-stamp, and the changes are acquired by the Ledger via a Broker. A Broker is a software interface to the Ledger which can regularly poll existing software to monitor its state: STYC, for example, is wrapped by a Python Broker so that it can access the internal state of STYC. For CHOUGH-specific software, a Broker can be built-in and so interface with the Ledger immediately given a change of state. This methodology maintains a proper record of CHOUGH (plus CANARY) state changes and so allows for a manual reconstruction of total system state since given a common time-stamp. Then there is sufficient information for subsequent analyses of recorded data.

One failure on-sky was of NCPA compensation and a second of twin-DM control. For the former, access to CANARY was only possible at the telescope and the existing risk-reduction was insufficient: a Strehl ratio of 0.1 at 832 nm with on-bench sources was the best PSF produced. For twin-DM control, a failure to fully understand the CANARY software infrastructure meant the DM control was sub-optimal. Nonetheless, from a technical perspective, the installation into CANARY of CHOUGH was successful and only algorithmic issues are mandatory to resolve if another on-sky run is attempted (Bharmal et al., 2018).

Figure 5.2 shows a screen shot of CHOUGH's computer during the on-sky run. The camera 1 image in the top left corner of the Figure shows the HOWFS on a blue grid which represents the subapertures; the centroid vectors are in red. Another image of Camera 1 to the right shows the same wavefront sensor image but without the centroid vectors. The rtcActuatorBuf images on the top centre and left of the Figure show the commands being sent to the DM. rtcFluxBuf image displays the pixel values inside all defined and used subapertures. rtcPxlBuf window in the top right corner of the Figure shows the NFSI camera. The elongated bottom window shows a plot of the HOWFS centroids. rtcPxlBufSummed window on the bottom left of the figure is a 100-times averaged image of the wavefront sensor image displayed in rtcPxlBuf on the bottom right.

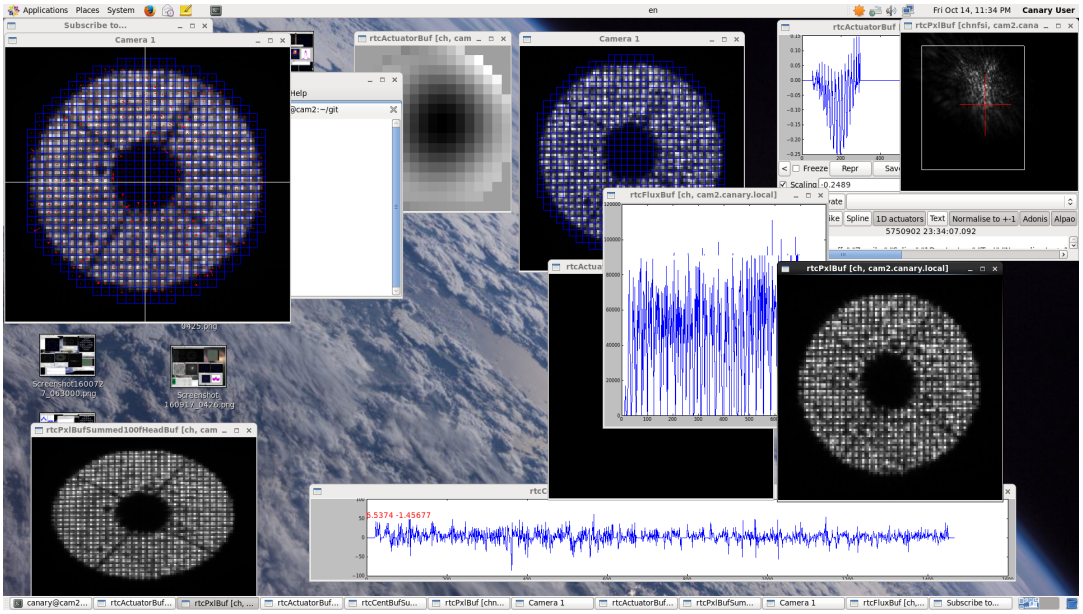

Figure 5.2: CHOUGH on-sky screen shot.

5.5 In-laboratory implementation

CHOUGH is now a laboratory-bound experiment. It is entirely possible to take it on-sky again subject to funding. The consequences are several-fold: first, the facilities provided by CANARY are replicated; second, the bench has been slightly upgraded; third, further software modifications are carried out. The primary CANARY facility replicated is an artificial source, called the Illuminator, mentioned in Chapter 2. A vertical unit that permits two standard fibre optic ferrules to be placed within the field of view of the NFSI: currently only one on-axis fibre is available. The secondary facilities which are not provided are a low-order high-stroke DM and a source of artificial aberrations. The former is planned via an upgrade of the Illuminator. Figure 5.3 presents NFSI PSF images obtained by Nicolas Dubost during his experiments with CHOUGH in the laboratory; with white light going through the whole optical path of CHOUGH, and NFSI filter number 4 (Table 2.1), 655 nm. The left-hand side image is the PSF and Strehl ratio when no DM corrections were applied to the system. The right-hand image is the PSF with DM corrections applied. This is being further optimized, and more recent experiments have achieved higher Strehl ratio, Figure 5.4 shows a PSF with 74 % Strehl ratio obtained in November 2018, using white light and filter 4. The code* used to compute the Strehl ratio was developed by Nicolas Dubost. It consists of finding the brightest pixel in the image, the PSF is centred in Fourier space, and then it is compared to a simulated image with Strehl = 1.

*https://github.com/nicolasdubost/strehl

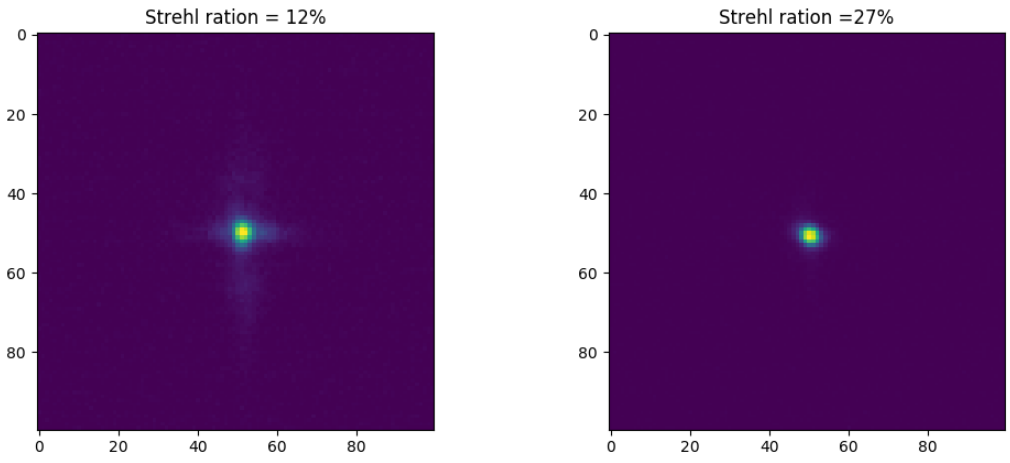

Figure 5.3: The image on the left is a PSF on the NFSI camera when no corrections were applied. The right-hand side image is the PSF with the DM corrections active. White light and Filter 4, $\lambda = 655\,\text{nm}$ (Image credits: Nicolas Dubost).

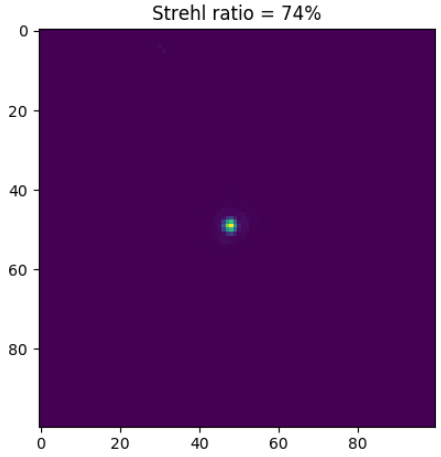

Figure 5.4: . PSF on the NFSI camera with DM corrections activated. White light and Filter 4, $\lambda = 655\,\text{nm}$ (Image credits: Nicolas Dubost).

5.6 Conclusions

The HOWFS determines the limiting brightness of the targets CHOUGH can do AO correction with. If the Shack-Hartmann does not receive enough photons the system can not measure the wavefront accurately due to the noise, then the AO system can not to close the loop. This chapter presents calculations for the number of photons the Shack-Hartmann could see according to the magnitude of the star and SNR, as well as, a possible astronomical targets to test the instrument's resolution power.

Eventually during the two nights run at the WHT, the system could not to close the loop as a result of other problems, thus CHOUGH did not use the targets presented in this chapter on this first run.

Chapter 6

Conclusions and Future Work

In conclusion, this thesis presented the development of CHOUGH, an experimental AO testbench dedicated to investigate high-order SCAO AO at visible wavelengths. In principle, it was designed to carry out experiments at the WHT, and it was aimed to support high-order AO research. Because its purposes differ from other visible wavelength AO projects, it was designed as a flexible platform.

In summary, CHOUGH as an addition to the CANARY project, sought to work as a narrow-field of view high-order SCAO for the WHT. CHOUGH was assembled at the WHT in La Palma, and had a two-night run. Since CHOUGH was first assembled at the telescope site, there was not enough time for laboratory testing, the non-common path aberration were not estimated and it was not possible to obtain high Strehl ratios on the bench by the time of the run.

After the on-sky run, back in the CfAI laboratories, CHOUGH was transformed into an on-axis high-order AO testbench instrument, this time without the CANARY tip-tilt mirror and DM. As a result, an on-bench illumination system nicknamed "Illuminator" (mentioned in Section 2.4) was added to the CHOUGH bench in the laboratory. In addtion, the CAWS (Dubost et al., 2018), a common-path interferometer to measure post-AO corrected light was implemented. Overall, the strong point of CHOUGH lies in the possibility to use it for both the laboratory experiments for AO research and the potential to go on-sky.

The main focus of this thesis was the development of a HOWFS and an ADC. Chapter 3 presented the HOWFS for CHOUGH, a 31×31 Shack-Hartmann WFS. The design and methods employed for system verification were discussed in the chapter. The WFS was tested in laboratory, and compared to its design and numerical model. Results confirmed the HOWFS works according to the specifications.

Chapter 4 described the ADC designed for CHOUGH. The ADC is made up of two plates of cemented double prisms. The design besides being able to correct for the atmospheric dispersion, contemplates a minimal pupil shift for DM-WFS pupil stability. The ADC went through a set of laboratory experiments, described in the chapter, to confirm it has the capability to correct for the chromatic atmospheric dispersion that could be found on-sky, as well as, meeting the required pupil stability on the HOWFS. In sum, the results confirm the ADC meets the design requirements.

Both of these designed sub-systems have performed individually within their specifications which demonstrates that the proposed design was successful.

In terms of future development of the CHOUGH project, funding has been secured to continue working on CHOUGH in the laboratory as a high-order SCAO bench experiment, and with the possibility to use it on-sky in association with CANARY. One of the future additions for CHOUGH is acquiring a second DM (LODM) which will enable CHOUGHs independence from CANARY. It is also planned to integrate the CAWS interferometer into the main control loop as an auxiliary high-order low speed WFS. Another possible development in CHOUGH is to add a Pyramid WFS to the existing Shack-Hartmann WFS. Finally, given the CANARY LGS capabilities, there is the potential to implement CHOUGH for LGS operation.

Chapter 7

Appendices

7.1 Sinusoidal wave pupil shift

The ADC was designed before the optical relay of CHOUGH came to its final design. When the requirements for the ADC were agreed, it was considered that it would have to go after the DM due to space considerations as depicted in Figure 7.1. Having this in mind, the ADC had to be designed aiming to minimum pupil-shift since the WFS would see an extra pupil-shift produced by the ADC and not present in the wavefront reaching the DM. What would happen is that the WFS would read this inexistent shift, thus the RTC would tell the DM to apply corrections for a tilt that is not there to the next incoming wavefront therefore adding an extra tilt to it. The pupil-shift will depend on the correction angle of the ADC. To illustrate this, a sinusoidal wave can be created using the DM. Figure 7.2 represents the sinusoidal wave on the two pupils and the shift after going though the ADC. Figure 7.3 illustrates a simplification of the example of the sinusoidal waves in a "perfect world" experiment. The picture on the left depicts the incoming sinusoidal wavefront (orange), the DM shape (blue) when applying corrections to this sinusoidal wave, and the resultant plane wavefront (green) after they cancel out. The plot on the right represents the same idea with the difference that the incoming wavefront is shifted off, thus the correction applied is not complete and the resultant wavefront is not flat.

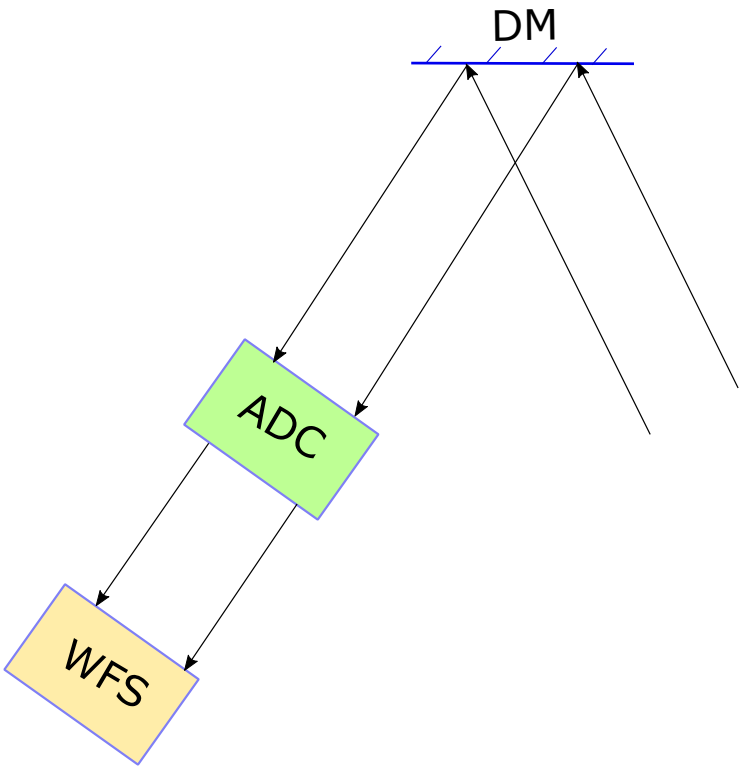

Figure 7.1: DM-ADC-WFS configuration.

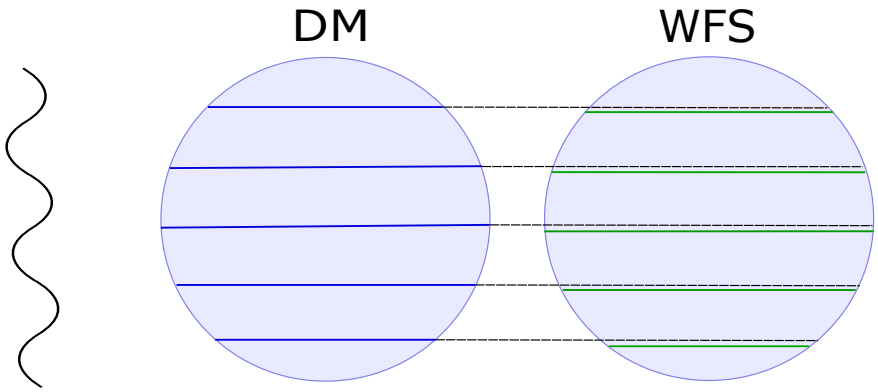

Figure 7.2: Illustration of the pupil shift of a sinusoidal wave on the WFS after going through the ADC.

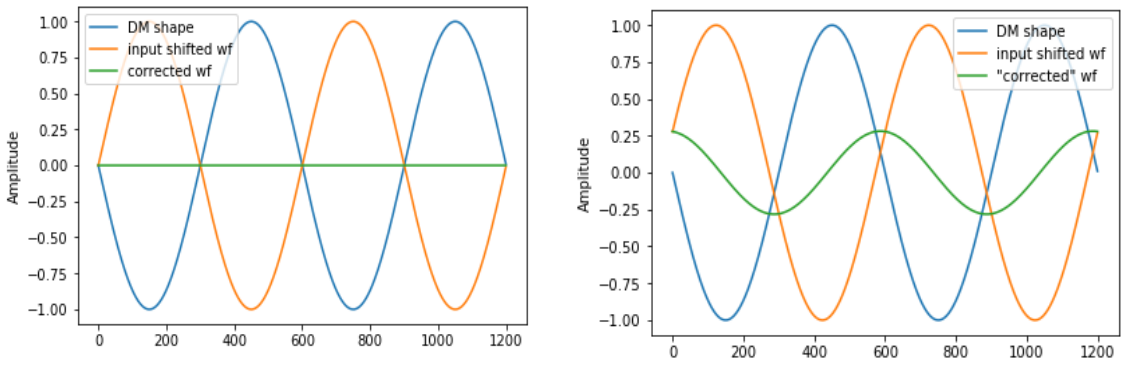

Figure 7.3: Sinusoidal wave when there is no shift present (left), and when the pupil is shifted (right). The incoming wavefront is in orange , the DM shape in blue, and the resultant plane wavefront after they cancel each other out is green.

Since this is the case for one iteration only, it is necessary to deduce a formula that can tell the effects of the pupil-shift on the resultant corrected wavefront after N iterations. In order to do this we start with the simple sum of the shape of the DM and shifted wavefront, same sinusoidal shape, different sign, and an extra phase ϕ in the input wavefront. Hence the first shifted wavefront after corrections applied takes the form

$$R\left(1\right) = \sin\left[2\pi x/\lambda\right] - \sin\left[2\pi x/\lambda + \phi\right] \,,$$

using the following identity

$$\sin A - \sin B = 2\cos\frac{1}{2}\left(A+B\right)\sin\frac{1}{2}\left(A-B\right); \sin\left(-A\right) = \sin A,$$

the resultant wave is

$$-2\sin\left[\frac{\phi}{2}\right]\cos\left(\left[\frac{2\pi x}{\lambda} + \frac{\phi}{2}\right]\right).$$

Applying a second shift

$$R\left(2\right) = -2\sin\left[\frac{\phi}{2}\right]\cos\left[\frac{2\pi x}{\lambda} + \frac{\phi}{2}\right] + 2\sin\left[\frac{\phi}{2}\right]\cos\left[\frac{2\pi x}{\lambda} + \frac{\phi}{2} + \phi\right]$$

and using the identity

$$\cos A - \cos B = 2 \sin \frac{1}{2} (A + B) \sin \frac{1}{2} (B - A) ; \cos (-A) = cos (A)$$

the resultant wave becomes

$$-4 \sin^2 \frac{\phi}{2} \sin \left[\frac{2\pi x}{\lambda} + \phi \right]$$

if we repeat the process for a third pupil-shift and correction

$$R (3) = -4 \sin^2 \frac{\phi}{2} \sin \left[\frac{2\pi x}{\lambda} + \phi \right] + 4 \sin^2 \frac{\phi}{2} \sin \left[\frac{2\pi x}{\lambda} + \phi + \phi \right]$$

the resultant wavefront is

$$8 \sin^3 \left[\frac{\phi}{2} \right] \cos \left[\frac{2\pi x}{\lambda} + \frac{3}{2} \phi \right]$$

if we repeat the process a few more times we obtained the following equations from n = 0 to n = 5

n = 0

$$R(0) : \sin \left[\frac{2\pi x}{\lambda} \right]$$

n = 1

$$R(1) : -2 \sin \left[\frac{\phi}{2} \right] \cos \left[\frac{2\pi x}{\lambda} + \frac{\phi}{2} \right]$$

n = 2

$$R(2) : -4 \sin^2 \left[\frac{\phi}{2} \right] \sin \left[\frac{2\pi x}{\lambda} + \phi \right]$$

n = 3

$$R(3) : 8 \sin^3 \left[\frac{\phi}{2} \right] \cos \left[\frac{2\pi x}{\lambda} + \frac{3\phi}{2} \right]$$

n = 4

$$R(4) : 16 \sin^4 \left[\frac{\phi}{2} \right] \sin \left[\frac{2\pi x}{\lambda} + 2\phi \right]$$

n = 5

$$R(5) : -32 \sin^5 \left[\frac{\phi}{2} \right] \cos \left[\frac{2\pi x}{\lambda} + \frac{5\phi}{2} \right] .$$

From these set of equations we can induce the following more general formula to calculate the resulting wave after n iterations:

$$\boxed{(-)^{\frac{n(n+1)}{2}} 2^n \sin^n\left[\frac{\phi}{2}\right] \sin\left[\frac{2\pi x}{\lambda} + \frac{n\phi}{2} + \frac{\pi}{4}\left[(-1)^{n+1}+1\right]\right].}$$

7.2 CHOUGH Optical Elements

Table 7.1: List of optical elements in CHOUGH.

Component	**Part Number**	**Manufacturer**	**Notes**	**R/T(%) at 550-650nm**
Periscope M1	PFE20-P01	Thorlabs	50.4mm elliptical, Ag	99.02
Periscope M2	PFE20-P01	Thorlabs	50.4mm elliptical, Ag	99.02
ADC Plate 1	CHOUGH-100-001	Gooch & Housego	2 prisms, custom, S-BAM4 & S-TIM3	99.00
ADC Plate 2	CHOUGH-100-001	Gooch & Housego	2 prisms, custom, S-BAM4 & S-TIM3	99.00
OAP M3	DUK-208-001	Aperture Optical Sciences	3", wedged OAP, f=1109.03mm, Ag	99.02
Flat mirror M4a	PF10-03-P01	Thorlabs	25.4mm circle, Ag	99.02
Flat mirror M4b	PF10-03-P01	Thorlabs	25.4mm circle, Ag	99.02
Spherical M5a	32-818	Edumund Optics	Protected Al	91.50
Spherical M5b	32-818	Edumund Optics	Protected Al	91.50
kilo-DM M6	BCDM32342-00-W01-M06-32	Boston Micromachines	BK7 Protective window wedge 6 deg. Al	86.25
Spherical M7	32-818	Edumund Optics	Protected Al	91.50
Dichroic D1	FF580-FDi01-25x36	SemRock	Dichroic, used at 13 degree. Ag	98.00
WFS LC1	49954	Edmund Optics	VIS-NIR Coated, Achromatic Lens	98.75
WFS LC2	65971	Edmund Optics	UV-VIS Coated, Near UV Achromatic Lens	98.50
WFS LC3	45125	Edmund Optics	Uncoated, Plano-Convex Lens	95.00
WFS LR1	45138	Edmund Optics	MgF2 Coated, Achromatic Doublet Lens	98.75
WFS LR2	32996	Edmund Optics	Uncoated, Double-Concave Lens	95.00
WFS LR3	45125	Edmund Optics	Uncoated, Plano-Convex Lens	95.00
LLA	18-00013	SUSS	1.2mm thick Fused Silica	99.50
Fold mirror M8	PF10-03-P01	Thorlabs	25.4mm circle, Ag	99.02
HNü 128 Camera Window	Not specified	Nüvü	3mm thick High Purity Fused Silica	94.00

Bibliography

The washington double star catalog. URL http://ad.usno.navy.mil/wds/.

E. Aller-Carpentier, M. Kasper, P. Martinez, E. Vernet, E. Fedrigo, C. Soenke, S. Tordo, N. Hubin, C. Verinaud, S. Esposito, E. Pinna, A. Puglisi, A. Tozzi, F. Quiros, A. G. Basden, S. J. Goodsell, G. D. Love, and R. M. Myers. High order test bench for extreme adaptive optics system optimization. *Proceedings of SPIE*, 7015(July 2008):70153Z–70153Z–12, 2008. ISSN 0277786X. doi: 10.1117/12.788710. URL http://link.aip.org/link/PSISDG/v7015/i1/p70153Z/s1{&}Agg=doi.

M. Bahrami and A. V. Goncharov. The achromatic design of an atmospheric dispersion corrector for extremely large telescopes. *Optics Express*, 19(18):17099, 2011. ISSN 1094-4087. doi: 10.1364/OE.19.017099.

A. Basden, D. Geng, R. Myers, and E. Younger. Durham adaptive optics real-time controller. *Applied optics*, 49(May):6354–6363, 2010. ISSN 0003-6935. doi: 10.1364/AO.49.006354.

J.-L. Beuzit. SPHERE: a planet finder instrument for the VLT. *Proc. SPIE*, 7014: 701418, 2008.

N. A. Bharmal, R. M. Myers, A. G. Basden, D. Hölck, and T. J. Morris. CHOUGH

, the Canary Hosted-Upgrade for High-order adaptive optics. In *SPIE 9148, Adaptive Optics Systems IV, 91485V (22 August 2014);*.

N. A. Bharmal, A. G. Basden, C. J. Bourgenot, M. Black, C. M. Dubbeldam, D. M. Henry, D. Hölck-Santibanez, T. J. Morris, D. J. Robertson, J. Schmoll, R. G. Talbot, E. J. Younger, and R. M. Myers. CHOUGH: implementation and performance of a high-order 4m AO demonstrator. 9909:990948, 2016. ISSN 1996756X. doi: 10.1117/12.2231721. URL `http://proceedings.spiedigitallibrary.org/proceeding.aspx?doi=10.1117/12.2231721`.

N. A. Bharmal, R. M. Myers, and H. Daniel. Chough , current status and future plans. 2018.

U. Bitenc, N. A. Bharmal, T. J. Morris, and R. M. Myers. Assessing the stability of an ALPAO deformable mirror for feed-forward operation. *Optics express*, 22(10):12438–51, 2014. ISSN 1094-4087. doi: 10.1364/OE.22.012438. URL `http://www.osapublishing.org/viewmedia.cfm?uri=oe-22-10-12438{&}seq=0{&}html=true`.

B. Bordwell, G. Duchene, E. Huby, S. Goebel, F. Marchis, G. Perrin, S. Lacour, T. Kotani, E. L. Gates, and E. Choquet. FIRST, a fibered aperture masking instrument: Results of the Lick observing campaign. In *American Astronomical Society Meeting Abstracts*, volume 225 of *American Astronomical Society Meeting Abstracts*, page 345.01, Jan. 2015.

A. H. Bouchez, R. G. Dekany, J. R. Angione, C. Baranec, M. C. Britton, K. Bui, R. S. Burruss, J. L. Cromer, S. R. Guiwits, J. R. Henning, J. Hickey, D. L. McKenna, A. M. Moore, J. E. Roberts, T. Q. Trinh, M. Troy, T. N. Truong, and V. Velur. The PALM-3000 high-order adaptive optics system for Palomar Observatory. *Proc. SPIE: Adaptive Optics Systems*, 7015:70150Z(7), 2008. ISSN 00404020. doi: 10.1016/j.tet.2005.02.009. URL `http://proceedings.spiedigitallibrary.org/proceeding.aspx?articleid=789871`.

R. Burruss, S. Hinkley, M. Wahl, J. Kuhn, E. Cady, R. Dekany, B. Mennesson, S. Metchev, B. Oppenheimer, R. Patel, and J. Roberts. First Exoplanet and Disk Results With the Palm-3000 Adaptive Optics System. (May):2–11, 2013. doi: 10.12839/AO4ELT3.13289.

R. S. Burruss, R. G. Dekany, J. E. Roberts, J. C. Shelton, J. K. Wallace, J. A. Tesch, D. L. Palmer, D. Hale, R. Bartos, K. M. Rykoski, C. M. Heffner, J. E. Eriksen, and F. Vescelus. Status of the PALM-3000 high order adaptive optics instrument. *Proc. SPIE, Adaptive Optics Systems IV*, 9148:914827, 2014. ISSN 1996756X. doi: 10.1117/12.2055538.

T. Currie, O. Guyon, M. Tamura, T. Kudo, N. Jovanovic, J. Lozi, J. Schlieder, T. Brandt, J. Kuhn, E. Serabyn, M. Janson, J. Carson, J. Kasdin, T. Groff, M. McElwain, G. Singh, T. Uyama, M. Kuzuhara, E. Akiyama, C. Grady, S. Hayashi, G. Knapp, J. Kwon, D. Oh, J. Wisniewski, M. Sitko, and Y. Yang. Subaru/SCExAO First-Light Direct Imaging of a Young Debris Disk around HD 36546. pages 1–6, 2017. ISSN 2041-8213. doi: 10.3847/2041-8213/836/1/L15. URL `http://arxiv.org/abs/1701.02314{%}0Ahttp://dx.doi.org/10.3847/2041-8213/836/1/L15`.

R. Dekany. High-contrast observation potential of the Palomar Adaptive Optics System (PALAO).

R. Dekany, J. Roberts, R. Burruss, A. Bouchez, T. Truong, C. Baranec, S. Guiwits, D. Hale, J. Angione, T. Trinh, J. Zolkower, J. C. Shelton, D. Palmer, J. Henning, E. Croner, M. Troy, D. McKenna, J. Tesch, S. Hildebrandt, and J. Milburn. PALM-3000: Exoplanet Adaptive Optics for the 5-meter Hale Telescope. 2013. doi: 10.1088/0004-637X/776/2/130. URL `http://arxiv.org/abs/1309.1216{%}0Ahttp://dx.doi.org/10.1088/0004-637X/776/2/130`.

N. Devaney, A. V. Goncharov, and J. C. Dainty. Chromatic effects of the atmosphere on astronomical adaptive optics. *Applied optics*, 47(8):1072–1081, 2008. ISSN 0003-6935. doi: 10.1364/AO.47.001072.

N. Dubost, N. Ali Bharmal, and R. Myers. Calibration of quasi-static aberrations in high-contrast astronomical adaptive optics with a pupil-modulated point-diffraction interferometer. 26:11068, 04 2018.

D. L. Fried. Optical resolution through a randomly inhomogeneous medium for very long and very short exposures. *JOSA*, 56(10):1372–1379, 1966.

D. L. Fried. Least-square fitting a wave-front distortion estimate to an array of phase-difference measurements. *Journal of the Optical Society of America*, 67 (3):370, 1977. ISSN 0030-3941. doi: 10.1364/JOSA.67.000370.

B. Garcia-Lorenzo and J. J. Fuensalida. Atmospheric optical-turbulence at Roque de los Muchachos Observatory : database and recalibration of the arXiv : 1106 . 2658v1 [astro-ph . IM] 14 Jun 2011. (June):1–8, 2011.

V. Garrel, O. Guyon, P. Baudoz, F. Martinache, P. Stewart, J. Lozi, and T. Groff. The Subaru coronagraphic extreme AO (SCExAO) system: fast visible imager. *Techniques and Instrumentation for Detection of Exoplanets V. Edited by Shaklan*, 8151:81510R–81510R–8, 2011. ISSN 0277786X. doi: 10.1117/12.894309. URL `http://adsabs.harvard.edu.ezproxy.obspm.fr/abs/2011SPIE.8151E..23G`.

E. Gendron, T. Morris, A. Basden, F. Vidal, D. Atkinson, U. Bitenc, T. Buey, F. Chemla, M. Cohen, C. Dickson, N. Dipper, P. Feautrier, J.-L. Gach, D. Gratadour, D. Henry, J.-M. Huet, C. Morel, S. Morris, R. Myers, J. Osborn, D. Perret, A. Reeves, G. Rousset, A. Sevin, E. Stadler, G. Talbot, S. Todd, and E. Younger. Final two-stage MOAO on-sky demonstration with CANARY. 9909:99090C, 2016. ISSN 1996756X. doi: 10.1117/12.2231432. URL `http://proceedings.spiedigitallibrary.org/proceeding.aspx?doi=10.1117/12.2231432`.

C. Giordano, J. Vernin, H. Vazquez Ramio, C. Munoz-Tunon, A. M. Varela, and H. Trinquet. Atmospheric and seeing forecast: WRF model validation with in

situ measurements at ORM. *Monthly Notices of the Royal Astronomical Society*, 430(4):3102–3111, 2013. ISSN 00358711. doi: 10.1093/mnras/stt117.

J. W. Hardy. *Adaptive Optics for Astronomical Telescopes*. Oxford University Press, 1998.

Y. Hayano, H. Takami, S. Oya, M. Hattori, Y. Saito, M. Watanabe, O. Guyon, Y. Minowa, S. E. Egner, M. Ito, V. Garrel, S. Colley, T. Golota, and M. Iye. Commissioning status of Subaru laser guide star adaptive optics system. *Proceedings of the SPIE*, 7736:77360N–77360N–8, 2010. ISSN 0277786X. doi: 10.1117/12.857567. URL `http://proceedings.spiedigitallibrary.org/proceeding.aspx?articleid=751083{%}5Cnhttp://adsabs.harvard.edu/abs/2010SPIE.7736E..21H`.

K. W. Hodapp, R. Suzuki, M. Tamura, L. Abe, H. Suto, R. Kandori, J. Morino, T. Nishimura, H. Takami, O. Guyon, S. Jacobson, V. Stahlberger, H. Yamada, R. Shelton, J. Hashimoto, A. Tavrov, J. Nishikawa, N. Ukita, H. Izumiura, M. Hayashi, T. Nakajima, T. Yamada, and T. Usuda. HiCIAO: the Subaru Telescope's new high-contrast coronographic imager for adaptive optics. *Proceedings of SPIE*, 7014(2008):701419–701419–12, 2008. ISSN 0277786X. doi: 10.1117/12.788088. URL `http://link.aip.org/link/PSISDG/v7014/i1/p701419/s1{&}Agg=doi`.

D. Hölck, N. A. Bharmal, C. M. Dubbeldam, and R. M. Myers. CHOUGH: spatially filtered Shack-Hartmann wave-front sensor for HOAO. 9909:990930, 2016. doi: 10.1117/12.2232364. URL `http://proceedings.spiedigitallibrary.org/proceeding.aspx?doi=10.1117/12.2232364`.

A. Kelz, F. Hammer, P. Jagourel, and t. M. Consortium. MOSAIC: a Multi-Object Spectrograph for the E-ELT. pages 1–4, 2015. URL `http://arxiv.org/abs/1512.00777`.

D. Kopon, J. Males, L. M. Close, and V. Gasho. <title>Enabling technologies for visible adaptive optics: the Magellan adaptive secondary VisAO camera</title>. *Society of Photo-Optical Instrumentation Engineers (SPIE) Conference Series*, 7439:74390Y–74390Y–12, 2009. ISSN 0277786X. doi: 10.1117/12.834688. URL `http://proceedings.spiedigitallibrary.org/proceeding.aspx?articleid=1340958`.

J. E. Larkin, J. K. Chilcote, T. Aliado, B. J. Bauman, G. Brims, J. M. Canfield, A. Cardwell, D. Dillon, R. Doyon, J. Dunn, M. P. Fitzgerald, J. R. Graham, S. Goodsell, M. Hartung, P. Hibon, P. Ingraham, C. a. Johnson, E. Kress, Q. M. Konopacky, B. a. Macintosh, K. G. Magnone, J. Maire, I. S. McLean, D. W. Palmer, M. D. Perrin, C. Quiroz, F. Rantakyrö, N. Sadakuni, L. Saddlemyer, A. Serio, S. Thibault, S. J. Thomas, P. Vallee, and J. L. Weiss. The integral field spectrograph for the Gemini planet imager. *Proceedings of SPIE*, 9147:91471K, 2014. ISSN 1996756X. doi: 10.1117/12.2056504. URL `http://proceedings.spiedigitallibrary.org/proceeding.aspx?doi=10.1117/12.2056504`.

J. Lozi, O. Guyon, N. Jovanovic, G. Singh, D. Doughty, P. Pathak, S. Goebel, and T. Kudo. SCExAO: the most complete instrument to characterize exoplanets and stellar environments. In *AAS/Division for Extreme Solar Systems Abstracts*, volume 3 of *AAS/Division for Extreme Solar Systems Abstracts*, page 104.03, Dec. 2015.

B. Macintosh, J. Graham, D. Palmer, R. Doyon, D. Gavel, J. Larkin, B. Oppenheimer, L. Saddlemyer, J. K. Wallace, B. Bauman, D. Erikson, L. Poyneer, A. Sivaramakrishnan, R. Soummer, and J. P. Veran. Adaptive optics for direct detection of extrasolar planets: the Gemini Planet Imager. *Comptes Rendus Physique*, 8(3-4):365–373, 2007. ISSN 16310705. doi: 10.1016/j.crhy.2007.04.007.

J. R. Males, L. M. Close, K. M. Morzinski, Z. Wahhaj, M. C. Liu, A. J. Skemer, D. Kopon, K. B. Follette, A. Puglisi, S. Esposito, A. Riccardi, E. Pinna, M. Xompero, R. Briguglio, B. A. Biller, E. L. Nielsen, P. M. Hinz, T. J. Rodigas, T. L.

Hayward, M. Chun, C. Ftaclas, D. W. Toomey, and Y. L. Wu. Magellan adaptive optics first-light observations of the exoplanet β pic b. I. direct imaging in the far-red optical with MagAO+VisAO and in the near-ir with nici. *Astrophysical Journal*, 786(1), 2014. ISSN 15384357. doi: 10.1088/0004-637X/786/1/32.

R. M. Myers, Z. Hubert, T. J. Morris, E. Gendron, N. a. Dipper, A. Kellerer, S. J. Goodsell, G. Rousset, E. Younger, M. Marteaud, A. G. Basden, F. Chemla, C. D. Guzman, T. Fusco, D. Geng, B. Le Roux, M. a. Harrison, A. J. Longmore, L. K. Young, F. Vidal, and A. H. Greenaway. CANARY: the on-sky NGS/LGS MOAO demonstrator for EAGLE. 7015:70150E–70150E–9, 2008. URL `http://proceedings.spiedigitallibrary.org/proceeding.aspx?articleid=789822`.

B. Norris, G. Schworer, P. Tuthill, N. Jovanovic, O. Guyon, P. Stewart, and F. Martinache. The VAMPIRES instrument: Imaging the innermost regions of protoplanetary discs with polarimetric interferometry. *Monthly Notices of the Royal Astronomical Society*, 447(3):2894–2906, 2015. ISSN 13652966. doi: 10.1093/mnras/stu2529.

P. Nussbaum. Birnbaum pp. 122-127.pdf. 6(1997):617–636, 2000.

C. Petit, T. Fusco, J. Charton, D. Mouillet, P. Rabou, T. Buey, G. Rousset, J.-F. F. Sauvage, P. Baudoz, P. Gigan, M. Kasper, E. Fedrigo, N. Hubin, P. Feautrier, J.-L. L. Beuzit, and P. Puget. The SPHERE XAO system: design and performance. *Adaptive Optics Systems. Edited by Hubin, Norbert; Max, Claire E.; Wizinowich, Peter L. Proceedings of the SPIE*, 7015:70151D–70151D–12 (2008), 2008. ISSN 0277786X. doi: 10.1117/12.790308.

L. A. Poyneer and B. Macintosh. Spatially filtered wave-front sensor for high-order adaptive optics. 21(5):810–819, 2004.

L. A. Poyneer, D. W. Palmer, B. Macintosh, D. Savransky, N. Sadakuni, S. Thomas, J.-P. Véran, K. B. Follette, A. Z. Greenbaum, S. Mark Ammons,

V. P. Bailey, B. Bauman, A. Cardwell, D. Dillon, D. Gavel, M. Hartung, P. Hibon, M. D. Perrin, F. T. Rantakyrö, A. Sivaramakrishnan, and J. J. Wang. Status and Performance of the Gemini Planet Imager's adaptive optics system. *Applied Optics*, 55(2):323, 2016. ISSN 0003-6935. doi: 10.1364/AO.55.000323. URL `http://proceedings.spiedigitallibrary.org/proceeding.aspx?articleid=2540731{%}5Cnhttps://www.osapublishing.org/abstract.cfm?URI=ao-55-2-323`.

B. W. F. Robert K. Tyson. *Field Guide to Adaptive Optics*. SPIE PRESS, 2004.

F. Roddier, J. M. Gilli, and G. Lund. On the origin of speckle boiling and its effects in stellar speckle interferometry. *Journal of Optics*, 13(5):263, 1982. URL `http://stacks.iop.org/0150-536X/13/i=5/a=002`.

Rousset, G., J. C. Fontanella, P. Kern, P. Gigan, F. Rigaut, P. Lena, C. Boyer, P. Jagourel, J. Gaffard, and F. Merkle. First difraction-limited astronomical images with adaptive optics. *A&A*, 230:L29–L32, 1990.

E. Sissa, J. Olofsson, A. Vigan, J. C. Augereau, V. D'Orazi, S. Desidera, R. Gratton, M. L. E. Rigliaco, A. Boccaletti, Q. Kral, C. Lazzoni, D. Mesa, S. Messina, E. Sezestre, P. Thébault, A. Zurlo, T. Bhowmik, M. Bonnefoy, G. Chauvin, M. Feldt, J. Hagelberg, A. M. Lagrange, M. Janson, A. L. Maire, F. Ménard, J. Schlieder, T. Schmidt, J. Szulágyi, E. Stadler, D. M. A. Deboulbé, P. Feautrier, J. Ramos, and R. Rigal. New disk discovered with VLT/SPHERE around the M star GSC 07396-00759. 7, 2018. ISSN 0004-6361. doi: 10.1051/0004-6361/201832740. URL `http://arxiv.org/abs/1804.02882`.

C. Wynne and S. Worswich. Atmospheric dispersion correctors at the Cassegrain focus. *Mon. Not.R.astr.Soc*, 220:657–670, 1986.

Colophon

This thesis was typeset with LaTeX 2$_\varepsilon$. It was created using the *memoir* package, maintained by Lars Madsen, with the *madsen* chapter style. The font used is Latin Modern, derived from fonts designed by Donald E. Kunith.